Universidade do Minho
Escola de Ciências

Tiago Miguel Pereira Rebelo

Ferroelectric thin film nanostructures by laser ablation

July 2021

Ferroelectric thin film nanostructures by laser ablation

Tiago Miguel Pereira Rebelo

UMinho | 2021

Universidade do Minho
Escola de Ciências

Tiago Miguel Pereira Rebelo

Ferroelectric thin film nanostructures by laser ablation

Dissertação de Mestrado
Mestrado em Física

Trabalho efetuado sob a orientação do

Professor Doutor Bernardo Gonçalves Almeida
Doutor Leonard Deepak Francis

Julho de 2021

DIREITOS DE AUTOR E CONDIÇÕES DE UTILIZAÇÃO DO TRABALHO POR TERCEIROS

Este é um trabalho académico que pode ser utilizado por terceiros desde que respeitadas as regras e boas práticas internacionalmente aceites, no que concerne aos direitos de autor e direitos conexos.

Assim, opresente trabalho pode ser utilizado nos termos previstos na licença abaixo indicada.

Caso o utilizador necessite de permissão para poder fazer um uso do trabalhoem condições não previstas no licenciamento indicado, deverá contactar o autor, através do RepositóriUM da Universidade do Minho.

Licença concedida aos utilizadores deste trabalho

Atribuição
CC BY

https://creativecommons.org/licenses/by/4.0/

Acknowledgements

There are several people to whom I am very grateful, for this work and life phase possibly wouldn't have come to fruition without them.

To my mother, for all her love, support and encouragement when I felt down and questioned myself, despite her own health struggles. She is a great inspiration for me and gives me strength to keep moving.

To my father, for providing the opportunity for me to keep pursuing my studies despite the delays along the way.

To Igor, for the friendship and support in hard times. And to Diogo, for all the help during my course and fun moments.

To João and Bruna, for all the help with the deposition of the samples.

To Kike, for the huge support, availability and help anytime I approached with a question. You did much more than was your obligation. Thank you very much, Kike.

To Oliver, for all the help whenever I had difficulties.

To Rong and Saha, for taking the time to teach me in the laboratory.

To Dr. Leonard Francis, for accepting to co-supervise me and allowing me the opportunity to work in a top-level research facility and experiencing the research environment at such an institution. Thank you.

Finally, one of the persons to whom I feel most grateful is my supervisor, Dr. Bernardo Almeida. For accepting to supervise me, and for all the support, availability and enormous patience he always had. And for all the encouragement whenever I questioned my abilities or expressed doubt. You went beyond the responsibility of a supervisor and I am extremely grateful for that. Thank you very much, professor.

STATEMENT OF INTEGRITY

I hereby declare having conducted this academic work with integrity. I confirm that I have not used plagiarism or any form of undue use of information or falsification of results along the process leading to its elaboration.

I further declare that I have fully acknowledged the Code of Ethical Conduct of the University of Minho.

Resumo

Materiais compósitos multiferróicos são de grande interesse para aplicações tecnológicas devido ao efeito de acoplamento magnetoeléctrico, através do qual se pode usar um campo eléctrico (magnético) para controlar a magnetização (polarização). Este efeito pode ser aumentado consideravelmente sob a forma de filmes finos através de engenharia de tensões, ou seja, a indução propositada de tensões na estrutura cristalina ao combinar materiais com parâmetros de rede distintos. Existem vários métodos para produzir as estruturas compósitas, sendo a ablação laser pulsada num gás de fundo notável pela sua simplicidade e controlo preciso dos parâmetros de deposição, nomeadamente da pressão do gás e da distância alvo-substrato. Contudo, a optimização dos parâmetros de deposição de forma a obter filmes com a microestrutura pretendida ainda é feita à base de tentativa e erro, justificando a modelização da dinâmica da pluma de ablação no gás de fundo a fim de tentar prever a estrutura resultante no filme.

Neste estudo, sistemas compósitos multiferróicos foram produzidos por ablação laser pulsada. Os sistemas estudados foram filmes finos de niobato de lítio ($LiNbO_3$, ferroeléctrico) depositados em substratos de Si e de Si\Pt, e filmes finos bi-camada de $LiNbO_3/CoFe_2O_4$ (ferrite de cobalto, ferromagnético) depositados em substratos de Si\Pt. O $LiNbO_3$ possui propriedades piezoeléctricas e electro-ópticas elevadas enquanto que o $CoFe_2O_4$ tem uma magnetostrição, magnetização de saturação, coercividade e anisotropia magnetocristalina elevadas. Os filmes foram depositados a 650 °C e à temperatura ambiente, neste último caso tendo sido submetidos a um processo de recozimento pós-deposição. Foram usadas diferentes combinações de pressão e distância alvo-substrato. Estudaram-se os filmes usando técnias de microscopia electrónica, nomeadamente microscopia electrónica de varrimento e feixe de iões focado.

A dinâmica da pluma de ablação no gás de fundo foi modelizada segundo um modelo de onda de choque, resultando uma equação para a propagação da frente de onda e permitindo a determinação de uma relação pressão-distância. Ao aplicar esta relação aos filmes, foi construído um diagrama de fases das zonas do diagrama de Thornton, para ambas as temperaturas de deposição, permitindo a previsão de zona estrutural resultante para uma dada pressão e distância.

Observou-se que filmes depositados à temperatura ambiente tinham uma estrutura da zona 1, modificada para a zona 2-3 pelo processo de recozimento. Filmes depositados a 650 °C tinham uma estrutura da zona 2-3 excepto quando o tempo de deposição era muito elevado. Neste caso observou-se uma estrutura da zona 1-T, resultado da espessura acrescida do filme induzir relaxamento da estrutura e defeitos. Os diagramas de fase obtidos revelam que, para que os filmes de $LiNbO_3$ atinjam uma estrutura da zona 2-3 à temperatura ambiente, a distância alvo-substrato teria que ser baixa o suficiente tal que repulverização do filme depositado se torna provável. Também se observou que, de uma forma geral, a espessura do filme e os tamanhos de grão aumentam com o tempo de deposição. Contudo, o aparecimento de uma estrutura da zona 1 para valores elevados do tempo de deposição indica a existência de um valor óptimo, atingindo um equilíbrio entre cristalinidade do filme e microestrutura adequada, mas sem aumento da espessura ao ponto de impedir difusão de superfície ou induzir relaxamento da estrutura nos filmes.

Palavras chave: ablação laser, diagrama de Thornton, filme fino, multiferróico, SEM

Abstract

Multiferroic composite materials are of great interest for technological applications due to the magnetoelectric coupling effect, by which an electric (magnetic) field may be used to control the magnetization (polarization). In the form of thin films this effect can be considerably increased by strain engineering, or the purposeful creation of strains in the crystalline structure by the combination of materials with lattice mismatch. Different deposition methods are available to produce the composite structures, with pulsed laser ablation in a background gas being noteworthy for its simplicity and precise control of the deposition parameters, namely the gas pressure and the target-substrate distance. However, the optimization of the deposition parameters to obtain films with the desired microstructure is still performed on a trial and error basis, justifying the modelling of the ablation plume dynamics with the background gas in order to try and predict the resulting film structure.

In this study, multiferroic composite systems were produced by pulsed laser ablation. The systems studied consisted of lithium niobate ($LiNbO_3$, ferroelectric) thin films deposited on Si and Si\Pt substrates, and bi-layer $LiNbO_3/CoFe_2O_4$ (cobalt ferrite, ferromagnetic) thin films deposited on Si\Pt substrates. $LiNbO_3$ possesses high piezoelectric and electro-optic properties while $CoFe_2O_4$ has high magnetostriction, saturation magnetization, coercivity and magnetocrystalline anisotropy. The films were deposited at 650 °C and at room temperature, with the latter submitted to an annealing procedure post-deposition. Different pressure and target-substrate distance combinations were used. The resulting films were studied using electron microscopy techniques, namely scanning electron microscopy and focused ion beam.

The ablation plume dynamics in the background gas was modelled according to a blast wave model, providing an equation for the propagation of the shock front and allowing the determination of a pressure-distance relationship. Applying this relationship to the films, a phase diagram of the zones of Thornton's diagram was built for both deposition temperatures, allowing the prediction of the resulting zone structure for a given pressure and distance.

It was observed that films deposited at room temperature displayed a zone 1 structure, with the annealing procedure modifying it to zone 2-3. Films deposited at 650 °C displayed a zone 2-3 structure, except when the deposition time was very high. In this case a zone 1-T structure was observed, a result of the increased film thickness inducing the presence of structure relaxation and defects. The phase diagrams obtained reveal that for the $LiNbO_3$ films to achieve a zone 2-3 structure at room temperature, the target-substrate distance would have to be low enough that resputtering of the deposited film becomes likely.

It was also observed that the film thickness and grain size generally increased with deposition time. However, the appearance of a zone 1 structure for high values of deposition time indicates the existence of an optimal value, striking a balance between film crystallinity and adequate microstructure, but without increasing the thickness to the extent of inhibiting surface diffusion or inducing structure relaxation in the films.

Keywords: laser ablation, multiferroic, SEM, thin film, Thornton diagram

Contents

1 Introduction and dissertation structure 18
1.1 Introduction . . . 18
1.2 Structure of the dissertation . . . 19

2 Theoretical introduction 20
2.1 Electric and magnetic materials . . . 20
2.1.1 Piezoelectricity . . . 20
2.1.2 Ferroelectricity . . . 20
2.1.3 Ferromagnetism . . . 21
2.1.4 Multiferroism and magnetoelectricity . . . 21
2.2 Materials used . . . 23
2.2.1 Lithium niobate . . . 23
2.2.2 Cobalt ferrite . . . 23
2.2.3 Silicon-Platinum . . . 24
2.2.4 Systems studied . . . 25
2.3 Pulsed laser ablation . . . 25
2.3.1 Ablation of material from the target - laser-target interactions . . . 26
2.3.2 Plume expansion . . . 27
2.3.3 Pressure-distance scaling law . . . 29
2.3.4 Film deposition and microstructure . . . 30
2.3.5 Structure zone models . . . 32

3 Experimental techniques 35
3.1 Film growth - Pulsed Laser Ablation . . . 35
3.1.1 Parameters that influence the deposition . . . 36
3.1.2 Advantages and disadvantages of the technique . . . 37
3.1.3 Equipment used . . . 38
3.2 Characterization techniques . . . 39
3.2.1 Electron microscopy . . . 40
3.2.2 Scanning electron microscopy . . . 40
3.2.3 Energy dispersive X-ray spectroscopy . . . 48
3.2.4 Focused ion beam . . . 48
3.2.5 Equipment used . . . 51

4 Results and Discussion 53
4.1 Experimental results . . . 53
4.1.1 LNO film on Si substrate . . . 54

4.1.2 LNO film on SiPt substrate 74
4.1.3 CFO-LNO film on SiPt substrate 77
4.1.4 Thornton's diagram zones of the studied samples 109
4.2 Application of the pressure-distance scaling law 110
4.2.1 Single-layer LNO films 110
4.2.2 CFO films 112
4.3 Effect of the deposition time 113

5 Conclusions and suggestions of future works 116

List of Figures

2.1 Hysteresis cycle typically seen on a ferroelectric, with different characteristics of interest of the material. Image adapted from Ref. [1]. 21
2.2 Schematic of the necessary overlap of electric and magnetic properties for multiferroism and magnetoelectricity. Image from Ref. [2]. 22
2.3 Different possible geometries for the multiferroic composites: a) particles inside a matrix; b) horizontal multilayer; c) vertical columns inside a martix. Image from Ref. [3]. 22
2.4 Atomic structure of LNO, showing the paraelectric (a) and ferroelectric (b),(c) phases. Image from Ref. [4]. 23
2.5 Crystal structure of CFO showing the octahedral and tetrahedral sites. Image from Ref. [5]. 24
2.6 The layers of a SiPt substrate. The brightest layer (yellow measurements) is the Pt layer. Below the SiO_2 is the Si. 24
2.7 The composite systems investigated in the present study: LNO thin film on Si substrate, LNO thin film on SiPt substrate, CFO thin film on SiPt substrate and CFO/LNO bilayer film on SiPt substrate. The grey layer on the SiPt substrates represents the Pt. 25
2.8 Schematic representation of the different stages of the PLA process. (a) Absorption of laser radiation (long black arrows) by the target and beginning of melting and vaporization. The shaded region represents melted material and the short arrows the movement of the melt front. (b) Vaporization increases originating a plume and the melt front progresses further into the solid part of the target. (c) The plume absorbs some of the laser radiation, originating a plasma and optical emissions (small arrows exiting the plume). (d) After the pulse stops the molten part of the target resolidifies and the melt front recedes. Figure taken from Ref. [6]. 25
2.9 Schematic representation of the plume shape as dictated by a cosine power law for different values of the exponent. Image adapted from Ref. [7]. 28
2.10 Photographs of the visible plasma emission from an YBCO (high-temperature superconductor ceramic) expanding plume during a PLA process, in vacuum (upper row of images) and in a background atmosphere of oxygen (lower row of images). Each photograph was taken at the indicated time after the laser pulse struck the target. The lower-right schematic shows the geometry of the experiment as well as the distance from the target that the plume reaches. Image from Ref. [8]. 28
2.11 Nucleus of a film on a substrate and interfacial energies involved. Image adapted from Ref. [7]. 30
2.12 The three major growth modes: (a) island, (b) layer-by-layer and (c) layer-plus-island. Image from Ref. [7]. 30
2.13 The structure zone model of Movchan and Demchishin (MD). Image from Ref. [9]. . . . 32
2.14 The structure zone model proposed by Thornton. Image from Ref. [10]. 33

2.15 Microstructure of zone 1. Image from Ref. [10]. 34
2.16 Another image of a zone 1 microstructure. Image from Ref. [10]. 34
2.17 Microstructure of zone T. Image from Ref. [10]. 34
2.18 Another image of a zone T microstructure. Image from Ref. [10]. 34
2.19 Microstructure of zone 2. Image from Ref. [10]. 34
2.20 Microstructure of zone 3. Image from Ref. [10]. 34
3.1 Schematic setup of a PLD apparatus. The inset picture shows a plume generated during the process. Image from Ref. [7]. 35
3.2 The PLD deposition chamber of the Laboratório de Filmes Finos do Centro de Física da Universidade do Minho. 38
3.3 Optical system of the Laboratório de Filmes Finos do Centro de Física da Universidade do Minho. 39
3.4 Oven used for sample annealing. 39
3.5 Cross-sectional view of the general structure and constituents of a SEM. The region above the backscattered electron detector is the microscope column; the region below it is the specimen chamber. The electron beam is represented in red. 41
3.6 Schematic representation of the interaction volume of the electron beam with the sample, with the different signals generated and corresponding depth of origin. The values shown were taken from Ref. [11](Auger electrons), Ref. [12](SE), Ref. [13](BSE) and Ref. [14](X-rays). 42
3.7 Cross-sectional view of the electron beam after exiting the final lens aperture, with the major beam parameters that affect the image obtained. a_v is the accelerating voltage applied to the electron beam, I_{inc} is the incident current, α is the convergence angle and S is the spot size. WD is the working distance. 43
3.8 Cross-sectional view of the general structure of a Dual Beam FIB-SEM. In the top-left, the general constituents of the ion column are indicated. The electron beam is represented in red and the ion beam in green. The sample chamber also features SE, BSE and EDS detectors but these are not represented. 49
3.9 Preparation step of a lamella, showing the first cross-section milled. 51
3.10 Preparation step of a lamella showing the two cross-sections milled - one in front of the protected surface region and the other behind it. 51
3.11 The FEI Quanta 650 FEG of the INL - International Iberian Nanotechnology Laboratory. . 52
3.12 The FEI Helios G2 NanoLab 450S of the INL - International Iberian Nanotechnology Laboratory. 52
4.1 SEM-EDS spectrum of the sample. 54
4.2 Low magnification SEM image showing the surface of the sample. 54
4.3 Higher magnification SEM image of Figure 4.2. 55
4.4 Higher magnification image but on another region. 55
4.5 SEM image showing a highly dense region amidst the less dense surroundings. 55

4.6 High magnification SEM image showing a low-density region. . . . 56
4.7 Higher magnification SEM image of Figure 4.6 revealing individual grains. . . . 56
4.8 High magnification SEM image of a dense region. . . . 57
4.9 Grain size distribution of the sample with mean average size and respective standard deviation indicated. . . . 57
4.10 High magnification SEM image of the film's cross-section, showing the formed voids and some representative dimensions. . . . 57
4.11 SEM-EDS spectrum of the sample's surface. . . . 58
4.12 High magnification SEM image of the surface of the sample. The white arrows indicate regions of smaller grain size. . . . 58
4.13 High magnification SEM image of another region, displaying the close-packing of the grains. 59
4.14 High magnification SEM image of a region with both larger and smaller grains. . . . 59
4.15 Size distribution of the larger grains. . . . 60
4.16 Size distribution of the smaller grains. . . . 60
4.17 High magnification FIB-SEM image of the cross-section with the film's thickness indicated. 60
4.18 SEM-EDS spectrum of the sample's surface. . . . 61
4.19 High magnification SEM image showing the surface of the sample. . . . 61
4.20 High magnification SEM image showing a region where the film was damaged, exposing the Si substrate (dark region on the left). . . . 62
4.21 High magnification SEM image of the surface. . . . 62
4.22 Size distribution of the grains. . . . 62
4.23 SEM-EDS spectrum of the sample's surface. . . . 63
4.24 Surface of the sample. . . . 64
4.25 SEM image of the surface taken at higher magnification and smaller spot size. . . . 64
4.26 Grain size distribution of the sample. . . . 64
4.27 SEM image taken at 10 kV showing the surface of the sample. . . . 64
4.28 High magnification SEM image of the surface taken in low vacuum mode and low kV. . . . 65
4.29 Higher magnification SEM image of the surface in low vacuum mode. . . . 65
4.30 SEM-EDS spectrum of the surface. . . . 66
4.31 SEM image showing the surface of the $LiNbO_3$ film after annealing, imaged in low vacuum mode. . . . 67
4.32 High magnification SEM image of the surface. . . . 67
4.33 Size distribution of the voids. . . . 67
4.34 Size distribution of the small grains. . . . 67
4.35 SEM image image of another region taken in high vacuum mode. . . . 68
4.36 Size distribution of the large grains. . . . 68
4.37 SEM image of the surface taken with a higher accelerating voltage. . . . 68
4.38 SEM-EDS spectrum of the non-annealed sample. . . . 69
4.39 SEM-EDS spectrum of the annealed sample. . . . 69

4.40 SEM image showing the surface of the non-annealed sample. . . . 70
4.41 Droplet's size distribution. . . . 70
4.42 Higher magnification SEM image of the region imaged in Figure 4.40. . . . 70
4.43 SEM image showing another region of the non-annealed sample. . . . 70
4.44 SEM image showing the surface of the annealed sample. . . . 71
4.45 Size distribution of the voids in the annealed sample. . . . 71
4.46 Higher magnification SEM image of the region shown in Figure 4.44. . . . 71
4.47 Size distribution of the grains. . . . 71
4.48 SEM-EDS spectrum of the non-annealed sample. . . . 72
4.49 SEM-EDS spectrum of the annealed sample. . . . 72
4.50 SEM image showing the surface of the $LiNbO_3$ film in the non-annealed sample. . . . 73
4.51 Higher magnification SEM image of the surface (non-annealed sample). . . . 73
4.52 SEM image of the surface (non-annealed sample) taken at higher kV. . . . 73
4.53 Grain size distribution of the non-annealed sample. . . . 73
4.54 SEM image showing the surface of the annealed sample. . . . 74
4.55 SEM image of another region of the annealed sample. . . . 74
4.56 SEM-EDS spectrum of the sample's surface. . . . 75
4.57 SEM-EDS spectrum of another region showing the presence of oxygen. . . . 75
4.58 SEM image showing the surface of the $LiNbO_3$ film. . . . 75
4.59 Higher magnification SEM image of the surface. . . . 76
4.60 Grain size distribution of the sample. . . . 76
4.61 SEM image of the surface taken at high-kV. . . . 76
4.62 Small grain size distribution. . . . 76
4.63 SEM image showing the gold coated films for dielectric measurements. . . . 77
4.64 X-ray diffraction patterns of the indicated samples. The red and blue vertical lines are the diffraction peaks of the LNO and CFO, respectively. Image adapted from Ref. [15]. . . . 77
4.65 SEM-EDS spectrum of the surface. . . . 78
4.66 SEM image showing the surface of the sample. . . . 79
4.67 High magnification SEM image of the surface. . . . 79
4.68 Size distribution of the white dots. . . . 79
4.69 Higher magnification SEM image of the surface revealing that it is made up of grains. . . . 79
4.70 High magnification SEM image of the grains. . . . 80
4.71 Grain size distribution. . . . 80
4.72 FIB-SEM image showing the cross-section of the sample with the thicknesses of the different layers. . . . 80
4.73 EDS spectrum of the cross-section acquired from the FIB-SEM. . . . 81
4.74 SEM image showing the surface of the sample. . . . 82
4.75 High magnification SEM image of the film's surface, displaying the grain boundaries. . . . 82

4.76 High magnification SEM image of a boundary between the aforementioned dark and bright regions (upper and lower halves of the image, respectively). 82
4.77 High magnification SEM image of the bright region. 82
4.78 Higher magnification SEM image of the region showed in Figure 4.76. 82
4.79 High magnification SEM image of the film's surface. 83
4.80 $LiNbO_3$ grain size distribution. 83
4.81 FIB-SEM cross-section image of the sample with the different layers identified. 83
4.82 $CoFe_2O_4$ grain size distribution. 83
4.83 High magnification FIB-SEM image of the cross-section with the different layer's thicknesses. 84
4.84 SEM-EDS spectrum of the surface. 84
4.85 SEM image showing the surface of the sample ($LiNbO_3$ layer). 85
4.86 High magnification SEM image of the $LiNbO_3$ layer. 85
4.87 $LiNbO_3$ grain size distribution. 85
4.88 Cross-section image of the sample imaged with the FIB-SEM. 86
4.89 High magnification image of the cross-section with the thicknesses of the different layers indicated, imaged by FIB-SEM. 86
4.90 SEM-EDS spectrum of the surface. 86
4.91 SEM image showing the surface of the sample ($LiNbO_3$ layer). 87
4.92 High magnification SEM image of the surface. 87
4.93 Size distribution of the LNO grains. 87
4.94 High magnification SEM image of the surface showing the LNO faceted grains. 88
4.95 Size distribution of the smaller LNO grains. 88
4.96 Cross-section image of the sample showing its different layers imaged by the FIB-SEM. . 88
4.97 The thickness of the different layers (red = SiO_2 layer, blue = TiO_x layer, yellow = Pt layer, orange = film). 88
4.98 SEM-EDS spectrum of the sample's cross-section. 89
4.99 Surface of the sample showing the $LiNbO_3$ layer imaged by the SEM. 89
4.100 Size distribution of the large particulates. 89
4.101 High magnification SEM image of the surface. 90
4.102 Higher magnification SEM image of the surface. 90
4.103 Size distribution of the agglomerations. 90
4.104 High magnification SEM image of the surface. 91
4.105 Size distribution of the small grains. 91
4.106 The non-uniformity of the film thickness due to the plume's shape. The region imaged in the previous sample corresponds to the red line while that imaged in the present sample corresponds to the orange one. 91
4.107 FIB-SEM image of the cross-section of the sample with the thicknesses of its layers. . . . 92
4.108 Excerpt from Figure 5 of Ref. [16]. Original simulations from Ref. [17]. 92
4.109 SEM-EDS spectrum of the sample's cross-section. 92

4.110 SEM image of the surface of the sample. 93
4.111 High magnification SEM image of the surface. 93
4.112 Size distribution of the agglomerations. 93
4.113 The individual grains that constitute the film. 94
4.114 Size distribution of the LNO grains. 94
4.115 FIB-SEM image of the cross-section of the sample revealing its different layers and their thicknesses. 94
4.116 SEM-EDS spectrum of the sample's surface. 95
4.117 SEM image of the surface of the sample. 95
4.118 High magnification SEM image of the surface. 95
4.119 High magnification SEM image of a bright region. 96
4.120 SEM-EDS spectrum of a bright region. 96
4.121 High magnification SEM image of the surface. 96
4.122 Higher magnification SEM image of the surface. 97
4.123 Size distribution of the LNO large grains. 97
4.124 High magnification SEM image of the grains. 97
4.125 Size distribution of the LNO small grains. 97
4.126 FIB-SEM image of the cross-section of the sample showing its different layers. Each film is indicated. 98
4.127 FIB-SEM higher magnification image of the cross-section with the layers' thicknesses. The film layer (CFO + LNO) measurements are presented in yellow. 98
4.128 SEM-EDS spectrum of the sample's surface. 98
4.129 SEM image of the surface of the sample. 99
4.130 High magnification SEM image of the surface. 99
4.131 Higher magnification SEM image of the surface. 99
4.132 SEM image showing the individual grains that constitute the surface (LNO layer). 100
4.133 Size distribution of the LNO grains. 100
4.134 FIB-SEM image showing the cross-section of the sample. 100
4.135 SEM-EDS spectrum of the sample's surface. 101
4.136 SEM image of the surface of the sample (LNO layer). 101
4.137 High magnification SEM image of the sample's surface. 102
4.138 Size distribution of the LNO grains. 102
4.139 FIB-SEM image of the cross-section of the sample. The measured region is the film. . . . 102
4.140 FIB-SEM image of another region of the film's layer. 102
4.141 Higher magnification FIB-SEM image of the sample's cross-section with the film layer measurements. 103
4.142 SEM-EDS spectrum of the sample's cross-section. 103
4.143 SEM image showing the surface of the sample, observed at a tilt of 52°. The protective Pt layer deposited and its height are shown as well. 104

4.144 Size distribution of the LNO grains. 104
4.145 FIB-SEM image of the cross-section of the sample. 104
4.146 A lamella of the sample imaged in STEM mode, in bright-field (BF) mode. The thicknesses of the film (red), the substrate's Pt layer (green), the Ti layer (blue) and the SiO_2 layer (orange) are presented. 105
4.147 Close-up of the lamella in BF mode. 105
4.148 Another region of the lamella imaged in BF mode. 106
4.149 SEM-EDS spectrum of the sample's surface. 106
4.150 SEM image of the surface of the sample. 107
4.151 Size distribution of the large particulates. 107
4.152 High magnification SEM image of the surface. 107
4.153 High magnification SEM image of the surface. 108
4.154 Grain size distribution of the sample. 108
4.155 Very low accelerating voltage SEM image of the surface. 108
4.156 P-D scaling law obtained for single-layer LNO films at the temperatures indicated. The Thornton's diagram zones observed for samples deposited at both temperatures are indicated as well. 111
4.157 P-D scaling law obtained for the CFO layer at the temperature indicated. The Thornton's diagram zones observed for this layer in other samples (both single film and bi-layer film) are also represented. 112
4.158 Variation of the total film thickness (CFO layer + LNO layer) with the total deposition time (t_{dep}(CFO) + t_{dep}(LNO)). 113
4.159 Variation of the LNO large grain size with the deposition time. An increasing tendency is visible. 114
4.160 Grainy surface of sample SiPtCFOLNO 9. The total deposition time was 135 minutes. . . 115
4.161 Cross-section of sample SiPtCFOLNO 9. 115
4.162 Grainy surface of sample SiPtCFOLNO 10. The total deposition time was 105 minutes. . 115
4.163 Cross-section of sample SiPtCFOLNO 10. 115

List of Tables

1 Deposition conditions of the LNO and CFO films studied. . . . 53
2 Deposition conditions of the CFO-LNO films studied. . . . 53
3 Deposition conditions of sample SiLNO 6A. . . . 54
4 Results of SEM-EDS analysis. . . . 54
5 Deposition conditions of sample SiLNO 5B. . . . 58
6 Results of SEM-EDS analysis. . . . 58
7 Deposition conditions of sample SiLNO 5B. . . . 61
8 Results of SEM-EDS analysis. . . . 61
9 Deposition conditions of sample SiLNO 10A. . . . 63
10 Results of SEM-EDS analysis. . . . 63
11 Results of SEM-EDS analysis. . . . 66
12 Deposition conditions of samples SiLNO 11A/B. . . . 69
13 Results of SEM-EDS analysis for the non-annealed sample. . . . 69
14 Results of SEM-EDS analysis for the annealed sample. . . . 69
15 Deposition conditions of samples SiLNO 12A/B. . . . 72
16 Results of SEM-EDS analysis for the non-annealed sample. . . . 72
17 Results of SEM-EDS analysis for the annealed sample. . . . 72
18 Deposition conditions of sample SiPtLNO4B. . . . 74
19 Lattice parameters obtained for the LNO and CFO. Calculated in Ref. [15]. . . . 78
20 Deposition conditions of the SiPtCFO 2 sample. . . . 78
21 Results of SEM-EDS analysis. . . . 78
22 Deposition conditions of the SiPtCFOLNO 2 sample. . . . 81
23 Results of SEM-EDS analysis. . . . 81
24 Deposition conditions of the SiPtCFOLNO 6 sample. . . . 84
25 Results of SEM-EDS analysis. . . . 84
26 Deposition conditions of sample SiPtCFOLNO 8. . . . 86
27 Results of SEM-EDS analysis. . . . 86
28 Results of SEM-EDS analysis. . . . 89
29 Deposition conditions of sample SiPtCFOLNO 10. . . . 92
30 Results of SEM-EDS analysis. . . . 92
31 Deposition conditions of sample SiPtCFOLNO 15. . . . 95
32 Results of SEM-EDS analysis. . . . 95
33 Deposition conditions of sample SiPtCFOLNO 16. . . . 98
34 Results of SEM-EDS analysis. . . . 98
35 Deposition conditions of sample SiPtCFOLNO 17. . . . 101
36 Results of SEM-EDS analysis. . . . 101
37 Deposition conditions of the sample SiPtCFOLNO 19. . . . 103

38 Results of SEM-EDS analysis. 103
39 Deposition conditions of the sample SiPtCFOLNO 22. 106
40 Results of SEM-EDS analysis. 106
41 Observed Thornton's diagram zones for the LNO and CFO films studied. 109
42 Observed Thornton's diagram zones for the CFO-LNO films studied. 109

1 Introduction and dissertation structure

1.1 Introduction

Functional materials are of great interest due to being adapted for specific applications. The combination of different materials into one, such as in a thin film, combines the properties of the individual materials and opens new possibilities in terms of applications. Multiferroic composite materials are one such case, combining materials that individually have different types of ferroism. This opens the possibility of controlling the magnetization using an electric field and the polarization through a magnetic field through magnetoelectric coupling. This effect may be augmented in thin film form through strain engineering, in which the lattice mismatch between the two phases is exploited to considerably increase the coupling[2,1].

Building such a composite requires precise control over the film thickness and stoichiometry. While several techniques exist, deposition via pulsed laser ablation distinguishes itself by its ease of operation, versatility and film quality attainable at relatively low temperatures[18]. The use of a background gas allows precise control over the stoichiometry and a movable substrate holder allows the distance to the target to be changed. Together with the deposition temperature, these parameters provide great control over the resulting film microstructure and, consequently, the final film properties.

It was observed first by Movchan and Demchishin[19] that the microstructures and surface morphologies obtained could be classified into three general categories, based on the substrate's temperature relative to the melting temperature of the material to be deposited. This originated the first structure zone model for thin film deposition. Thornton[10] further developed this model by adding the influence of the background gas pressure and an additional zone. Since then other authors such as Messier[20] and Grovenor et al.[21] modified the model to account for parameters such as particle bombardment and substrate surface defects.

However, the process to determine the appropriate deposition conditions, namely the pressure and distance, for a certain material at a given temperature, is still performed on the basis of trial and error. As such, being able to at least predict the resulting microstructure for a given change in pressure and/or distance is relevant. Attending to the dynamics of the ablation plume's expansion in the background gas[8] provides this possibility, as a pressure-distance relationship can be established from it[22]. This allows the construction of a phase diagram for the observed film zone structures[23], according to their deposition pressure and target-substrate distance.

In this work, this process was applied to three systems: lithium niobate ($LiNbO_3$, ferroelectric) thin films deposited on Si and on Si (100) substrates covered with a Pt layer (SiPt), and bi-layer thin films constituted by a $LiNbO_3$ layer on top of a ferrite cobalt ($CoFe_2O_4$, ferromagnetic) layer, also deposited on SiPt substrates. All systems were deposited at 650 °C by pulsed laser ablation using a 248 nm KrF excimer laser. These materials are of great interest due to $LiNbO_3$ high piezoelectricity, ferroelectricity and electro-optical properties, and $CoFe_2O_4$ high magnetostriction, saturation magnetization, coercivity and magnetocrystalline anisotropy, giving them great potential for technological applications. The obtained

film's microstructure, surface morphology and stoichiometric content were studied using scanning electron microscopy techniques and energy dispersive spectroscopy. Study of the samples' cross-section was also performed using a focused ion beam. The effect of the deposition time on the film's microstructure was also investigated.

1.2 Structure of the dissertation

This work is constituted by 5 sections. Section 1 is the Introduction, where the motivation behind the work and a brief description of the study carried out, as well as the dissertation's structure, are presented.

Section 2 is the Theoretical Introduction where the main concepts relevant for this study are introduced: piezoelectricity, ferroelectricity, ferromagnetism, multiferroism and magnetoelectricity. The materials studied are presented as well. The basics behind pulsed laser ablation and the pressure-distance scaling law are explained, and the film growth modes and structure zone models are presented.

Section 3 is dedicated to the experimental aspects of the techniques used in this work, namely the experimental parameters that influence film growth in pulsed laser ablation and advantages and disadvantages of the technique. The characterization techniques used in this study are also presented, namely scanning electron microscopy, focused ion beam and energy dispersive spectroscopy. Finally, the equipment used is presented as well.

Section 4 consists in the Results and Discussion. The deposition conditions of the samples studied are indicated, the scanning electron microscopy images obtained are presented and information from them is discussed. This results in the classification of the samples studied into zones of Thornton's diagram. With this information, the pressure-distance scaling law is applied to the $LiNbO_3$ and $CoFe_2O_4$ films, resulting in phase diagrams of their microstructure and morphology in terms of zones of Thornton's diagram. The section concludes with the study of the deposition time's effect.

Section 5 compiles the conclusions derived from this study and makes suggestions regarding possible future work.

2 Theoretical introduction

2.1 Electric and magnetic materials

The crystal lattice of any solid falls under one of 32 possible classes. Of these, 11 are centrosymmetric, and as such have no polar effects, and 21 are non-centrosymmetric.[15] Due to this lack of symmetry, they may develop a spontaneous polarization (pyroelectricity) or present a polarization when subjected to a stress (piezoelectricity).

2.1.1 Piezoelectricity

Piezoelectricity is the property of a material displaying a potential difference after being subjected to mechanical stress or, conversely, manifesting a mechanical deformation under the application of an electric field.[1] This happens due to a mechanical stress inducing a polarization in the material according to:

$$P = d\sigma \tag{2.1}$$

where P is the polarization, d is the piezoelectric coeficient and σ is the mechanical stress. The converse effect is quantized by:

$$x = dE \tag{2.2}$$

where x is the mechanical deformation and E is the applied electric field.

2.1.2 Ferroelectricity

Ferroelectricity refers to the property of a pyroelectric material having two or more stable polarization states, in the absence of an electric field, and being able to switch between them when an electric field is applied.[1] This effect happens below a certain temperature - the material's Curie temperature - under which the negative and positive charge distribution centres in a unit cell do not coincide, giving rise to a spontaneous electric polarization.[15] As the temperature increases, at the Curie temperature there is a phase transition to a paraelectric state due to a transition to a high-symmetry structure[1] at high temperature, resulting in the disappearance of the electric polarization. This transition is termed first-order if it occurs abruptly and second-order if it happens continuously.

When a ferroelectric crystal transitions from the paraelectric to the ferroelectric state, its electric dipoles tend to align parallelly. However, the formation of the ferroelectric state turns this arrangement into a highly energetic one with a high depolarization field. To minimize the depolarization energy, different unit cells will align their dipoles parallelly but such that they are antiparallel to other set of unit cells, giving rise to ferroelectric domains.[15]

Ferroelectric materials preserve their electric polarization even after an electric field has been removed and as such display hysteresis cycles, which have characteristic information about the material.[15] One such cycle is represented in Figure 2.1 with the material's characteristics of interest: the saturation polarization in red, which is the maximum polarization that the material can attain due to the applied electric field; the remanent polarization in yellow, which is the polarization the material retains after the applied electric field is removed; and the coercive field in blue, which is the applied electric field necessary to remove the induced polarization.

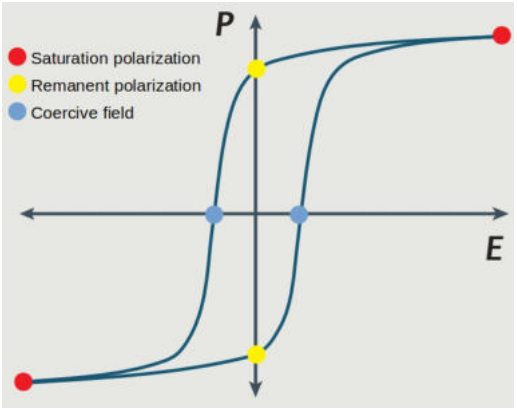

Figure 2.1: Hysteresis cycle typically seen on a ferroelectric, with different characteristics of interest of the material. Image adapted from Ref. [1].

2.1.3 Ferromagnetism

Ferromagnetism is analogous to ferroelectricity: a material displays a spontaneous and reversible magnetization when a magnetic field is applied to it. As the field increases, domain growth and alignment occurs until all reach the same alignment at the saturation magnetization.[15] This behaviour originates an hysteresis cycle, completely analogous to that presented in Figure 2.1, but with magnetization instead of polarization.

Similarly to ferroelectricity, ferromagnetism occurs below a certain temperature also termed as Curie temperature. Upon reaching it, a paramagnetic phase sets in and the material loses its permanent magnetization.[15]

2.1.4 Multiferroism and magnetoelectricity

Multiferroism is the property of a material possessing at least two of the properties of ferroelectricity, ferromagnetism and ferroelasticity. Magnetoelectricity consists in the property of an electric field changing both the polarization and the magnetization, and of a magnetic field changing the both magnetization and the polarization.[2] Figure 2.2 schematically illustrates the overlap of properties for each case.

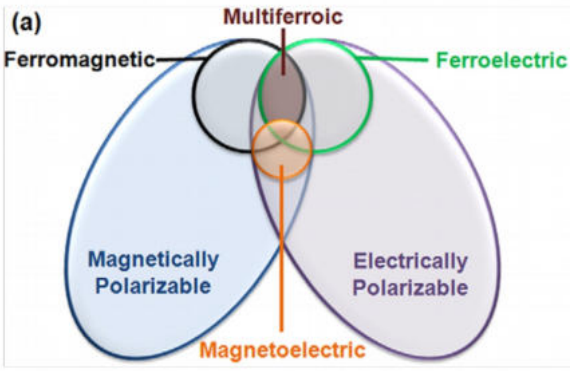

Figure 2.2: Schematic of the necessary overlap of electric and magnetic properties for multiferroism and magnetoelectricity. Image from Ref. [2].

In the case of multiferroic magnetoelectric materials, the strength of the coupling may be obtained experimentally by measuring either the current or voltage induced by an applied magnetic field (H), yielding the coupling parameter α[24]:

$$\alpha = \frac{\partial E}{\partial H} \tag{2.3}$$

where E is the electric field induced in the sample. However, the coupling parameter tends to be reduced in single-phase materials and magnetic and electric order occurs mostly at low temperatures.[15] An alternative to increase the coupling strength is to introduce an indirect coupling between two different phases via strain, such as a ferromagnetic (magnetostrictive) phase and a ferroelectric (piezoelectric) one[2,24], effectively creating a composite. Under the effect of a magnetic (electric) field, the magnetostrictive (piezoelectric) phase suffers a deformation which will be transmitted to the piezoelectric (magnetostrictive) phase via strain, giving rise to a polarization (magnetization).[15] Different composite geometries are possible with some examples being: vertical, columnar structures of one phase inside a matrix of the other[2]; horizontal multilayer composites, such as thin films on top of each other[2,24]; and particles of one phase inside a matrix of the other[15]. These geometries are illustrated in Figure 2.3.

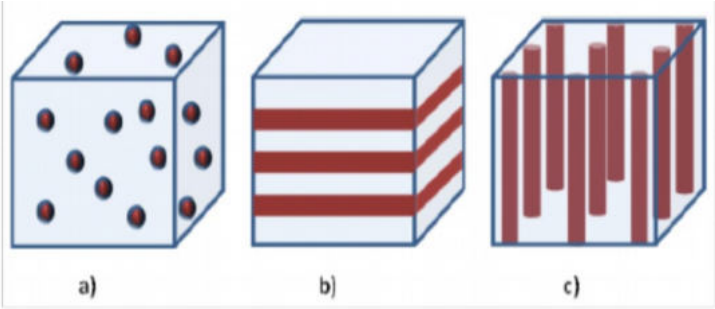

Figure 2.3: Different possible geometries for the multiferroic composites: a) particles inside a matrix; b) horizontal multilayer; c) vertical columns inside a martix. Image from Ref. [3].

The focus of the present study will be on horizontal multilayer composites.

2.2 Materials used

The materials used in this study were lithium niobate, cobalt ferrite, silicon (Si) and silicon with a layer of titanium oxide and platinum (SiPt).

2.2.1 Lithium niobate

Lithium niobate ($LiNbO_3$, LNO) is a material displaying piezoelectricity, ferroelectricity and electro-optical properties.[15] It has a reasonable piezoelectric coupling coefficient, making it attractive for ultrasonic applications.[25] Its melting point is at $\approx$ 1250 °C and its Curie temperature is $\approx$ 1142 °C.

The crystal structure is trigonal and lacks inversion symmetry. Above the Curie temperature, the Li atom is in an oxygen layer while the Nb atom is centered between oxygen layers, resulting in a non-polar phase[26], as shown in Figure 2.4, (a). As the temperature decreases to values below the Curie temperature, the elastic forces of the crystal move the Li and Nb ions to new positions, with the resulting charge separation inducing a polarization[26]. However, applying an electric field may reverse this polarization, as the Li ions move from above (below) the oxygen plane to below (above) it, with the Nb ions following but moving less. This is illustrated in Figure 2.4 (b) and (c) and is know as domain inversion.[4]

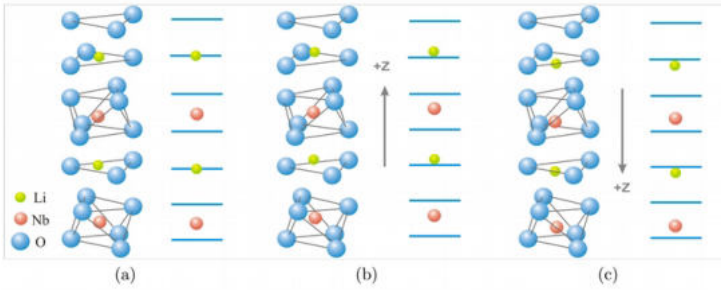

Figure 2.4: Atomic structure of LNO, showing the paraelectric (a) and ferroelectric (b),(c) phases. Image from Ref. [4].

2.2.2 Cobalt ferrite

Cobalt ferrite ($CoFe_2O_4$, CFO) is a ferromagnetic material displaying high magnetostriction, saturation magnetization, coercivity[27] and magnetocrystalline anisotropy, making it attractive for magnetoelectric applications.[28] It has an inverse spinel crystal structure with the octahedral sites occupied by eight Co^{2+} and eight Fe^{3+} ions, while the tetrahedral sites are occupied by eight Fe^{3+} ions, as shown in Figure 2.5.

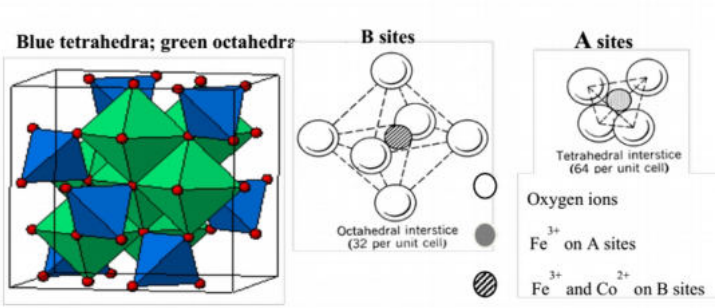

Figure 2.5: Crystal structure of CFO showing the octahedral and tetrahedral sites. Image from Ref. [5].

Its Curie temperature is at 790 K[27] ($\approx$ 518.85 °C) and its melting point is at 1575 °C[29].

2.2.3 Silicon-Platinum

The integration of ferroelectric and ferromagnetic materials with silicon (Si) may require an intermediate layer, as direct deposition on Si may result in reactions and oxidation due to the deposition temperatures typically used.[30,31] However, for most applications, this layer should be conductive to be used as an electrode for voltage measurements and application. Platinum (Pt) is one of the most common choices. It is a good conductor that is stable, oxygen resistant and does not react with most of the envisaged materials. Its adhesion to Si is poor, however, and it reacts with Si at 400 °C.[30] This is addressed with the use of intermediate layers that prevent reactivity and increase adhesion. Silicon oxide (SiO_2) and titanium oxide (TiO_x) are used for this. This results in a multilayer material as showed in Figure 2.6, in this work presented as silicon-platinum (SiPt).

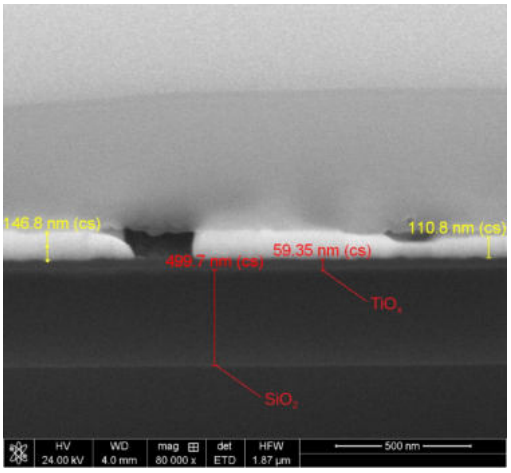

Figure 2.6: The layers of a SiPt substrate. The brightest layer (yellow measurements) is the Pt layer. Below the SiO_2 is the Si.

The nominal composition of the SiPt substrate is: Pt (150 nm)\$TiO_x$ (50 nm)\$SiO_2$ (500 nm)\Si(100).

2.2.4 Systems studied

Horizontal multilayer composites were used in this study. In particular, four systems were studied: LNO thin films deposited on silicon (Si) and silicon-platinum (SiPt) substrates; bilayer films of LNO and CFO on SiPt substrates; and a CFO thin film on a SiPt substrate. Figure 2.7 shows a schematic representation of these systems.

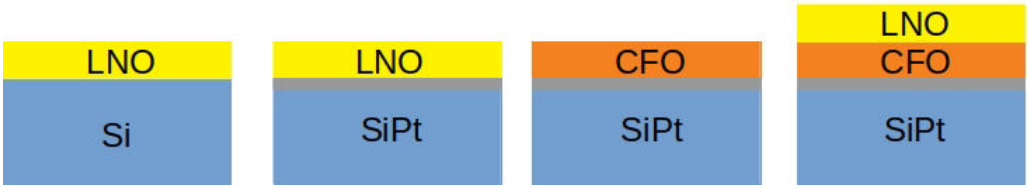

Figure 2.7: The composite systems investigated in the present study: LNO thin film on Si substrate, LNO thin film on SiPt substrate, CFO thin film on SiPt substrate and CFO/LNO bilayer film on SiPt substrate. The grey layer on the SiPt substrates represents the Pt.

2.3 Pulsed laser ablation

Pulsed laser ablation (PLA) is a technique which uses pulses of sufficiently energetic laser radiation to vaporize (or ablate) material from a target. Laser pulses are focused on a target made from the material to be deposited. Extremely fast heating of a small region of the target takes place, leading to boiling of the material and its vaporization and originating a so-called plume of ablated material that expands away from the target. This plume absorbs some of the laser radiation and ionization and excitation of its constituents takes place, resulting in plasma formation and optical emissions. Between laser pulses the target cools and resolidifies and the melted front recedes.[6] Figure 2.8 shows schematically the mentioned stages of the PLA process.

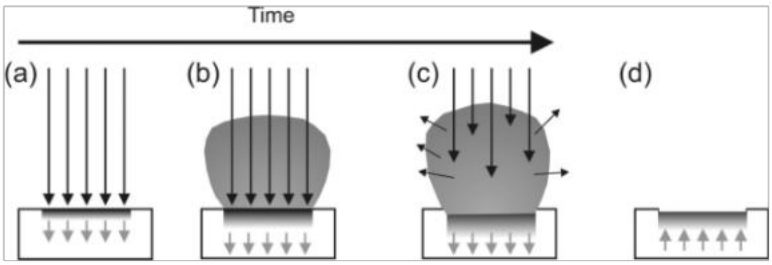

Figure 2.8: Schematic representation of the different stages of the PLA process. (a) Absorption of laser radiation (long black arrows) by the target and beginning of melting and vaporization. The shaded region represents melted material and the short arrows the movement of the melt front. (b) Vaporization increases originating a plume and the melt front progresses further into the solid part of the target. (c) The plume absorbs some of the laser radiation, originating a plasma and optical emissions (small arrows exiting the plume). (d) After the pulse stops the molten part of the target resolidifies and the melt front recedes. Figure taken from Ref. [6].

After a pulse ceases, the plume continues to expand away from the target and if a substrate is aligned

perpendicularly to the direction of propagation of the plume, deposition of the ablated material and consequent film growth takes place. This constitutes the process of pulsed laser deposition (PLD)

The deposition of a thin film by pulsed laser ablation (PLA) can be considered as constituted by 3 major steps: 1) ablation of material from the target, 2) plume expansion and 3) film deposition. The major theoretical aspects behind each step are presented in the following.

2.3.1 Ablation of material from the target - laser-target interactions

As the laser strikes the target, its photons are absorbed by the target's material according to Beer-Lambert's law:

$$I(x) = I_0 e^{-\alpha x} \tag{2.4}$$

where $I(x)$ is the photon's energy at depth x relative to the target's surface (considering a one-dimensional model), I_0 is the photon's energy and α is the absorption coefficient of the target's material. As the photons' energy is absorbed, different mechanisms that contribute to material ablation are activated. These mechanisms may be divided into primary and secondary mechanisms[32], with the former further divided in electronic, thermal and macroscopic sputtering. The mechanisms that are activated depend on the laser's parameters (wavelength and pulse duration) as well as on the target's properties.[6] For very short laser pulses, on the order of the picoseconds, electronic processes are relevant - the target's electrons are excited, originating a rise in the electron temperature which is transmitted to the lattice and eventually results in vaporization of material from the target.[7,6]

If, however, the laser pulse has a longer duration - in the nanoseconds for example, as is the case in the present study - then thermal processes will be of greater relevance.[6] The photons' energy is absorbed and diffused as heat in the target in a depth given by the thermal diffusion length[7] (L):

$$L = 2\sqrt{D\Delta t} \tag{2.5}$$

where D is the target's thermal diffusivity and Δt is the laser pulse duration. For ablation to occur, the temperature rise must be sufficient to at least reach the target's boiling point. This is favoured if the target has low reflectivity at the laser's wavelength, a large absorption coefficient and low diffusivity[6], as this maximizes the energy absorption and its concentration in a layer as small and close to the target's surface as possible, preventing its dissipation inside the bulk. The temperature at a certain depth x relative to the target's surface, at a given instant t since the beginning of the laser pulse, $T(x,t)$, is obtained by solving the 1D Fourier heat diffusion equation with the addition of a heat source[33,34,35]:

$$c\rho\frac{\partial T(x,t)}{\partial t} = I(x,t)\alpha + \frac{\partial}{\partial x}\left(k\frac{\partial T(x,t)}{\partial x}\right) \tag{2.6}$$

where c is the specific heat of the target's material, ρ is its density and k its thermal conductivity. $I(x,t)$

is the laser intensity profile, which will dictate how the laser energy varies with time and depth (the depth dependence is given by Equation 2.4), and it models the heating effect of the laser.

Regarding macroscopic sputtering, it usually only becomes relevant when large laser fluences are used, inducing explosive boiling of the target's material, or when the target is porous.[6]

Secondary processes are due to gas dynamics. As the plume of ablated material expands, if its density is high then the plume's constituents will collide and reach an equilibrium, with some being backscattered to the target.[6,32] This may induce secondary sputtering of material from the target.

For a nanosecond or longer laser pulse, the ablated material interacts with the laser, absorbing energy from it and undergoes ionization.[7,36]

2.3.2 Plume expansion

The plume of ablated material, constituted by neutrals, ions and electrons, expands away from the target's surface in all directions. If the density of ablated material is reduced, the particles don't experience any collisions and expand away from the target's surface freely. The velocity distribution for such a scenario would be Maxwellian.[6,32] However, the particle density in a PLA plume has been measured to be about 10^{15} $\sim 10^{16}$ atoms/pulse and the plume expansion velocity to be about 10$\sim$20 km/s[6,36], which translates into a very high density of material at the end of a typical nanosecond laser pulse. This means that at the early stages of the plume expansion the particles collide sufficiently for an equilibrium to be reached[32], with their velocity distribution following a shifted Maxwellian distribution:[6]

$$f\left(v_x\right) dx = N v_x^3 \exp\left(-\frac{m\left(v_x - u\right)^2}{2kT}\right) dx \tag{2.7}$$

where v_x is the velocity of one of the particles along the normal to the target's surface, N is the number of particles, m is the particle's mass, u is the plume's flow velocity and T is the average temperature in the plume. It is noteworthy that v_x can take positive or negative values[6,32] which means that some plume material may be backscattered, as mentioned before.

When the laser pulse ends, the transfer of energy and material to the plume is very reduced and considering the equilibrium reached in regards to the velocity distribution, the expansion can be considered adiabatic.[36]

The shape of the plume allows an estimation of the angular distribution of the plume's material, relative to the surface's normal. It is observed that the plume's shape follows a cosine power law of the form $f(\theta) = \cos^n(\theta)$[6,7,33,37], with $4 < n < 14$[37] and θ the angle relative to the surface's normal. A schematic representation of the plume shape according to this dependence is shown in Figure 2.9.

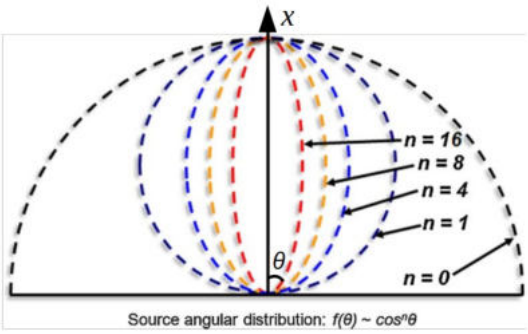

Figure 2.9: Schematic representation of the plume shape as dictated by a cosine power law for different values of the exponent. Image adapted from Ref. [7].

The angular distribution of the material in the plume is reflected in the film by an angular dependence of its thickness. As such, typical samples in laser ablation have 1×1 cm^2.

2.3.2.1 Expansion in a background gas - blast wave model

The presence of a background gas will constrain the plume expansion. In the early instants, however, the pressure in the plume is much higher than the pressures typically used for a background gas, and as such the expansion will proceed similarly to the vacuum case[36] as shown in Figure 2.10.

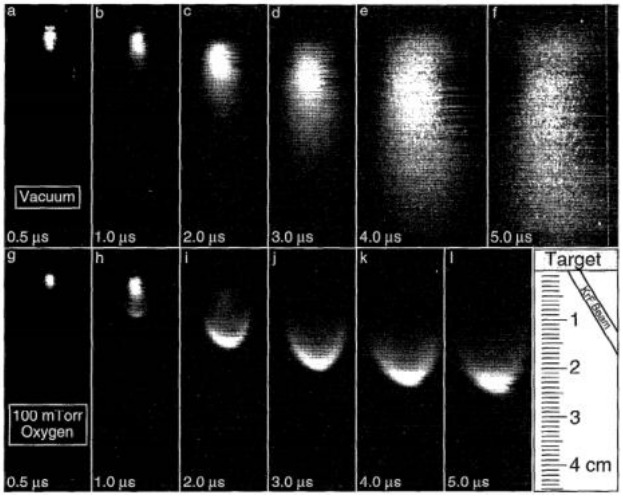

Figure 2.10: Photographs of the visible plasma emission from an YBCO (high-temperature superconductor ceramic) expanding plume during a PLA process, in vacuum (upper row of images) and in a background atmosphere of oxygen (lower row of images). Each photograph was taken at the indicated time after the laser pulse struck the target. The lower-right schematic shows the geometry of the experiment as well as the distance from the target that the plume reaches. Image from Ref. [8].

It is observed that before ≈ 1 μs the plume expansion is virtually the same both in vacuum and in an oxygen atmosphere. However, at ≈ 1 μs, a component at the front of the plume expanding in an oxygen atmosphere becomes visible, which is absent in the vacuum case and is typical of a shock front.[8] In the following instants, the visible emission comes from this front component only, whose progress is seen to slow quickly in stark contrast with the expansion in vacuum.

The ablation plume is constituted by two components - a slow-moving one, which stays close to the target, and a fast-moving one with a strongly forward-directed expansion.[8] These components are easily distinguishable in the images of the expansion in vacuum. The shock front is originated by the slow-moving component - the collisions experienced by its constituents with the background gas' particles excite the ablated species at the frontier between the plume and the background gas, originating visible emissions and pushing a layer of the background gas away from the target, giving rise to a shock wave.[36]

The propagation of the shock front can be modelled using a blast wave model[38], which considers that the shock wave is originated by a large release of energy E in a small volume of the background gas and in a reduced time interval. According to this model, the position of the shock front, D, at an instant t after the energy release is given by:

$$D(t) = \xi_0 \left(\frac{E}{\rho_0}\right)^{1/5} t^{2/5} \tag{2.8}$$

where ξ_0 is a constant and ρ_0 is the density of the background gas. For low pressures of the background gas, however, an exponent ≈ 0.6 in t provides a better description at early times.[8] To account for this possible variation, Equation 2.8 may instead be expressed as:

$$D(t) = \xi_0 \left(\frac{E}{\rho_0}\right)^{1/5} t^{n} \tag{2.9}$$

2.3.3 Pressure-distance scaling law

During the deposition process several parameters will influence the film's growth mode and morphology, consequently affecting its physical properties. Examples of these parameters are the deposition rate, the temperature of the substrate and background gas pressure.[7] The target-substrate distance, however, is another parameter of great impact with slight variations inducing significant changes in the film's microstructure.

Given a certain pressure, there is an optimal target-substrate distance for which the film's properties will be optimized.[22] Due to the collisions of the plume's constituents with the background gas, they lose energy as they traverse the target-substrate distance. If this distance is too great, they will arrive without enough energy to induce surface diffusion and the film becomes porous. On the other hand, if the distance is too small they will arrive with excessive energy and may damage the deposition surface.[22] As such, there must be an optimal distance for a given pressure at which the plume's constituents arrive with an adequate velocity. This relation may be found using Equation 2.9. Taking the derivative with respect to time yields the velocity of the shock front, v, and eliminating the time dependence yields:

$$v \propto P^{-0.2/n} D^{n-1/n} \tag{2.10}$$

where P is the pressure of the background gas. Assuming that the best quality films are obtained always for the same velocity[22] this yields the pressure-distance scaling law:

$$PD^{5(1-n)} = \text{constant} \tag{2.11}$$

2.3.4 Film deposition and microstructure

As the plume contacts with the substrate, its constituents condense on it and the film starts growing. This process may be thought of as occurring in three major steps: nucleation, coalescence and thickness growth.[9]

Nucleation consists in the condensation of the plume's constituents - atoms, for example - in the substrate's surface, where they diffuse and agglomerate together into nuclei. Upon reaching a critical size, a nucleus starts growing according to the mechanical equilibrium between the interfacial tensions of the film, vapour and substrate. This equilibrium is stated by Young's equation[7]:

$$\gamma_{sv} = \gamma_{fs} + \gamma_{fv}\cos\theta \tag{2.12}$$

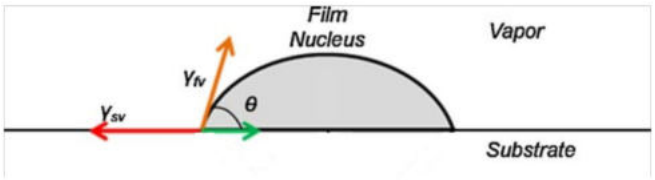

Figure 2.11: Nucleus of a film on a substrate and interfacial energies involved. Image adapted from Ref. [7].

where, attending to Figure 2.11, θ is the contact angle and γ_{sv}, γ_{fs} and γ_{fv} are the interfacial energies in the substrate-vapour, film-substrate and film-vapour interfaces, respectively. Three major growth modes are observed (Figure 2.12):

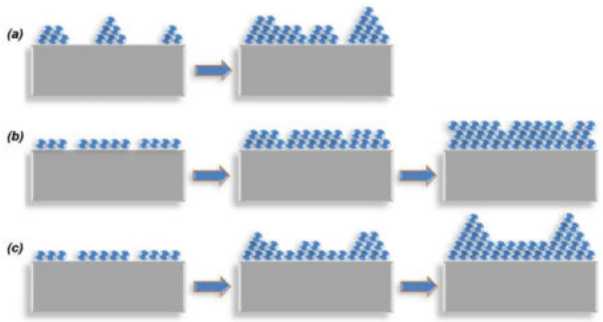

Figure 2.12: The three major growth modes: (a) island, (b) layer-by-layer and (c) layer-plus-island. Image from Ref. [7].

1) layer-by-layer or Frank-van der Merwe mode, in which the film's atoms are more strongly bonded to the substrate than between themselves, resulting in the growth of film layers on top of each other. In this case, $\theta \approx 0$ and $\gamma_{sv} \geq \gamma_{fs} + \gamma_{fv}$.

2) island or Volmer-Weber growth mode, in which the film's atoms are more strongly bonded to each other than to the substrate's atoms, resulting in the growth of isolated three-dimensional film clusters. In this case, $\theta \neq 0$ and $\gamma_{sv} \leq \gamma_{fs} + \gamma_{fv}$.

3) layer-plus-island or Stranski-Krastanov mode, which is a combination of the aforementioned modes - the film begins growing layer-by-layer but this becomes energetically unfavourable as the thickness increases and island growth mode sets in.

The next step in film growth is coalescence, in which isolated islands of film material grow until they make contact, creating a continuous network.[9] Depending on the energy available for surface and bulk diffusion, a boundary may result or not.

The final step is the growth in thickness. As the film grows, different factors influence the growth mode and the resulting microstructure - defects or irregularities on the deposition surface, the deposition rate, the temperature of the substrate and the background gas pressure are some examples.[7] Of these, irregularities on the deposition surface and the substrate's temperature will have particular impact on the film's microstructure due to shadowing, surface and bulk diffusion and recrystallization.[9,39]

Shadowing is an effect resulting from irregularities on the deposition surface, which may be due to defects on the substrate's surface, steps or the appearance of preferential growth directions during film growth. The surface's normal direction will be different on each of these morphological features, resulting in the incident plume atoms striking the surface in different directions. This results in the film growing in different directions on each point. As a consequence, in some regions the film may end up blocking - or shadowing - some regions of the deposition surface from the incident plume atoms, originating voids in the film's microstructure. This effect is more prevalent at reduced substrate temperatures[10,9], as the adsorbed atoms don't have enough energy to diffuse and overcome the morphological barriers.

Surface diffusion refers to the movement of the adsorbed atoms on the deposition surface and across surface grain boundaries. Enough energy is necessary for this process to occur and as such it is mostly seen at intermediate substrate temperatures.[9] However, other processes such as bombardment by arriving particles may also provide the necessary energy to the adsorbed atoms.[40]

Bulk diffusion refers to the movement of the adsorbed atoms within the volume of the growing film. This process requires considerable energy and as such is mostly prevalent at high substrate temperatures.

Recrystallization consists in a phase transition which changes the crystal orientation, resulting in the formation of grains with different orientations. It occurs when the film thickness is large and the substrate temperature is high.[9]

The substrate temperature will then have a decisive influence on the growth mode and film microstructure formed, as different processes are activated according to its value. The activation energies typically depend on the melting temperature of the film's material[9], T_M, and as such the substrate's temperature relative to it, T/T_M, may be used as a parameter to organize the observed film microstructures into

different regions[39]. This type of organization originates what are known as structure zone models.

2.3.5 Structure zone models

There are different types of structure zone models which use different parameters to organize the observed film microstructures. The first to appear was that of Movchan and Demchishin[19] which organizes the observed microstructure of deposited films in three regions according to T/T_M (Figure 2.13).

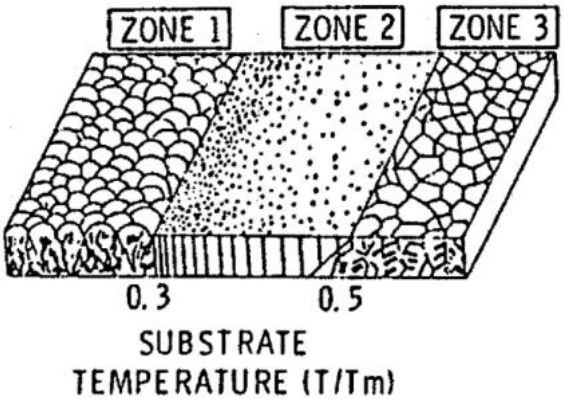

Figure 2.13: The structure zone model of Movchan and Demchishin (MD). Image from Ref. [9].

The MD model organizes the observed film morphology and microstructure in three regions of T/T_M:

- Zone 1, $T/T_M < 0.3$: the film's microstructure is constituted by tapered crystals separated by voids and with domed tops[39]. The crystal's internal structure lacks definition and exhibits a high density of dislocations, originating a fine-grained and porous structure[9]. The diameter of the crystals increases with T/T_M. This structure develops due to reduced surface diffusion, meaning that the deposited atoms stay essentially at the positions of landing.[9,39]

- Zone 2, $0.3 < T/T_M < 0.5$: the film displays a columnar microstructure separated by intercrystalline boundaries and the surface has a smooth appearance, with dislocations observed mostly at the boundaries.[39] Similarly to the previous zone, the grain size increases with T/T_M and at the upper limits may extend through the film's thickness. This process is possible due to considerable surface diffusion occurring.[9,39]

- Zone 3, $T/T_M > 0.5$: the film's microstructure is composed of equiaxed grains, with the grain size increasing with T/T_M.[39] This structure occurs due to bulk diffusion.[9,39]

Thornton built on the MD model by considering the influence of both T/T_M and the background gas pressure P on the morphology and microstructure of the deposited films. The analysis of the microstructure and surface morphology of thin films deposited by magnetron sputtering using Ar gas yielded the model shown in Figure 2.14.

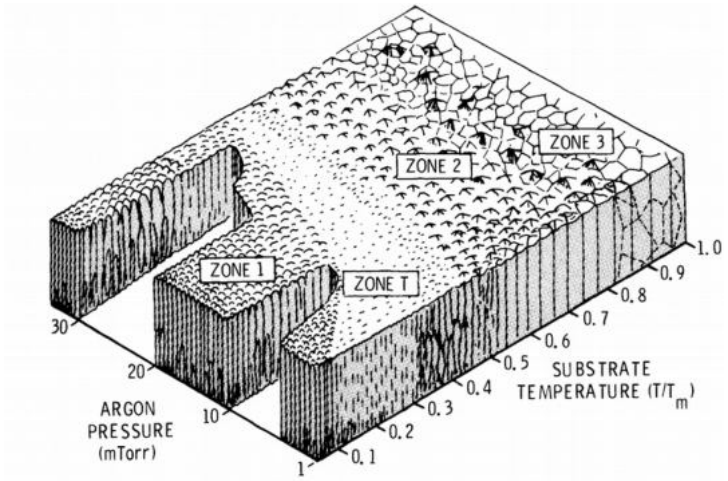

Figure 2.14: The structure zone model proposed by Thornton. Image from Ref. [10].

Thornton's model (from this point onwards in this text termed TD, Thornton's Diagram) presents three major differences relative to the MD model: the presence of four zones instead of three; the somewhat different ranges of T/T_M for the zones presented in the MD model; and the boundaries between the different zones have a different shape than those of the MD model, due to the additional dependence on the pressure.

The different zones of TD are:

- Zone 1, $T/T_M < 0.1$: the structure is similar to its equivalent in the MD model, with the film constituted by tapered crystallites with voids between them.[10] This structure develops due to the reduced substrate temperature, which doesn't provide enough energy for surface diffusion. As a consequence, shadowing effects will be relevant. Higher pressure of the background gas allows this zone to persist even if T/T_M is increased, due to adsorption of the gas molecules onto the deposition surface, which limit the mobility of the film's atoms.

- Zone T, $0.1 \lesssim T/T_M \lesssim 0.3$: this zone was introduced by Thornton due to the observation of a microstructure that didn't fit in either zone 1 nor 2 of the MD model. In this zone the intergrain voids observed in zone 1 begin to fill in, forming a dense array of poorly defined fibrous grains which generally do not extend through the film's thickness.[10,16] The surface appears smooth and with fine domes. This structure becomes possible due to the increased surface diffusion provided by the higher T/T_M, being dominant as long as the pressure remains low.

- Zone 2, $0.3 \lesssim T/T_M \lesssim 0.75$: this zone displays columnar grains which extend through the film's thickness and are separated by grain boundaries. At the upper end of the temperature range the surface tends to be constituted by faceted grains.[10] This zone's structure sets in due to the increased surface diffusion, with the pressure's influence having negligible impact (Figure 2.14.

- Zone 3, $T/T_M \gtrsim 0.75$: the film's surface displays smooth and relatively flat grains with grooved boundaries. Similarly to zone 2, the pressure doesn't seem to affect appreciably this zone's phase boundary[10] (Figure 2.14), with bulk diffusion being the dominant physical process by which it sets

in. The absence of equiaxed grains was noted by Thornton to be a possible consequence of reduced film thicknesses and lower deposition rates as compared to Movchan and Demchishin, and other studies seem to display them at this T/T_M range[39] so they should be considered as a feature of this zone.

Figures 1.13 to 1.18 show examples of the microstructure of the different zones, as observed by Thornton[10].

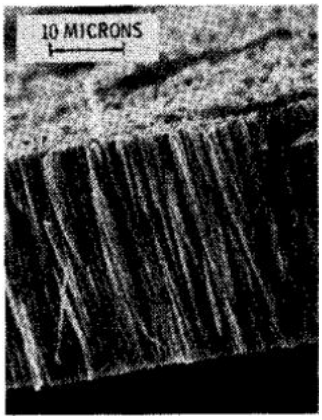

Figure 2.15: Microstructure of zone 1. Image from Ref. [10].

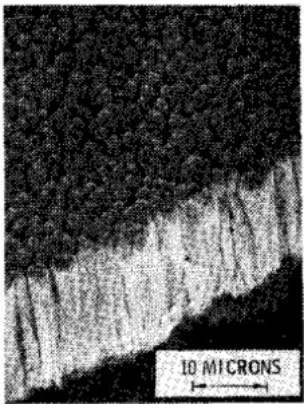

Figure 2.16: Another image of a zone 1 microstructure. Image from Ref. [10].

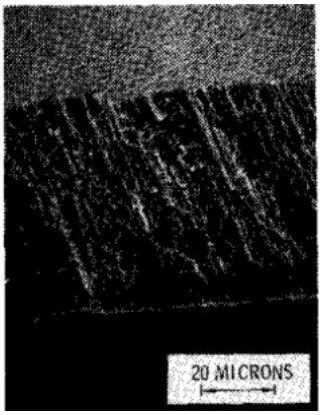

Figure 2.17: Microstructure of zone T. Image from Ref. [10].

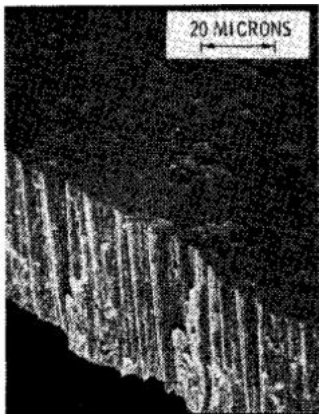

Figure 2.18: Another image of a zone T microstructure. Image from Ref. [10].

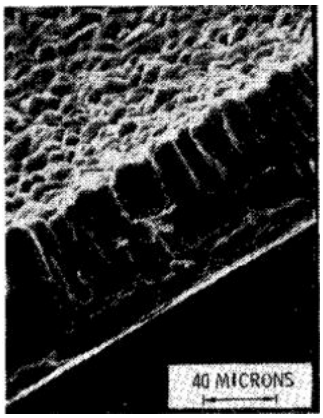

Figure 2.19: Microstructure of zone 2. Image from Ref. [10].

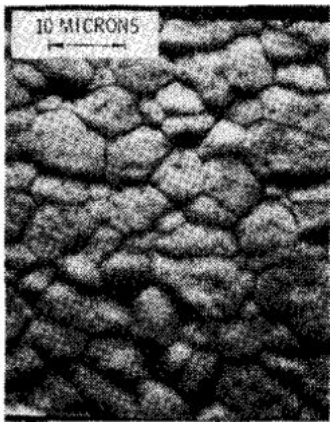

Figure 2.20: Microstructure of zone 3. Image from Ref. [10].

Despite having been developed using films deposited by sputtering, TD may be successfully applied to films deposited by other physical vapour deposition methods[39] such as PLD[23], making it suited for the present study. In the subsequent studies it will be used as a guide to organize and understand the growth of the produced laser ablation films.

3 Experimental techniques

There are various physical and chemical techniques through which thin films may be grown. Multiferroic thin films, in particular, have been deposited by sputtering, spin coating, pulsed laser deposition, sol-gel processes, among others.[7] The choice of technique is dependent on the material to be deposited and envisaged application. For complex oxide materials, one of the most suited techniques is pulsed laser ablation and was the one used in the present study.

Regarding the characterization of the produced films, their surface morphology and microstructure gives valuable information regarding the suitability of the deposition conditions used and, consequently, whether there is need for further tuning of their experimental conditions. Electron microscopy techniques are adequate to probe these characteristics and were used in the current study. The techniques used for the characterization of these thin films include scanning electron microscopy (SEM) and focused ion beam (FIB).

The film growth was conducted at the Laboratório de Filmes Finos do Centro de Física da Universidade do Minho. The electron microscopy characterization was performed at the facilities of the INL - International Iberian Nanotechnology Laboratory.

3.1 Film growth - Pulsed Laser Ablation

Figure 3.1 shows the typical setup for a PLD process. The target is placed in a vacuum chamber such that the laser strikes it. The substrate is placed on a substrate heater and aligned perpendicularly to the plume. The laser enters the chamber and strikes the target, originating the plume which expands away from it and deposits the material on the substrate. The target is rotated during the process to avoid repeated erosion of the same spot. Additionally, the process may be performed in a reactive atmosphere, such as O_2. This is particularly relevant when depositing materials with volatile components in order to obtain the intended stoichiometry.

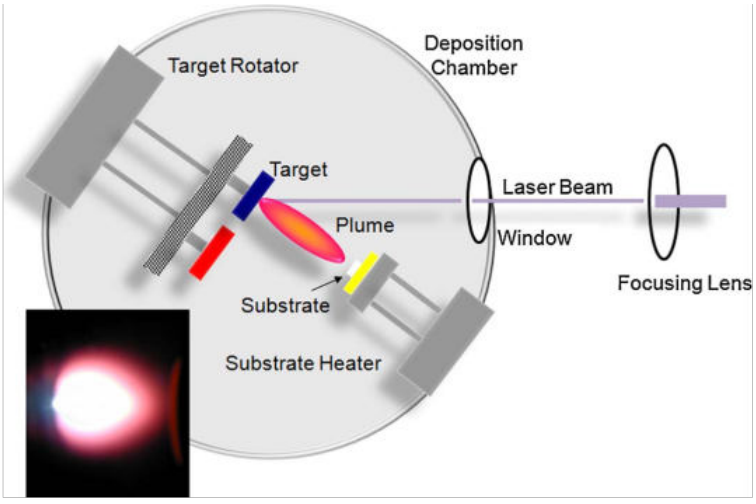

Figure 3.1: Schematic setup of a PLD apparatus. The inset picture shows a plume generated during the process. Image from Ref. [7].

3.1.1 Parameters that influence the deposition

Several parameters that may be controlled during the deposition influence the quality of the deposited film.

The substrate temperature is a crucial parameter. Higher temperatures increase the surface diffusion of the deposited species, which facilitates their movement into the equilibrium positions on the substrate and favours the formation of crystalline, epitaxial films with larger grain sizes. Additionally, lower deposition rates contribute to this effect, as the particles have more time to diffuse before more particles arrive. In contrast lower temperatures do not transmit as much energy for the diffusion process, which tends to produce amorphous films. The effect is increased by higher deposition rates as the particles don't have as much time to diffuse before more arrive and disturb the process.[6,33]

The laser wavelength, fluence and repetition rate are also parameters of importance. Regarding the wavelength, the penetration depth generally decreases with it and the ablated material has more kinetic energy. This means that upon impact with the substrate it has more energy to transmit to already deposited atoms, which enables their movement into the most favorable positions energetically. This results in smoother films.[6]

The laser fluence consists in how much energy is delivered to the target per unit area. The higher the fluence the more energy is delivered, increasing the ablation rate and the kinetic energy of the ablated species. This promotes an epitaxial growth of the film, similarly to the effect of the substrate temperature.[15] However, if the fluence is sufficiently high, macroscopic sputtering of large particulates from the target may occur through exfoliation[7] or explosive boiling[6], which may lead to particulate deposition on the film. The amount of ionized material in the plume also increases, which may lead to a blinding effect of the target and reducing the ablation rate.[15,41,42]

The laser repetition rate, or frequency, influences both the efficiency of the ablation process and the growth mode and epitaxy of the deposited film.[15,43] For a given fluence, if the repetition rate is too low, the laser energy that wasn't used in the ablation of the target will be dissipated as heat. If the repetition rate is higher there won't be time for it to dissipate and it may contribute to ablation with the next pulse, increasing the efficiency of the process. However, high repetition rates also promote an amorphous film structure, as the atoms already deposited won't have as much time to diffuse before more arrive.

Another relevant parameter is the pressure inside the chamber during the deposition. Two types of pressure can be distinguished: base pressure and work pressure.

Base pressure is defined as the pressure inside the chamber when a background gas isn't used, that is, when the deposition is performed in vacuum. It's a measure of the vacuum level - the amount of contaminants present during the deposition. Lower pressures mean less contaminants that may be deposited. As such, it has great impact on the quality of the deposited film.[15]

Work pressure is the pressure inside the chamber when a background gas is used. The use of a

gas may be necessary to obtain the intended film stoichiometry or to obtain a different film chemistry.[43] However, the presence of a background gas constrains the expansion of the plume and increases the probability of material re-deposition on the target's surface[6]. Additionally, the species in the plume collide with the gas molecules, reducing their propagation velocities and, as a consequence, the velocities with which they arrive at the substrate. This impacts the growth mode of the film.

The distance between the target and the substrate can also be controlled. Smaller distances increase the deposition rate[33] and for the same substrate temperature, laser parameters and pressure, seem to promote a denser and smoother morphology with large grain sizes. Epitaxy is also more strongly promoted.[23] Additionally, given the shape of the plume, the film thickness may vary across the substrate and smaller target-substrate distances minimize this effect.[33] However, if too small, inclusions may be deposited and the stoichiometry may not be correct. Furthermore, depending on the applications envisaged, a less dense film structure may be desirable in which case larger target-substrate distances are preferable.[23]

The target is also worthy of mention, as depending on its density and surface morphology, the ejection of larger particulates as splashing as well as exfoliation may occur. These larger particulates and droplets are deposited on the film, which usually is undesirable.[7,6] Denser targets with polished and smooth surfaces diminish these effects. Single crystals, ceramics and metal foils may be used.[15]

3.1.2 Advantages and disadvantages of the technique

PLD has several advantages compared to other deposition methods, namely: 1) the possibility of ablating nearly any material or combination thereof thanks to the large range of laser fluences and wavelengths possible[43]; 2) precise control over the growth rate of the film[43]; 3) the possibility of controlling the kinetic energy of the vaporized species allows control of the growth properties and modes of the film[43]; 4) the fact that the laser is independent of the vacuum system opens the possibility for different ablation geometries[43]; 5) the process occurs far from equilibrium and as such preserves well the stoichiometry, even when it's complex[7]; 6) is appropriate for rapid prototyping of materials and studying a wide phase space[7]. However, some disadvantages are also present: 1) possible ejection of large particulates which may resputter the deposited film and induce other defects[7,43]; 2) heterogeneous energy distribution in the laser pulse is reflected in a very directed plume with low angular energy distribution, which may in turn vary the film thickness across the substrate. To address this, the samples usually aren't larger than 1×1 cm^2[15,43]; 3) lighter elements propagate at different velocities and have different angular distributions in the plume when compared to the heavier ones, which is reflected in an angular heterogeneity of the chemical composition of the plume. This disadvantage can, however, be countered by an appropriate selection of a background gas and pressure during the deposition or a modified target composition in order to account for it.[43]

3.1.3 Equipment used

Figure 3.2 shows an image of the PLD deposition chamber used. It consists of a cylindrical stainless steel chamber with a diameter of 30 cm, to which two vacuum pumps are connected. These allow high-vacuum to be reached. The primary pump is an Alcatel Pascal 2010 I rotary vane pump, characterized by a pumping capacity of 9.7 m^3/h and a minimum pressure of 1×10^{-3} mbar. High-vacuum is reached with an Alcatel ADP80 turbomolecular pump capable of reaching speeds pf 27000 rpm. It has a pumping capacity of 288 m^3/h and can reach pressures on the order of 5×10^{-9} mbar. The pressure inside the chamber is monitored by a Pirani AML PGC1 pressure gauge controller, for pressures in the range $1 \times 10^{-3} - 10$ mbar, and by a Penning gauge for pressures under 10^{-3} mbar.[15]

The chamber has an inlet for a background gas, a rotateable target holder with capacity for 4 targets and a resistive substrate holder controlled by an Eurotherm 2116 PID temperature controller, capable of reaching 800 °C. The temperature is monitored by a thermocouple inserted in the substrate holder, in the area where the substrate is fixed. The substrate is fixed using silver ink. The substrate holder can be distanced from the target as desired until a maximum of 14 cm.

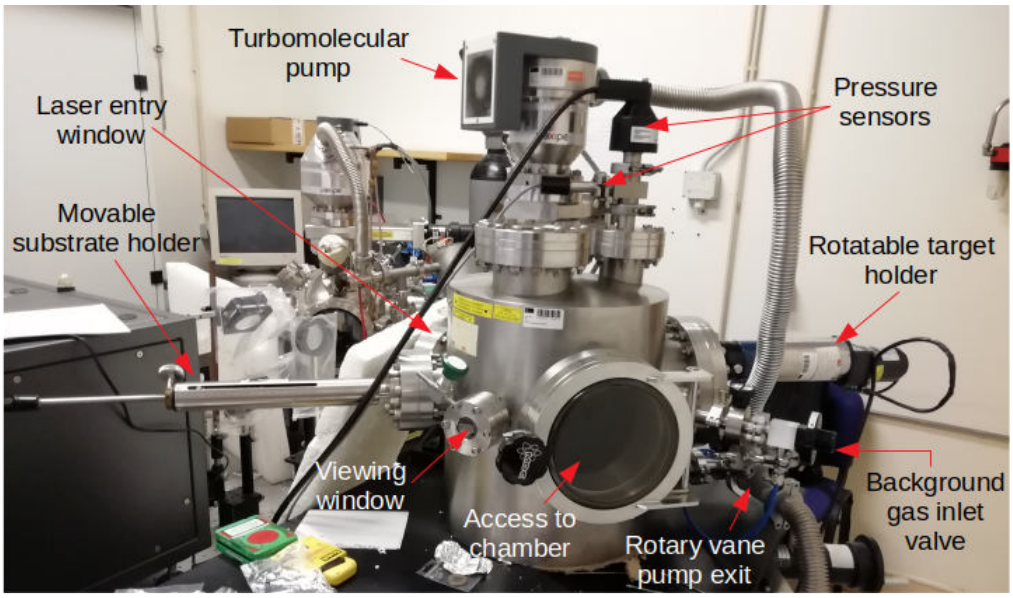

Figure 3.2: The PLD deposition chamber of the Laboratório de Filmes Finos do Centro de Física da Universidade do Minho.

Figure 3.3 shows the optical system used for the PLD. It consists of a Lambda Physik LPXpro 210 KrF excimer laser, with a wavelength of 248 nm, pulse duration of 25 ns (FWHM), maximum pulse energy of 800 mJ and a repetition rate of up to 100 Hz[44]. The laser beam passes by a beam-splitter (99/1) and is reflected by two mirrors into a lens of 50 cm focal distance. This lens focuses the beam, which enters the deposition chamber through a silica window and strikes the target at 45° relative to its normal.

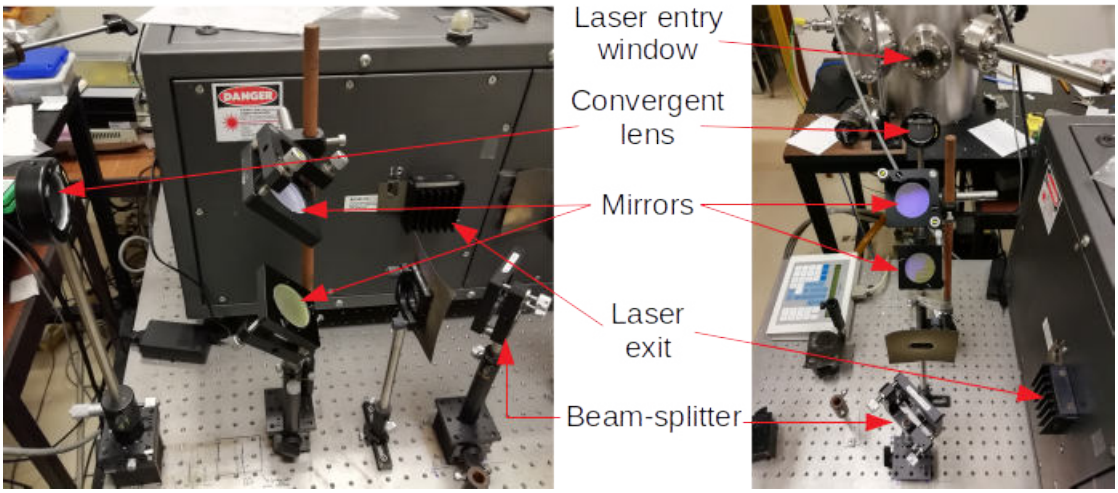

Figure 3.3: Optical system of the Laboratório de Filmes Finos do Centro de Física da Universidade do Minho.

Due to a malfunction on the substrate heater, some of the samples had to be deposited at room temperature. To increase their crystallinity they were subjected, post-deposition, to an annealing procedure in an oven. The oven used was a Carbolite MTF 12/38/250, capable of reaching 1200 °C (Figure 3.4).

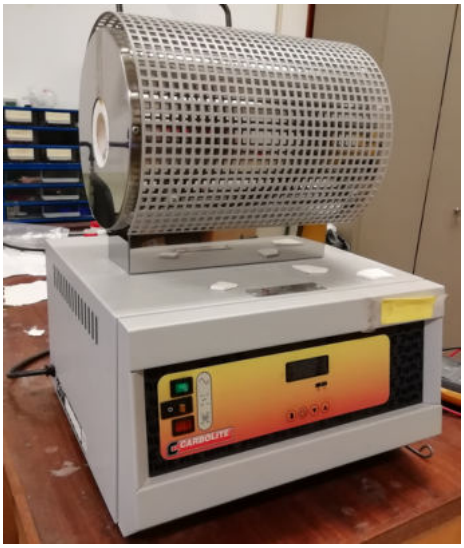

Figure 3.4: Oven used for sample annealing.

3.2 Characterization techniques

This section provides an overview of the principles behind the characterization techniques employed in this work.

The structure and morphology of the deposited films was investigated using electron microscopy techniques, namely SEM and FIB. The elemental and stoichiometric characterization was confirmed via energy-dispersive X-ray spectroscopy (EDS).

3.2.1 Electron microscopy

Microscopy is a valuable tool to observe small scale structures. However, even when considering a perfect optical system, the maximum resolution that a microscope can achieve - that is, its ability to distinguish two adjacent points as distinct - is limited by diffraction according to the Abbe diffraction limit[45]:

$$d = \frac{\lambda}{2n \sin \alpha} \tag{3.1}$$

where d is the smallest distance that can be resolved, λ is the wavelength of the probe used, n is the refractive index of the medium in which it propagates and α is half the angle with which it converges to the point observed. The resolution will thus improve if probes with smaller wavelengths are used. For light microscopes, considering light with a wavelength of about 400 nm, the maximum resolution achieavable is around 200 nm.[46] As such, light is not an adequate probe to observe smaller structures.

However, the discovery of the wave-particle duality and the confirmation of de Broglie's hypothesis:

$$\lambda = \frac{\hbar}{p} = \frac{\hbar}{mv} \tag{3.2}$$

where $\hbar$ is the reduced Plack's constant and $p = mv$ is the particle's linear momentum, revealed that sufficiently accelerated electrons could have wavelengths much smaller than those of light, and as a consequence could resolve structures that light could not and with much more detail. This led to the development of electron microscopy, which enables the visualization of the surface morphology and structure of materials at the micrometer to nanometer scales.

3.2.2 Scanning electron microscopy

Scanning electron microscopy is a technique that rasters the surface of a sample, in a xy pattern, with a focused beam of electrons. The interaction of the beam's electrons with the atoms and electrons of the sample generates different signals that give information about the sample's surface morphology, elemental distribution and stoichiometry.[14]

Figure 3.5 shows a schematic representation of the general structure of a scanning electron microscope (SEM). The main components of a SEM are the electron gun, which generates the beam of electrons, an anode to accelerate them to the desired kinetic energy (typically in the range 0.1 - 30 keV[14]), a set of magnetic lenses and physical apertures which narrow the beam and focus it on the sample, and a scanning coil which allows the rastering of the sample's surface with the beam. Detectors for the signals generated are also necessary, as well as a stage for holding the sample. The SEM has to be kept at high vacuum (below 10^{-4} Pa), to avoid undesired scattering of the electrons by atoms or molecules from atmospheric gases.[14]

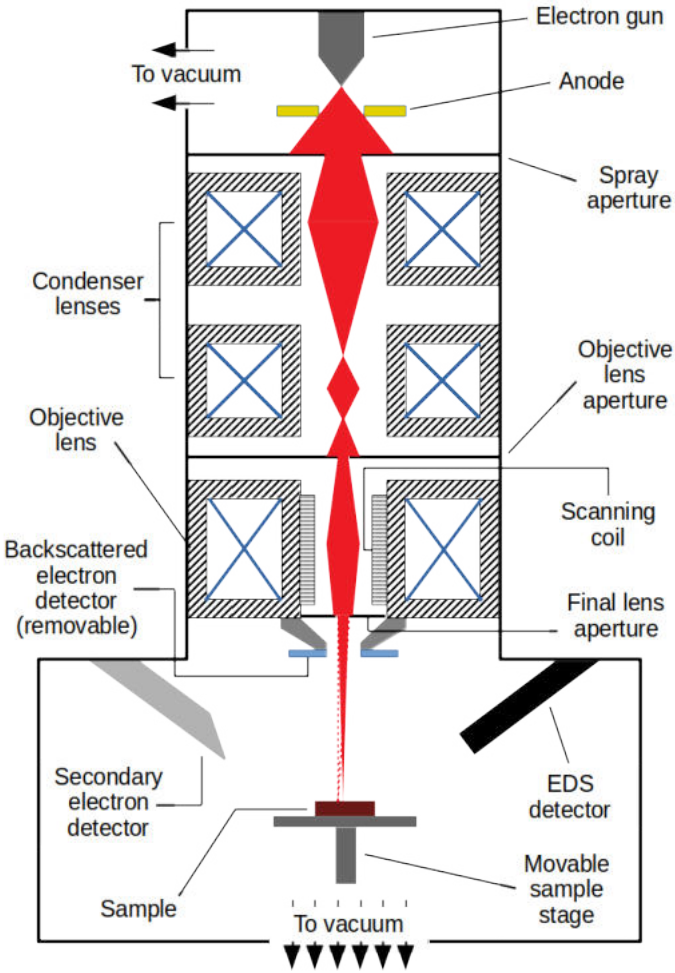

Figure 3.5: Cross-sectional view of the general structure and constituents of a SEM. The region above the backscattered electron detector is the microscope column; the region below it is the specimen chamber. The electron beam is represented in red.

3.2.2.1 Signals generated

When striking the sample, the beam's electrons experience elastic and inelastic scattering with the sample's atoms and electrons, giving rise to different signals: secondary electrons (SE), backscattered electrons (BSE), characteristic X-rays and Auger electrons. These signals are captured by the different detectors inside the SEM chamber and provide different information about the sample.

Figure 3.6 shows a schematic representation of the interaction volume - the volume through which the beam's electrons are scattered - and the different depths from where the different signals originate. Despite the small size of the electron probe at the sample's surface, the beam's electrons can be scattered throughout a volume with linear dimensions orders of magnitude larger.[13] This volume is affected by the accelerating voltage of the electron beam and by the atomic number and density of the sample's elements: higher accelerating voltages increase the penetration depth and widen the volume, but higher atomic numbers decrease the penetration depth[13] and higher densities decrease the scattering range.[47]

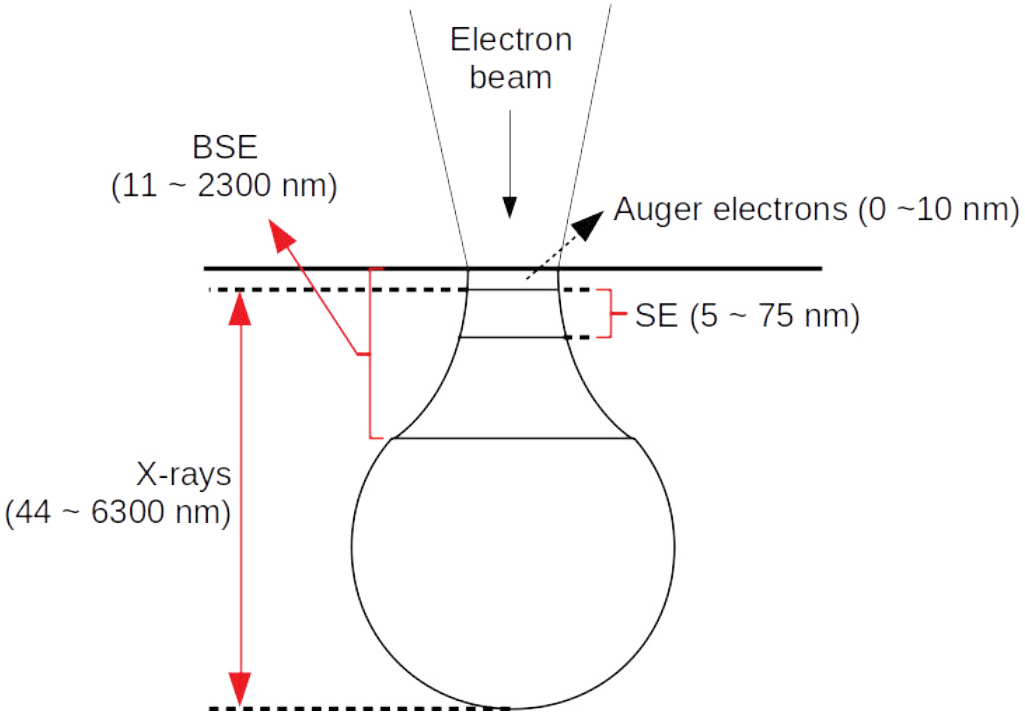

Figure 3.6: Schematic representation of the interaction volume of the electron beam with the sample, with the different signals generated and corresponding depth of origin. The values shown were taken from Ref. [11](Auger electrons), Ref. [12](SE), Ref. [13](BSE) and Ref. [14](X-rays).

Depending on the nature of the scattering different signals will result. Inelastic scattering occurs when a beam electron is scattered by an electron of a sample's atom, transfering its energy to it and possibly removing it from the atom.[13] If it is a valence electron, it constitutes a SE. However, given the reduced energy of SEs (typically below 50 eV[13,47]), only those close to the sample's surface actually escape it, which means that the SE signal detected comes mostly from the surface. For this reason the SE signal carries mostly topographic information. This also means that regions of the sample where the electron beam strikes the surface obliquely, rather than perpendicularly, will emit more SEs as a larger part of the interaction volume will be at the surface, a phenomenon called edge effect.[47]

However, if the electron removed by the scattering event is not a valence electron, then an electron from an outer shell of the atom will fill in the hole created. The atom emits X-rays in this process, with energy equal to the difference between the electron energy in the shells involved in the process. As the electronic energies in the atoms of the different elements are well defined, these X-rays can identify the element that emitted them, earning them the name of characteristic X-rays.[47] This signal may be used to confirm the elements present in the sample and their stoichiometry.[14]

However, instead of emitting a characteristic X-ray, the energy may be transfered to another electron from the outer shell resulting in its emission, a process known as Auger effect. The Auger electrons result from this process and have specific kinetic energies, allowing identification of the atomic element that emitted them.[14]

A beam electron may also undergo elastic scattering, in which case it is scattered by the atomic

nucleus of a sample's atom. In this case the energy of the electron is mostly conserved and it is simply deflected, constituting a BSE if it exits the sample.[13] Since their energy is conserved, BSEs are able to escape the sample even after penetrating considerably, which means the signal carries information from deep within the sample.[47] They are influenced by the atomic number of the sample's atoms, with higher atomic numbers deflecting more strongly and increasing the signal - this makes regions with higher atomic number elements appear brighter in a BSE image, making it an appropriate signal for imaging compositional variations.[47]

3.2.2.2 Beam parameters

The different components in the microscope column will act on the electron beam, changing different parameters that impact the quality of the image obtained. Figure 3.7 is a cross-section representation of the beam as it exits the final lens aperture and strikes the sample, with these different parameters indicated.

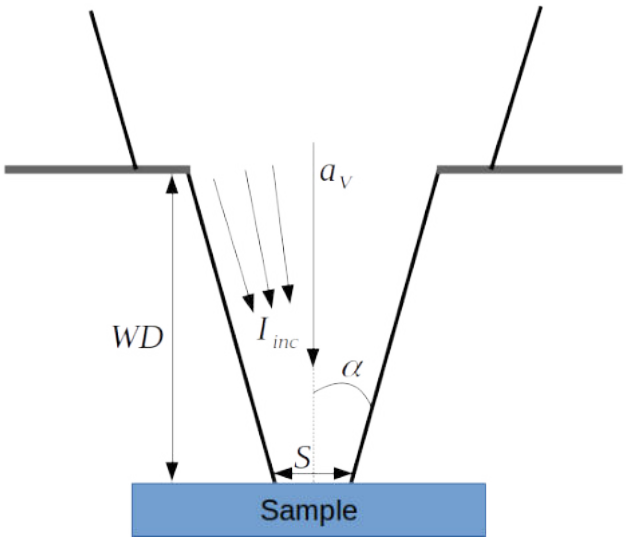

Figure 3.7: Cross-sectional view of the electron beam after exiting the final lens aperture, with the major beam parameters that affect the image obtained. a_v is the accelerating voltage applied to the electron beam, I_{inc} is the incident current, α is the convergence angle and S is the spot size. WD is the working distance.

The accelerating voltage, a_v, is the voltage applied by the anode to the electrons emitted by the gun. It sets the energy with which the electron beam strikes the sample, influencing the penetration depth of the beam and the resolution of the image obtained.[47] Higher accelerating voltages increase the penetration depth and as such increases the amount of electrons emitted from deeper layers of the sample. The image thus obtained becomes a superposition of information from the surface and information from within the sample. If the acceleration is high enough, the surface detail may be completely lost. However, higher accelerating voltages also decrease the effects of chromatic aberration.[14]

The incident current or probe current, I_{inc}, is a measure of the number of beam electrons that strike the sample. It affects the number of secondary electrons emitted from the sample and as such influences the signal-to-noise ratio and image contrast. Higher currents increase the signal-to-noise ratio and improve

contrast[47] at the cost of increasing the probe size and diminishing the resolution.[14] This parameter is controlled by the condenser lens and apertures' size mostly, but the accelerating voltage also influences it.[13]

The convergence angle, α, affects the depth of focus - the ability to keep sample structures at different heights both in focus. Smaller convergence angles increase the depth of focus but at the expense of probe current.[13] It is controlled by the aperture's size.

The spot size, S, is the size of the electron beam at the surface of the sample. It influences the resolution of the image and the incident current, I_{inc}. Smaller spot sizes increase the resolution and can resolve smaller structures and details, but decrease I_{inc} and consequently the image contrast.[13] This is controlled by the condenser lens.

The working distance, WD, is the distance between the sample's surface and the final aperture. It influences both the image resolution and the depth of focus, with longer distances diminishing the former but increasing the latter.[14] It is controlled by the vertical movement of the sample's stage, but is also affected by the objective lens' strength.

3.2.2.3 Components of the SEM

The beam parameters mentioned previously are controlled by the different constituents of the SEM (Figure 3.5). A general overview of them follows.

The electron beam originates in the electron gun, with three main types available: thermionic emission guns, field-emission guns and Schottky-emission guns.

The thermionic emission gun emits electrons by thermionic emission - a current is applied to a thin filament, heating it to the point where electrons acquire enough energy to overcome the work function of the filament's material. They are then accelerated by an anode with a hole at its center, allowing the beam to pass. Tungsten may be used for the filament but a LaB_6 single crystal or coating is also a possible choice.

The field-emission gun uses quantum tunneling to emit electrons. The emitter consists of a thin tungsten wire with a tungsten single crystal welded onto it, whose tip is extremely thin ($\approx$ 100 nm wide[47]). Positioned below the emitter is an anode. When a high voltage is applied between the anode and the emitter, the strong electric field generated is enough to remove electrons from the tungsten crystal. The electrons pass through a hole in the center of the anode and acquire their acceleration through a second anode positioned below. The tip of the crystal must be very clean and this type of electron gun requires ultra high vacuum conditions for proper operation.[47] The advantages it offers compared to the thermionic emission gun are an electron beam with much smaller beam width, which allows high resolution imaging, and a reduced spread of the electron's energies, which determines the resolution when imaging in low-accelerating voltage conditions.[47] Additionally, the emitter has a much longer lifetime and its brightness is 2 to 3 orders of magnitude greater.[48]

The Schottky-emission gun combines the thermionic emission and field-emission effects. The emitter

is the same as in the field-emission case with the difference that the tungsten crystal is coated with ZrO, which lowers the work function considerably. The strong electric field applied further contributes to this effect, and consequently a large current by thermionic emission is possible at lower temperatures compared to the thermionic emission gun.[47] However, the energy spread of the electron beam is larger when compared to the field-emission gun, which may affect the resolution in low-accelerating voltage imaging.

The condenser and objective lenses consist of magnetic lenses - coils of electric wire through which a direct electric current passes, giving rise to a magnetic field around them. The coils are placed inside a metal yoke with a narrow part, the polepiece, which concentrates the magnetic field lines.[47] This generates a strong magnetic field which affects the trajectory of the beam electrons. Changing the current affects the field's strength, allowing control over the width of the beam. The condenser lens controls this width, increasing or decreasing the amount of electrons that eventually pass through the objective lens aperture (see Figure 3.5) and thus also controlling the beam current that reaches the objective lens. This impacts the image contrast and signal-to-noise ratio, important parameters for image quality.

The objective lens focuses the beam on the sample's surface. If its magnetic field is too strong the image will appear underfocused, and if it is too weak it will appear overfocused.[14]

The apertures are thin metal plates with very small holes that are centered with the optical axis of the beam. They stop electrons that are too far from it, either due to emission at large angles from the electron gun or due to strong deflection by the condenser lens. This is important to maintain a narrow beam and consequently obtain a small probe on the sample's surface but also to avoid spherical aberrations on the beam.[47,49] The final lens aperture has the additional effect of changing the convergence angle of the electrons on the sample, which affects the depth of focus of the image.[49,13]

The scanning coils continuously change the position where the beam strikes the sample, performing a rastering pattern and giving the SEM its scanning capability (ilustrated by the dashed, red line in Figure 3.5). They also influence the level of magnification by defining the area to be scanned.[49]

Different detectors are necessary for the different signals produced. For secondary electrons an Everhart-Thornley (ET) detector is used. It consists of a scintillator placed within a Faraday cage to which a bias voltage of a few hundred volts is applied, attracting the secondary electrons emitted from the sample.[47] A much larger voltage, on the order of 10 kV, is applied to the scintillator, further attracting the secondary electrons and accelerating them. Their interaction with the scintillator generates light, which is guided into a photomultiplier tube and then converted into an electric signal. This signal is amplified and displayed on the computer screen as a brightness value for each pixel, originating the grayscale images characteristic of SEM.[49]

For backscattered electrons a different detector is used. The main types available are scintillation detectors and semiconductor detectors.[14] The working principle of the scintillation detectors is the same as the ET detector but without the need for a Faraday cage. Regarding the semiconductor detectors, the

backscattered electrons that reach it experience inelastic scattering in the semiconductor material, promoting some of its electrons to the conduction band. By applying an electric field the electrons are accumulated on surface electrodes in the detector, and the corresponding current progresses to an amplification and display stage similarly to the described for the ET detector. The semiconductor detector consists of a small ring of semiconductor material, with surface electrodes on both faces, which can be attached to the hole through which the electron beam exits the microscope column, in the final lens polepiece[14] (as ilustrated in Figure 3.5).

The characteristic X-rays emitted can be detected with an EDS detector.

The sample is attached to a movable stage which can move vertically, changing the working distance - the distance between the sample's surface and the final lens polepiece - and thus the depth of focus. The sample stage may also be rotated or tilted.

Finally, the specimen chamber usually features an infrared camera to observe the interior of the chamber and the movements performed with the stage.

3.2.2.4 Charging and beam damage

Depending on the material of the sample, the irradiation with the electron beam may originate undesirable effects such as charging or beam damage.

Charging occurs when there is an inbalance between the amount of electrons arriving at the sample and the amount leaving. This may happen with insulating materials, as is the case of the dielectrics used in this study. With conducting materials the beam's electrons can easily flow through the material onto the sample stage and from there to the ground. In the case of an insulator, however, the beam's electrons don't flow easily to the stage and remain on the sample.[47] As more electrons arrive, charge accumulation begins to develop. As a consequence, the SE emission may be increased or decreased according to whether the charging is positive or negative, originating dark or bright regions respectively in the SE image. In more extreme cases, beam displacement or even total deflection may occur.[14]

To eliminate charging the most common strategy is to coat the sample with a thin layer of a conductive material, ideally one that may form a continuous layer with no structure. The material should also have a high SE yield, so that there is no loss of information. Gold-palladium alloy, Pt, Cr or Ir are suitable choices.[14] Another possible strategy is to decrease the accelerating voltage of the electron beam, as lower values increase the electron yield from the sample.[14] By doing this a balance between the arriving and emitted electrons can be achieved, effectively eliminating charging.[47] Tilting the sample is another possibility which exploits the already mentioned edge effect to increase the SE emission and thus achieve charge balance. However, this technique may only be viable in relatively flat samples.[47] Using a fast scan rate coupled with frame integration may also be of help[13], as the electron beam doesn't stay on each spot for as long, reducing the amount of electrons that arrive on the sample. Visualization with BSEs may also

be a strategy, as their increased energy facilitates their escape from the specimen and thus contributes to charge balance in the sample. [13]

There is also the possibility of visualizing the sample not in high vacuum, as usual, but with a reduced pressure of an ionized gas inside the specimen chamber. This is called Low Vacuum SEM (LVSEM). By introducing a reduced pressure - in the order of tens to hundreds Pa [47] - of a gas, the electron beam and the emitted BSEs and SEs suffer inelastic colision with the gas molecules, ionizing them. The areas of the sample that experience charging will then attract the oppositely charged particles - either the positive ions or the free electrons - according to the sign of the charge accumulated, resulting in its neutralization. Furthermore, the gas molecules, ions and free electrons may penetrate into regions of the sample that could be difficult to coat, such as crevices or deep holes, and help in establishing a conducting path. [14] LVSEM may also be used to observe samples that are unstable in high vacuum, frozen samples containing water or porous samples. [47] In the case of frozen samples, the high pressure of LVSEM prevents the ice from sublimating. For porous samples, high vacuum may take a very long time to be reached, so the low vacuum mode is a quicker way to observe the sample.

LVSEM was used for some samples in this study, as the effect of charging made their observation difficult in high vacuum mode.

The electron beam may damage some materials. As it strikes the sample, the beam loses energy and generates heat which may damage the sample if the material is not heat resistant. This is frequently the case with polymers and biological samples [13]. If the material has volatile components they may be evaporated, leading to mass loss, collapse or swelling. These effects may even induce image drift due to the changes occuring. [14] Reducing the beam current and dwell time, as well as low magnifications whenever possible help to prevent this. A common strategy is also to adjust the beam's focus and astigmatism in another region of the sample before moving to the region from where images are intended, as this reduces the exposure time.

Another effect of beam damage is contamination. It refers to the presence of an unintended substance in the sample that suffers damage when struck by the electron beam, leaving a deposit of undesired material on it. Hydrocarbons are a common source of this effect, leaving a deposit of carbon on the sample's surface after interaction with the beam [14], contaminating it. The contamination is visible, when lowering the magnification or moving the stage, as a rectangular region with different contrast caused by the different SE yield due to the deposited material.

Another effect that may occur is, contrary to contamination, the removal of a layer of material by the beam. This is known as etching [50] and is visible in the same way as contamination. Distinguishing between the two effects is usually possible by comparing the observed brightness in the scanned region with the rest of the sample, and considering the SE yield of the material studied.

To avoid contamination or ecthing both the SEM and the sample should be handled and kept as clean as possible. Plasma cleaning also presents itself as a good strategy if the sample can undergo the procedure. [14] Another possibility is cryoshielding the sample. [50]

3.2.3 Energy dispersive X-ray spectroscopy

To confirm the elements present in the sample and their stoichiometry, energy dispersive X-ray spectroscopy (EDS) was used. This technique uses the characteristic X-rays detected since their energy is specific to each element, and their intensity is proportional to the concentration of the element.[47] The principle by which the X-rays are generated has already been explained but some detail can be added about the EDS detector and how it works.

There are different types of EDS detectors. EDS Detectors in principle are made of semiconducting material and the X-rays that arrive on them excite electrons to the conduction band, giving rise to electron-hole pairs. X-rays with different energies originate different current values, so measuring the current allows identification of the X-ray energy and hence the corresponding element.[47]

The accelerating voltage of the electron beam should be selected according to the energy of the X-rays that are expected.

It should also be noted that the actual area of the sample that is excited may be much bigger than the area selected for analysis. This is due to the scattering of the electron beam inside the sample in all directions, generating X-ray emissions from the whole region. Decreasing the accelerating voltage reduces the excited area but given the minimum acceleration needed for X-ray emission this has a limit. This uncertainty in the region of origin of the X-rays introduces some uncertainty in the precise mapping of the elements in the sample.[47] This uncertainty also extends to the quantitave analysis capability, given the possible absorption of the X-rays inside the sample or their loss to excitation of X-rays of other elements, as well as the possible overlapping of certain X-ray's energies. However, there are methods to take into consideration the possible absorptions and correct the quantitative analysis, known as matrix corrections.[14] Despite these uncertainties, EDS remains a reliable technique to confirm the elements present and obtain an estimate of their stoichiometry.

3.2.4 Focused ion beam

The focused ion beam (FIB) is a technique virtually equivalent to the SEM but where a beam of positive ions is used instead of an electron beam. Given the much greater mass of an ion comparatively to an electron, if it is accelerated sufficiently it may remove material from the sample it strikes. Allied with a resolution of ≈ 5 nm[51], this gives the FIB the ability to mill structures with extreme precision. Applications of this ability include the milling of a cross-section in a thin film, allowing the measurement of the film's thickness and visualization of its internal structure, as well as preparation of sufficiently thin samples of the film - lamellae - for (scanning) transmission electron microscopy ((S)TEM) analysis.

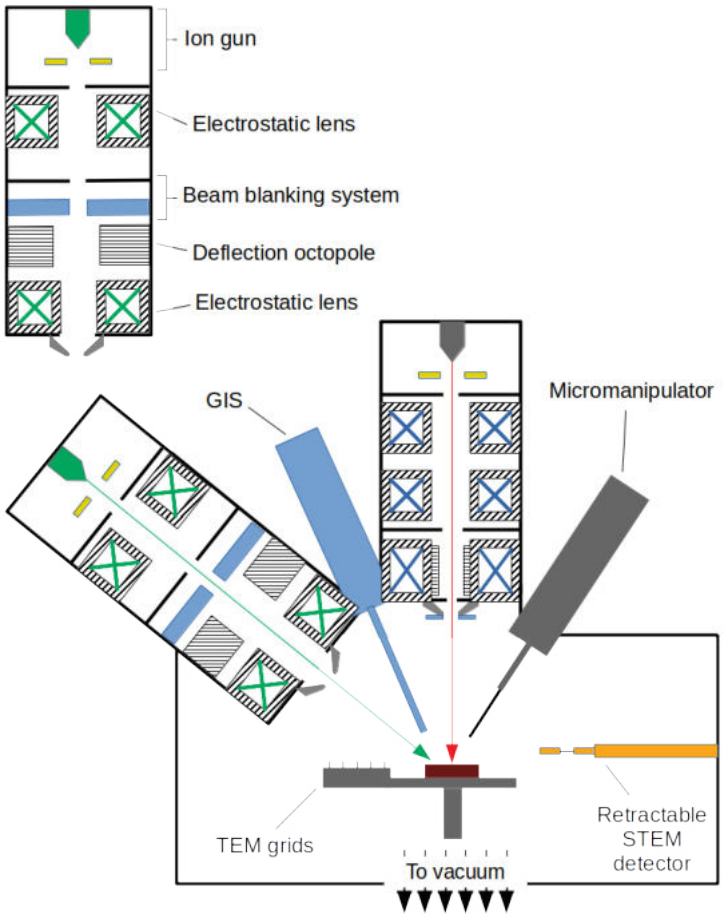

Figure 3.8: Cross-sectional view of the general structure of a Dual Beam FIB-SEM. In the top-left, the general constituents of the ion column are indicated. The electron beam is represented in red and the ion beam in green. The sample chamber also features SE, BSE and EDS detectors but these are not represented.

FIBs may be individual instruments or they may be integrated together with a SEM in the same machine, constituting a Dual Beam FIB-SEM. A schematic representation of the Dual Beam FIB-SEM is shown in Figure 3.8, as one such was used in the present study.

The SEM column's structure and constituents are as presented before. The ion column is very similar to the SEM column in the sense that it is constituted by a beam source, lenses to produce a finely focused beam on the sample's surface and apertures. However, there are key differences.

The beam source in a FIB is usually a liquid metal ion source, with Ga being the most common element used for the ions.[14] This type of source consists of a field-emission gun coated by the metal from which the ions are to be obtained. The field-emission gun is heated to the metal's melting point and a large voltage is applied to it. The balance between the surface tension forces on the metal and the electric field applied makes the liquid acquire a conical shape. This cone eventually acquires a tip sufficiently thin for field-emission of metal ions to occur.[52]

The lenses used in the FIB differ from those used in the SEM. In the latter, electromagnetic lenses are used. However, given the much higher mass of an ion compared to an electron, this type of lens will not be able to produce a finely focused beam, with electrostatic lenses having to be used instead.[14]

The ion column also includes a beam blanking system, which blocks the beam when it is not in use,

and a deflection octopole, responsible for rastering the beam across the sample's surface. The column is placed at a certain angle relative to the SEM column. This angle may vary slightly according to the equipment's manufacturer but usually is around 52°. The sample's stage is tilted by this amount when the ion beam is to be used, such that it strikes the sample normally. However, to ensure that both the electron beam and the ion beam strike the same spot on the sample, it must first be moved to the eucentric height - the stage height where tilting the sample doesn't move the region imaged. This is performed using the electron beam.

The FIB also features an additional stage, adjacent to the regular stage, where TEM grids are placed to receive the produced lamellae. It also possesses a micromanipulator - a long needle capable of very precise and minute movements - which is used to lift-out the lamella from the bulk sample and a gas injection system (GIS in Figure 3.8), to introduce a precursor gas into the sample's chamber for beam induced deposition.

Several detectors are available. Similarly to the SEM, SE, BSE and EDS detectors are present but some FIB models also include a retractable STEM detector, which allows verifying if electron transparency has been reached when thinning lamellae. The STEM detector may also provide information about the sample with different imaging modes, if capable - bright-field (BF), dark-field (DF) and high-angle annular dark-field (HAADF). BF mode generates an image using the unscattered beam that is transmitted directly through the sample. The images appear with a bright background and the regions where electrons are scattered or absorbed appear darker. DF mode works in the opposite way - the image is generated using the scattered electrons rather than the direct beam. This results in a dark background, with the imaged structures appearing brighter according to how strongly they scattered the beam. The HAADF mode uses an annular detector to detect electrons scattered at very high angles. The scattering intensity is proportional to the atomic number of the atoms that caused the scattering, which makes elements with high atomic numbers appear bright in DF and HAADF images.[53] This may allow the identification of elemental distributions in the sample. All imaging modes described provide valuable and usually complementary information.

A detector for secondary ions - ions ejected from the sample due to the incident ion beam - may be present. In this case imaging may be performed with the ion beam, originating images which are less prone to charging artifacts and with greater surface detail, due to the reduced sample depth from which the ions originate.[14] However, the danger of damaging the sample is always present.

To sputter the sample, high enough current values are necessary. If the current is lower, imaging may be performed using the ion beam with minimal sample damage. However, some damage is inevitable and as such focusing the beam should be performed on a region of the sample that can be sacrificed. The beam can then be moved to the region of interest for imaging, which should be performed with reduced dwelling times.

When milling the sample its surface must be protected from possible beam damage. To do this the region of interest is protected by a layer of some material, Pt for instance, placed by electron beam induced deposition (EBID). An additional layer may be deposited on top of this by ion beam induced deposition. Regardless of the beam used, the principle is the same. A precursor containing the material to be deposited

is introduced in the sample chamber by the gas injection system (GIS) of the FIB (Figure 3.8). This material is usually kept in solid or liquid state and is heated to the gas phase for the deposition. The electron or ion beam scans the region of interest in the pattern defined and decomposes the gas into its constituents, with the non-volatile ones being deposited and the volatile ones being extracted by the vacuum system.

With the protective Pt deposited, a region adjacent to it can be milled with the desired dimensions using the ion beam. The beam rasters the region defined, sputtering material and exposing the cross-section (Figure 3.9). For lamellae preparation, an additional cross-section must be milled on the opposite side of the deposited surface protector (Figure 3.10). A thin region is obtained, which must be moved to a TEM grid for thinning until electron transparency is reached. The micromanipulator's tip is connected to the lamella using EBID and the bottom of the lamella is milled, separating it from the sample. It can then be moved to the TEM grid where it is attached by EBID again. The lamella then undergoes final thinning with the STEM detector used to check whether electron transparency has been reached. A final cleaning with the ion beam, using reduced accelerating voltages, is performed to remove possible amorphizations induced.

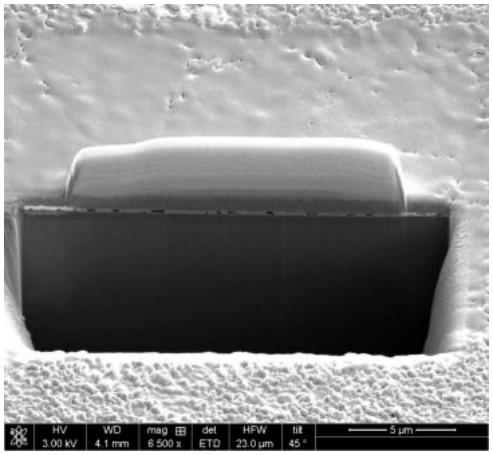

Figure 3.9: Preparation step of a lamella, showing the first cross-section milled.

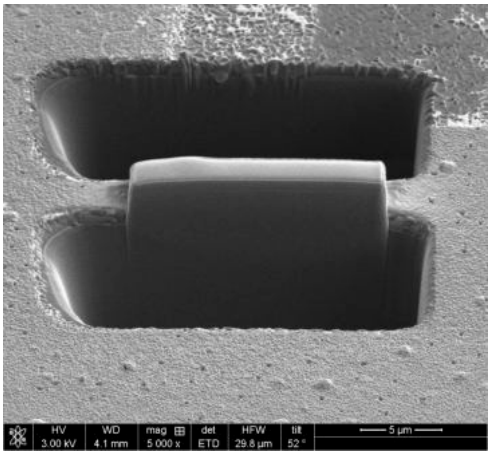

Figure 3.10: Preparation step of a lamella showing the two cross-sections milled - one in front of the protected surface region and the other behind it.

3.2.5 Equipment used

The SEM used was a FEI Quanta 650 FEG (Figure 3.11). It has capability for high vacuum, LVSEM and environmental SEM, a mode which uses much higher pressure than LVSEM. The electron gun is a Schottky field-emission gun allowing resolutions down to 1 nm and the accelerating voltage ranges in 1-30 kV. It also includes a Peltier cooling stage, SE detectors for the different vaccum modes - an Everhart-Thornley for high vacuum mode, a Large Field Detector (LFD) for LVSEM and a gaseous SED (GSED) for environmental SEM - and BSE and EDS detectors. The EDS detector is an Oxford Instruments INCA x-act, model 51-ADD0008, sensor 51-1385-022. The microscope also includes multi-sample and individual sample holders and the stage is capable of moving in the xyz space, rotating and tilting.[54]

The microscope was operated in high vacuum whenever possible, except when the samples under

study displayed an elevated degree of charging. In these instances LVSEM was used.

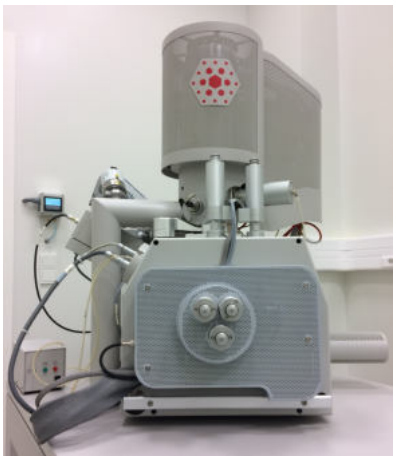

Figure 3.11: The FEI Quanta 650 FEG of the INL - International Iberian Nanotechnology Laboratory.

The FIB used was a FEI Helios G2 NanoLab 450S (Figure 3.12). It is a Dual Beam FIB-SEM. The SEM uses a field-emission gun capable of resolutions of 0.8 nm at an accelerating voltage of 15 kV, and having an accelerating voltage range of 1-30 kV. The FIB uses Ga for the ion beam, has an accelerating voltage range of 1-30 kV and is capable of resolutions of 4 nm at 30 kV. The system possesses SE detectors for both beams and a BSE detector for the electron beam. Additionally, an EDS detector from Oxford Instruments INCA x-act, model 51-ADD0052, sensor 51-1385-022 is available, as well as a STEM detector with a resolution of 0.8 nm at 30 kV. The microscope possesses a sample stage capable of moving in the xyz space, rotating and tilting, and a "Flip stage" where TEM grids are stored. It also possesses a loadlock chamber, which allows loading and unloading of samples without the need of venting the whole sample chamber, and as such reducing the contamination level. It possesses 4 GIS, giving it the ability of depositing Pt and W or performing enhanced etching using iodine or selective carbon etching. The micromanipulator is an Omniprobe 200. Finally, the system possesses a charge neutraliser to compensate possible charging due to the Ga ions. [55]

The material deposited to protect the surface of the samples studied was Pt.

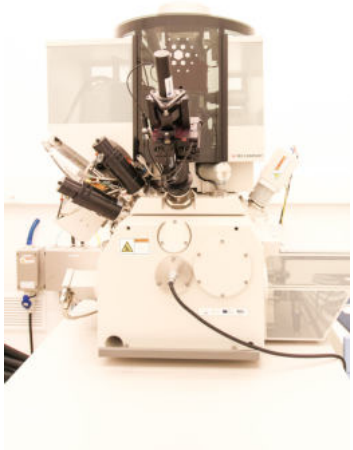

Figure 3.12: The FEI Helios G2 NanoLab 450S of the INL - International Iberian Nanotechnology Laboratory.

4 Results and Discussion

4.1 Experimental results

In this section the experimental results of the studied systems are presented. Three systems were studied: LNO film on Si substrate, LNO film on SiPt substrate and CFO-LNO bilayer film on SiPT substrate.

The deposition conditions of the studied samples are presented in Table 1 (LNO and CFO films) and in Table 2 (CFO-LNO films). T_{dep} is the deposition temperature, E is the laser's energy, f the frequency of the pulse and t_{dep} is the deposition time. T_{an} is the annealing temperature and t_{an} the annealing time, d_{target} is the target-substrate distance and P_{dep} is the deposition pressure or background gas pressure.

Sample	Substrate	T_{dep}(°C)	E(mJ)	f(Hz)	t_{dep}(min)	T_{an} (°C)	t_{an}(min)	d_{target}(cm)	P_{dep}(mbar)
SiLNO 6A	Si	RT	350	6	20	650	120	3	1
SiLNO 5B	Si	650	350	6	20	–	–	3	0
SiLNO 9A	Si	RT	350	6	20	–	–	3	0.1
SiLNO 10A/B	Si	RT	350	6	20	–/650	–/120	3	0.01
SiLNO 11A/B	Si	RT	350	6	20	–/650	–/120	7	0.01
SiLNO 12A/B	Si	RT	350	6	20	–/650	–/120	2	0.1
SiPtLNO 4B	SiPt	650	350	6	60	–	–	3	1
SiPtCFO 2	SiPt	650	350	10	60	–	–	3.5	0.1

Table 1: Deposition conditions of the LNO and CFO films studied.

Sample	Substrate	Target	T_{dep}(°C)	E(mJ)	f(Hz)	t_{dep}(min)	d_{target}(cm)	P_{dep}(mbar)
SiPtCFOLNO 2	SiPt	CFO	650	350	10	45	5	0.1
		LNO			6	30	3	1
SiPtCFOLNO 6	SiPt	CFO	650	350	10	60	5	0.1
		LNO			6	45	3	1
SiPtCFOLNO 8	SiPt	CFO	650	350	10	60	5	0.1
		LNO			6	75	3	1
SiPtCFOLNO 9	repetition of the previous sample							
SiPtCFOLNO 10	SiPt	CFO	650	350	10	75	5	0.1
		LNO			6	30	3	1
SiPtCFOLNO 15	SiPt	CFO	650	350	10	20	5	0.1
		LNO			6	10	3	1
SiPtCFOLNO 16	SiPt	CFO	650	350	10	30	5	0.1
		LNO			6	10	3	1
SiPtCFOLNO 17	SiPt	CFO	650	350	10	75	5	0.1
		LNO			6	30	3	1
SiPtCFOLNO 19	SiPt	CFO	650	350	10	60	5	0.1
		LNO			6	60	3	1
SiPtCFOLNO 22	SiPt	CFO	650	350	10	60	3.5	0.1
		LNO			6	60	3.1	1

Table 2: Deposition conditions of the CFO-LNO films studied.

4.1.1 LNO film on Si substrate

Sample: SiLNO 6A

Substrate	T(°C)	E(mJ)	f(Hz)	d_{target}(cm)	t_{dep}(min)	P_{dep}(mbar)
Si	RT	350	6	3	20	1

Table 3: Deposition conditions of sample SiLNO 6A.

This sample was deposited at room temperature (RT) and subsequently annealed at 650 °C for 2h. It shows the effect that a low deposition temperature allied with a high background gas pressure has on the film's microstructure.

Atomic %		
Nb	O	Ratio (approx.)
7.62	36.4	0.21
25.55	72.82	0.35
10.09	41.92	0.24
4.61	18.83	0.24
24.57	73.08	0.34
25.65	70.87	0.36
20.01	79.27	0.25
45.67	48.34	0.94

Table 4: Results of SEM-EDS analysis.

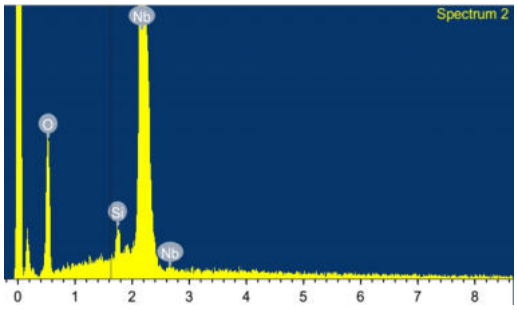

Figure 4.1: SEM-EDS spectrum of the sample.

SEM-EDS analysis confirms that all $LiNbO_3$ elements of interest are present (Figure 4.1). Table 4 shows the results of SEM-EDS for different regions in the sample. According to the chemical formula for LNO, $LiNbO_3$, the intended Nb/O ratio is $1/3$. It is observed that the ratio is achieved in some regions (denser regions shown in Figure 4.8 and Figure 4.7) and is close in others. The estimated uncertainty for the presented values is around 10%.

The sample's surface shows regions of different density as well as voids (Figure 4.2 and Figure 4.3).

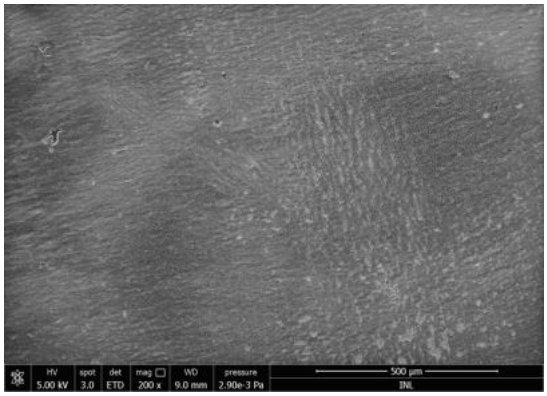

Figure 4.2: Low magnification SEM image showing the surface of the sample.

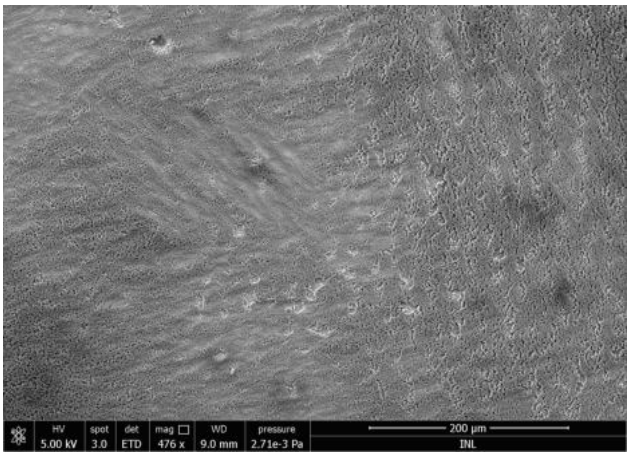

Figure 4.3: Higher magnification SEM image of Figure 4.2.

Figure 4.4 shows a region where the density is reasonably uniform, contrasting with other regions comprising both high and low-density areas, as shown in Figure 4.5.

Figure 4.4: Higher magnification image but on another region.

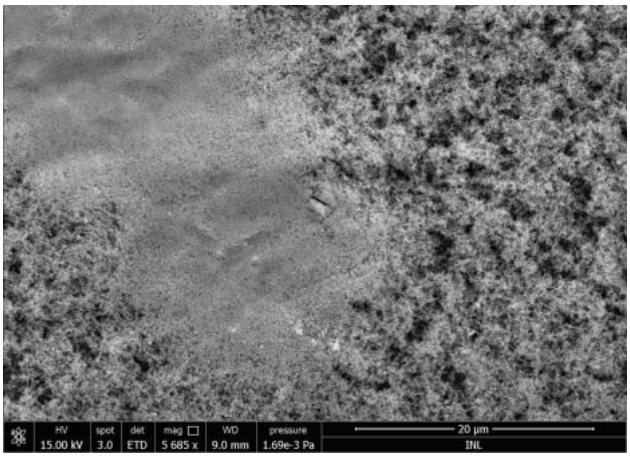

Figure 4.5: SEM image showing a highly dense region amidst the less dense surroundings.

Figure 4.6 shows a close-up of a low-density region, revealing a mesh-like structure originating from individual grains accumulating in different directions but with large distances between clusters (Figure 4.7).

The high pressure of 1 mbar used during deposition tends to brake the progression of the ablation plume, thermalizing its species. As such, there is a tendency for the atoms to accumulate randomly at the substrate depending on its temperature, creating the low density regions observed.

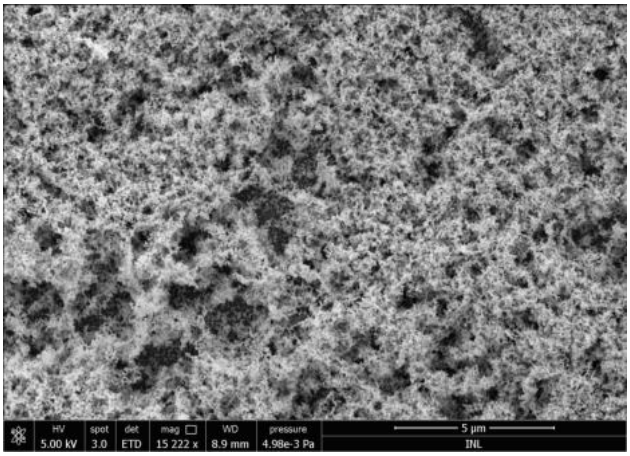

Figure 4.6: High magnification SEM image showing a low-density region.

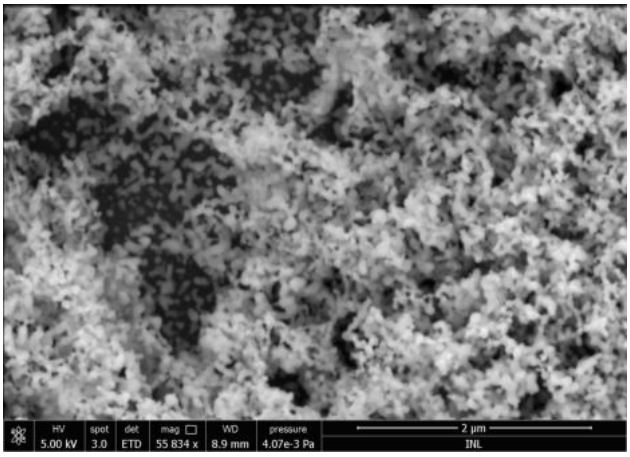

Figure 4.7: Higher magnification SEM image of Figure 4.6 revealing individual grains.

Closer inspection of a denser region (Figure 4.8) reveals the much closer packing of the grains. Their dimensions were manually measured using the image analysis software ImageJ and a histogram was generated (Figure 4.9). A logarithmic normal distribution (lognormal) was adjusted to it, yielding the average grains size x_0 and its respective standard deviation σ (indicated in Figure 4.9), the latter of which providing a notion of the extent to which the grain size varies in the sample. This procedure was performed for every sample in this work.

The average grain size for the present sample has a value of $\approx$ 78.6 with a distribution width of $\approx$ 29.5 nm.

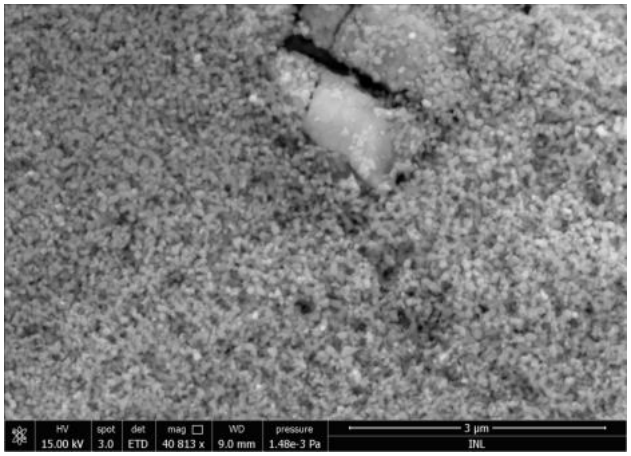

Figure 4.8: High magnification SEM image of a dense region.

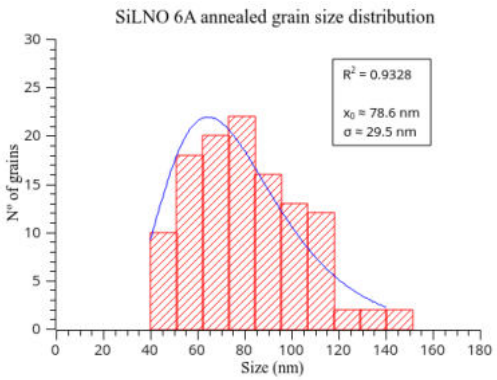

Figure 4.9: Grain size distribution of the sample with mean average size and respective standard deviation indicated.

Cross-section imaging of the sample reveals a voided bulk structure, as shown in Figure 4.10.

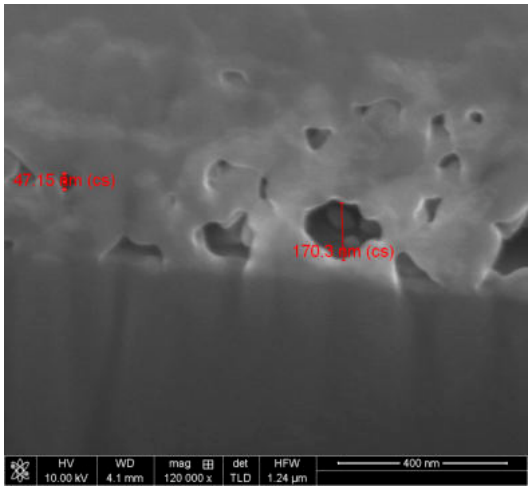

Figure 4.10: High magnification SEM image of the film's cross-section, showing the formed voids and some representative dimensions.

The mesh-like structure and the small, individual grains observed suggest a zone 1 structure of Thornton's diagram.

Sample: SiLNO 5B

Substrate	T(°C)	E(mJ)	f(Hz)	d_{target}(cm)	t_{dep}(min)	P_{dep}(mbar)
Si	650	350	6	3	20	0

Table 5: Deposition conditions of sample SiLNO 5B.

This sample shows the impact on the film microstructure and stoichiometry of performing a deposition without a background gas.

Atomic %		
Nb	O	Ratio (approx.)
0.85	10.55	0.08
0.74	10.36	0.07

Table 6: Results of SEM-EDS analysis.

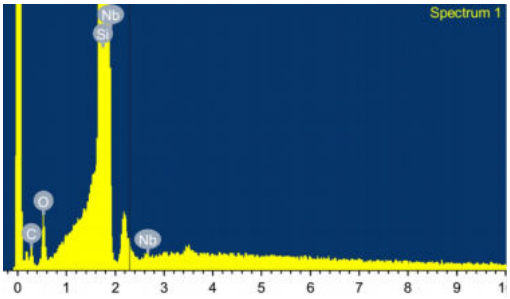

Figure 4.11: SEM-EDS spectrum of the sample's surface.

SEM-EDS analysis confirms that all $LiNbO_3$ elements of interest were deposited (Figure 4.11). The presence of carbon is not surprising since it is very common in the atmosphere and simply by manipulating the sample it may adhere to its surface. It may also come from the copper tape used to glue the samples to their support. Table 6 shows the results of SEM-EDS for different regions in the sample. Only two of the regions analysed confirmed the presence of Nb. However, despite it not appearing in the analysis of the other regions, an asymmetry of the Pt peak was observed, suggestive of the presence of Nb given the proximity in energy of the Nb and Pt peaks. Despite this, in the regions where analysis was possible, the Nb/O ratio is far from the intended 1/3 value. Results from more regions would be necessary to draw a more definitive conclusion, but it should be noted that this sample was deposited without a reactive O_2 atmosphere, so this observation is not surprising.

Figure 4.12 reveals the individual grains that make up the surface. Regions of smaller grain size are visible in the bottom and top-left of the image as indicated by the white arrows.

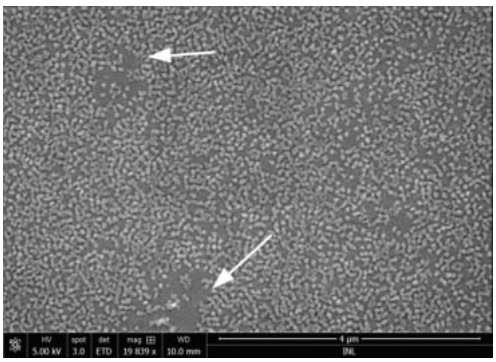

Figure 4.12: High magnification SEM image of the surface of the sample. The white arrows indicate regions of smaller grain size.

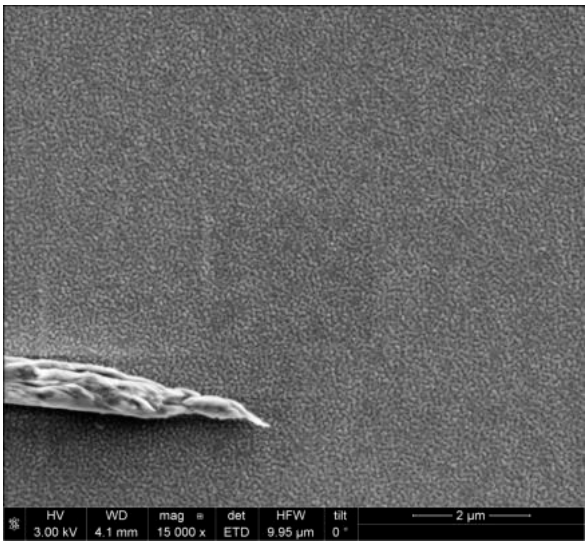

Figure 4.13: High magnification SEM image of another region, displaying the close-packing of the grains.

Figure 4.13 shows another region where the grains are closely-packed together. The elongated structure observed is most likely some contamination that was on the film's surface - perhaps a piece of copper tape used to hold the sample to the sample holder.

Figure 4.14 shows a high magnification SEM image of a region with both large and small grains. The large grains appear faceted and have an average size of $\approx$ 76.4 with a distribution width of $\approx$ 13.4 nm (Figure 4.15). The smaller grains appear to have coalesced to some extent. Their average size is $\approx$ 51.8 with a distribution width of $\approx$ 24.2 nm (Figure 4.16). This suggests a zone 2 structure of Thornton's diagram.

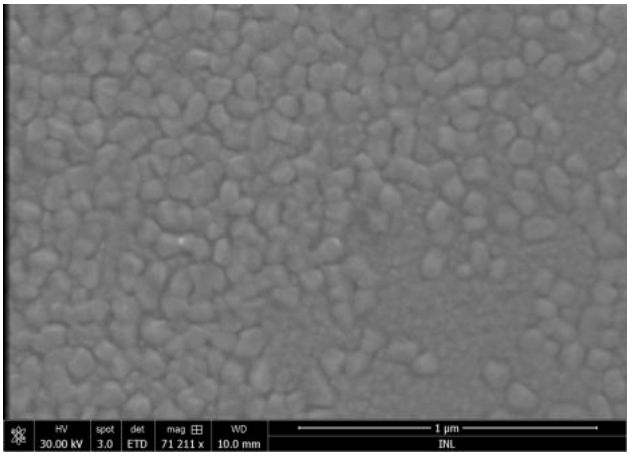

Figure 4.14: High magnification SEM image of a region with both larger and smaller grains.

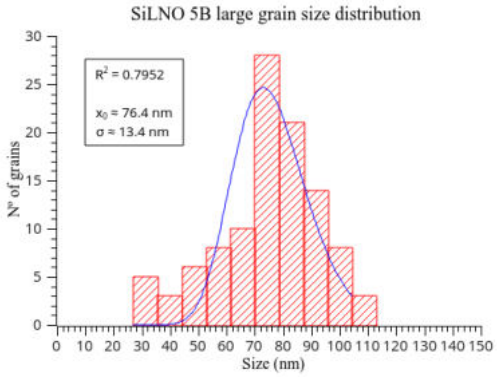

Figure 4.15: Size distribution of the larger grains.

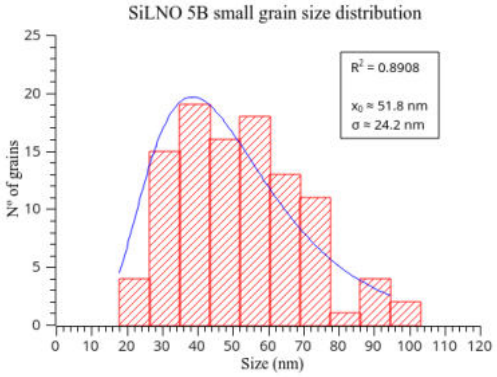

Figure 4.16: Size distribution of the smaller grains.

Figure 4.17 reveals the sample's cross-section with the film thickness indicated.

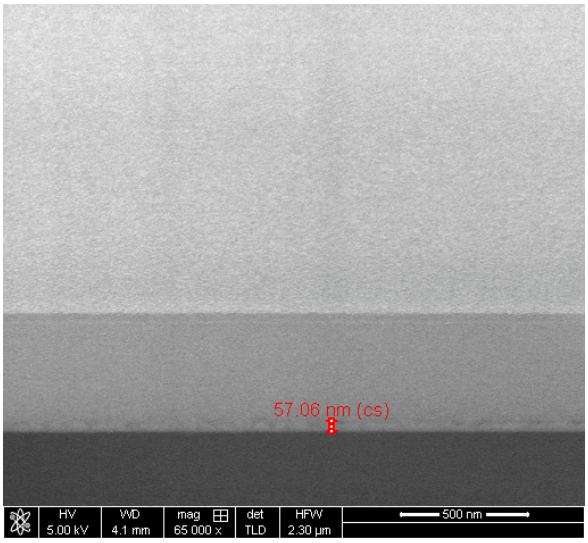

Figure 4.17: High magnification FIB-SEM image of the cross-section with the film's thickness indicated.

Sample: SiLNO 9A

Substrate	T(°C)	E(mJ)	f(Hz)	d_{target}(cm)	t_{dep}(min)	P_{dep}(mbar)
Si	RT	350	6	3	20	0.1

Table 7: Deposition conditions of sample SiLNO 5B.

Comparison with the previous sample reveals the impact on the film's microstructure of introducing a background gas during the deposition. In particular, it provides information on the pressure value necessary, for the same target-substrate distance, to avoid a film with voids.

Atomic %		
Nb	O	Ratio (approx.)
1.02	13.75	0.07

Table 8: Results of SEM-EDS analysis.

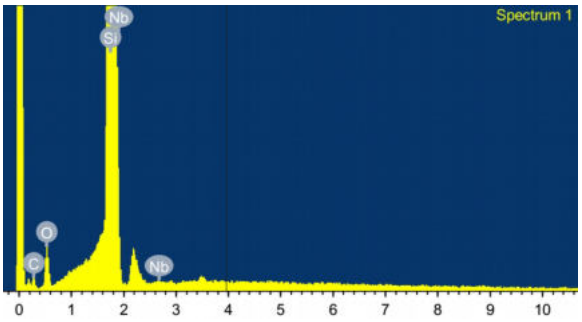

Figure 4.18: SEM-EDS spectrum of the sample's surface.

SEM-EDS analysis confirms the presence of the $LiNbO_3$ elements of interest (Figure 4.18) but the Nb/O ratio seems far from the intended value (Table 8). However, more regions analysed would be needed to draw a more definitive conclusion.

The sample's surface is cracked but appears smooth overall (Figure 4.19). On a region where the film was damaged (Figure 4.20), its border exposes a columnar/crystallite structure separated by voids.

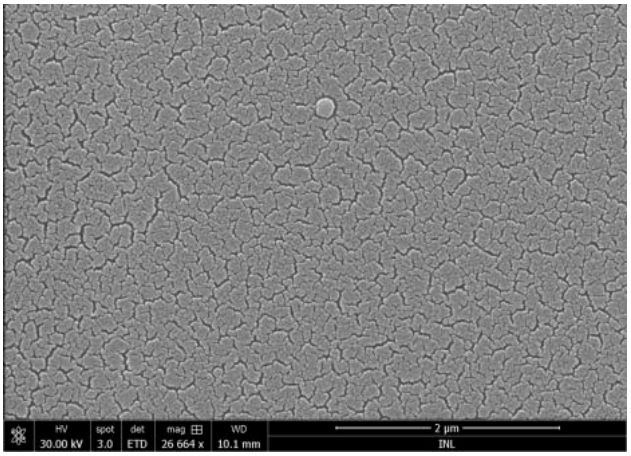

Figure 4.19: High magnification SEM image showing the surface of the sample.

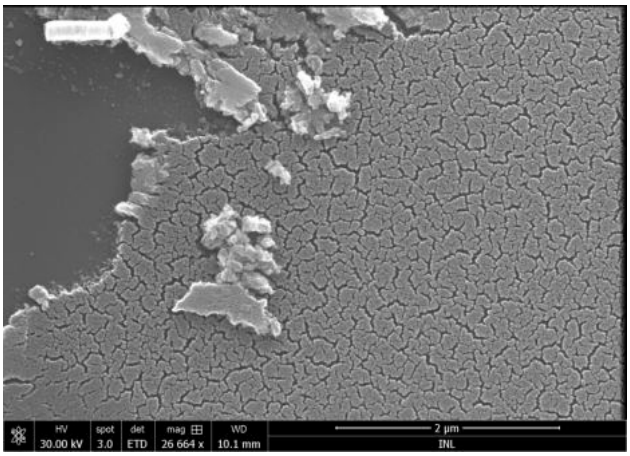

Figure 4.20: High magnification SEM image showing a region where the film was damaged, exposing the Si substrate (dark region on the left).

Close inspection of the surface (Figure 4.21) reveals the individual grains that constitute the clusters, allowing the determination of their size distribution (Figure 4.22). The average grain dimension is ≈ 22.9 with a distribution width of ≈ 9.1 nm.

The cracked structure is typical of a zone 1 of Thornton's diagram, eventually a zone T (compare with Figure 2.16, Figure 2.17 and Figure 2.18). Given that the sample was deposited at room temperature the zone 1 structure is not surprising, as not enough energy was available to promote surface diffusion of the film's atoms on the substrate's surface.

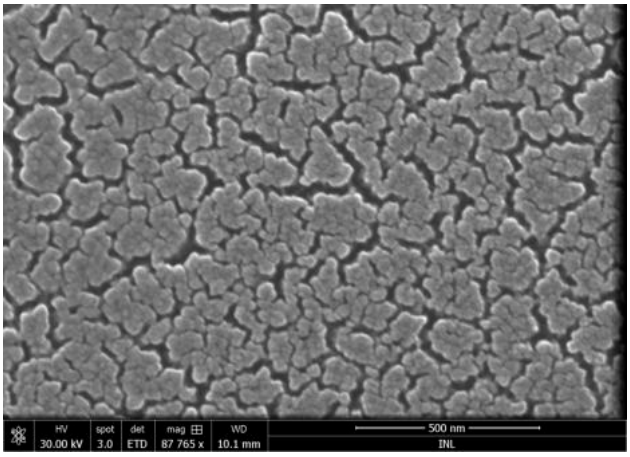

Figure 4.21: High magnification SEM image of the surface.

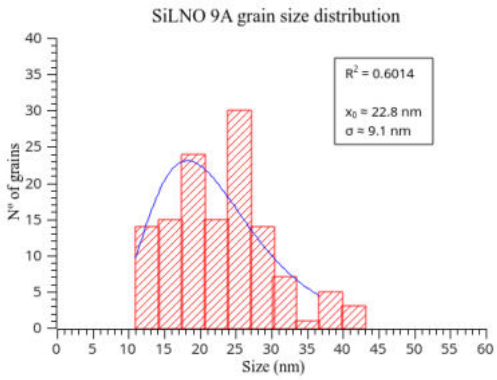

Figure 4.22: Size distribution of the grains.

Sample: SiLNO 10A

Substrate	T(°C)	E(mJ)	f(Hz)	d_{target}(cm)	t_{dep}(min)	P_{dep}(mbar)
Si	RT	350	6	3	20	0.01

Table 9: Deposition conditions of sample SiLNO 10A.

This sample shows the effect on film microstructure of using a lower pressure compared with the previous sample, for the same target-substrate distance. However, the effect of using a much lower deposition temperature will become clear when compared with the next sample.

Atomic %		
Nb	O	Ratio (approx.)
1.59	17.81	0.09
4.09	27.71	0.15
3.97	27.49	0.14
4.45	26.59	0.17
4.15	25.71	0.16
4.39	31.73	0.14
4.12	28.86	0.14
3.71	27.82	0.13
3.71	28.56	0.13
4.15	29.51	0.14
3.75	28.29	0.13
4.15	31.37	0.13
3.82	27.23	0.14
3.94	27.28	0.14
4.05	26.59	0.15
3.64	27.96	0.13
4.10	26.73	0.15
4.40	30.67	0.14
3.57	25.86	0.14

Table 10: Results of SEM-EDS analysis.

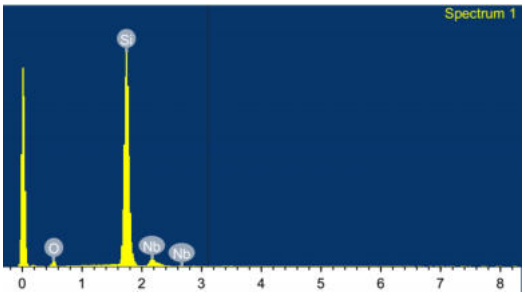

Figure 4.23: SEM-EDS spectrum of the sample's surface.

SEM-EDS analysis confirms the presence of all intended elements (Figure 4.23). However, the Nb/O ratio is not as intended (Table 10), tending to be lower and indicating an excess of oxygen that comes from the oxidation of the Si substrate surface.

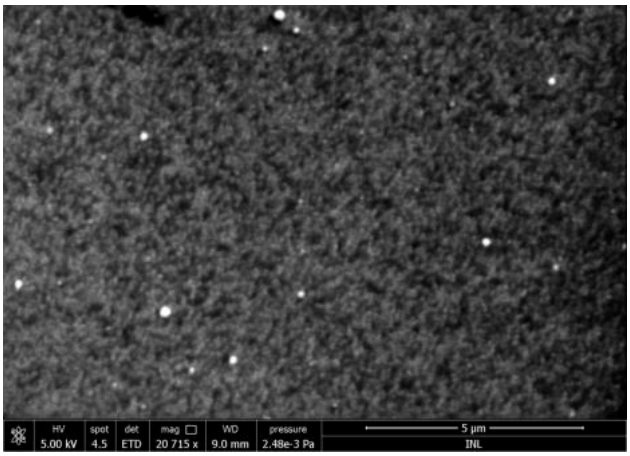

Figure 4.24: Surface of the sample.

The sample's surface seems uneven and porous (Figure 4.24). The white balls observed are probably larger LNO particulates that were deposited.

Higher magnification imaging reveals small, individual grains (Figure 4.25) with an average size of ≈ 67.8 and distribution width of ≈ 21.8 nm (Figure 4.26).

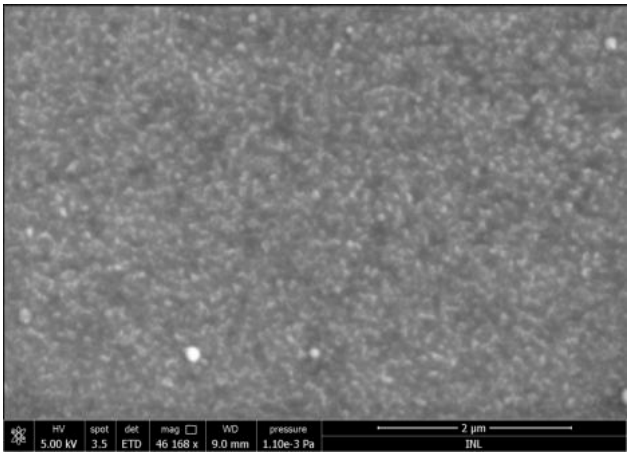

Figure 4.25: SEM image of the surface taken at higher magnification and smaller spot size.

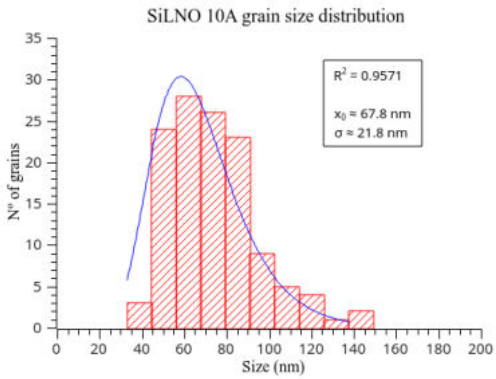

Figure 4.26: Grain size distribution of the sample.

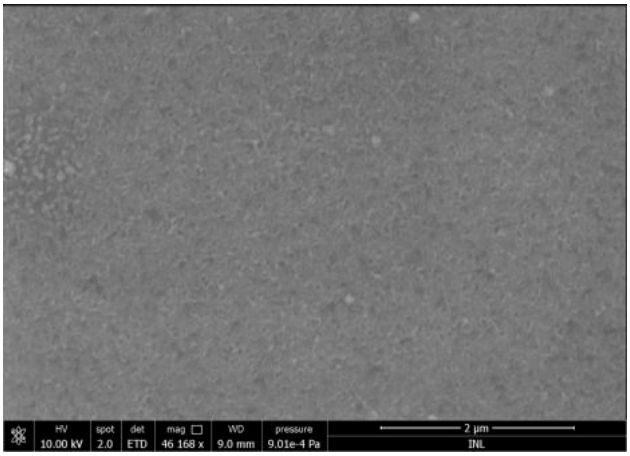

Figure 4.27: SEM image taken at 10 kV showing the surface of the sample.

Figure 4.27 shows an image of the surface taken at a higher accelerating voltage. The non-smooth surface observed suggests a porous inner structure.

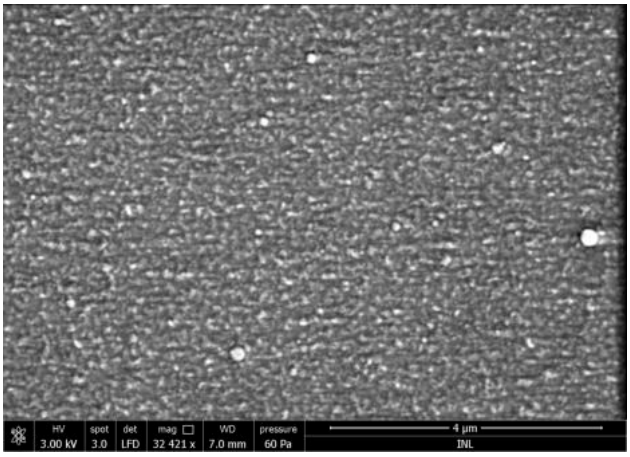

Figure 4.28: High magnification SEM image of the surface taken in low vacuum mode and low kV.

The surface appears rough but otherwise continuous and homogeneous, constituted by individual grains that coalesced to some extent and originated an uneven surface (Figure 4.28). Larger particulates (large, white spheres) are also observed.

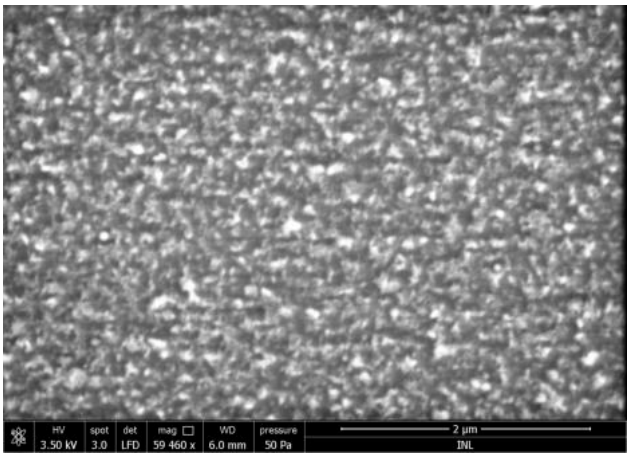

Figure 4.29: Higher magnification SEM image of the surface in low vacuum mode.

Figure 4.29 shows that the roughness seems due to the coalescence of the grains, originating regions where the film's material agglomerated and gave rise to peaks in the surface. This morphology seems characteristic of a zone 1 of Thornton's diagram or perhaps a zone T. Once again, as the sample was deposited at room temperature, this is not surprising.

Sample: SiLNO 10B

This sample is an annealed version of the previous one - its deposition conditions are the same but was submitted to an annealing procedure at 650 °C for 2h after the deposition. It shows the result of performing an annealing, post-deposition, with the original value of deposition temperature, providing insight on the effect that using it during the deposition, for this value of pressure, may have on film microstructure.

Atomic %		
Nb	O	Ratio (approx.)
3.79	28.72	0.13
3.81	28.20	0.14
3.60	27.57	0.13
3.63	27.45	0.13
3.86	28.19	0.14
4.08	28.36	0.14
3.80	28.01	0.14
3.88	28.27	0.14
3.90	28.96	0.13
3.94	28.13	0.14
3.92	28.14	0.14
3.54	29.53	0.12
3.96	29.86	0.13
3.65	28.17	0.13
4.18	33.17	0.14

Table 11: Results of SEM-EDS analysis.

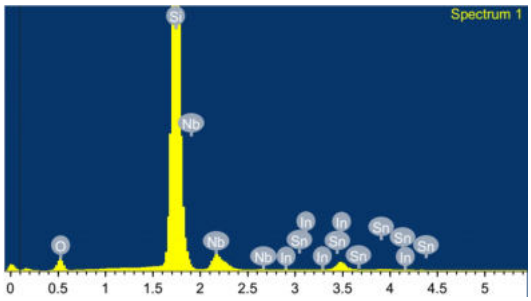

Figure 4.30: SEM-EDS spectrum of the surface.

SEM-EDS analysis accuses the presence of contaminations (Figure 4.30). Given that the only difference between the present sample and the previous one is the annealing procedure, they must come from the annealing oven. The Nb/O ratios (Table 11) remain in accordance with the previous sample.

Figure 4.31 reveals a dense film with large, smooth grains, suggestive of the occurrence of recrystallization. This structure is typical of zone 3 of Thornton's diagram. However smaller grains are also present, as well as small voids (dark dots) at the boundaries between grains. The bright, round structures are larger particulates that were deposited.

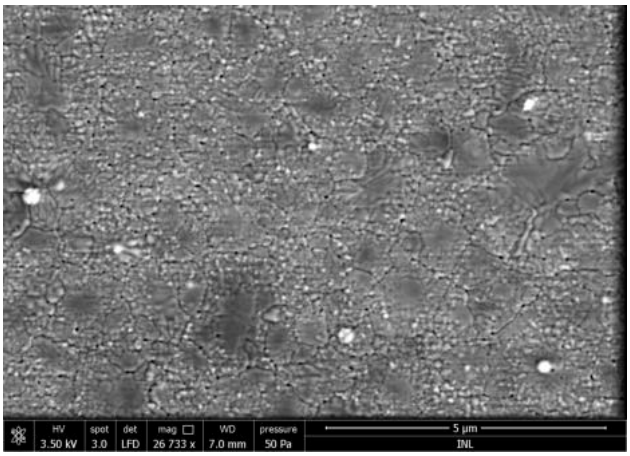

Figure 4.31: SEM image showing the surface of the $LiNbO_3$ film after annealing, imaged in low vacuum mode.

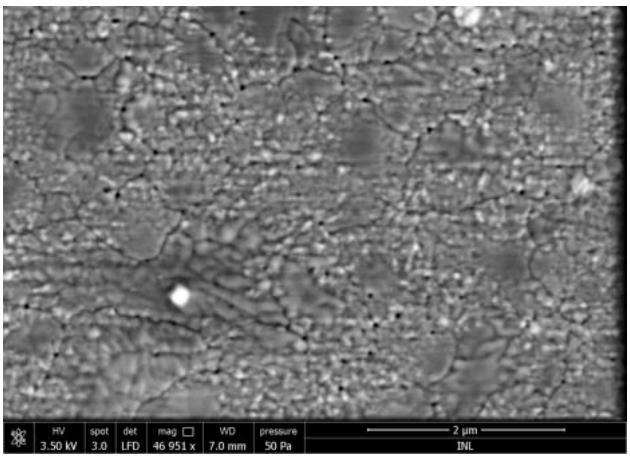

Figure 4.32: High magnification SEM image of the surface.

Figure 4.32 facilitates the visualization of the voids (dark areas) as well as of the smaller grains, which appear to have coalesced to form the larger ones. The void average size is $\approx$ 38.0 with a distribution width of $\approx$ 13.0 nm (Figure 4.33) while the small grain average size is $\approx$ 67.0 with a distribution width of $\approx$ 20.4 nm (Figure 4.34).

The presence of the small grains with coalescence is evident, along with the small voids at the boundaries between grains, suggesting a zone 2 structure of Thornton's diagram in transition to zone 3.

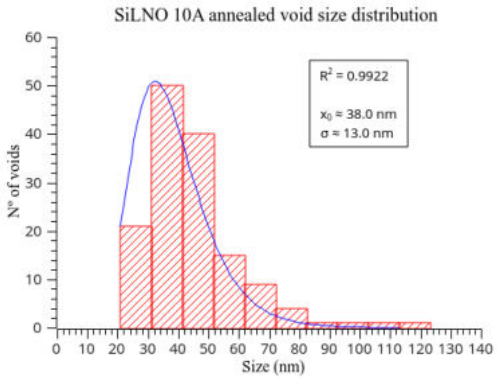

Figure 4.33: Size distribution of the voids.

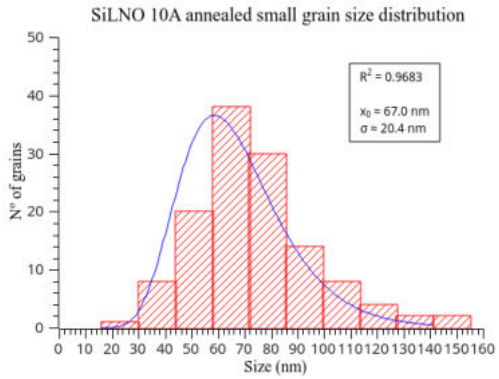

Figure 4.34: Size distribution of the small grains.

Figure 4.35 shows another region where a greater number of larger grains are visible, allowing an estimation of their size distribution (Figure 4.36). The average grain size is $\approx$ 438 with a distribution width of $\approx$ 130 nm.

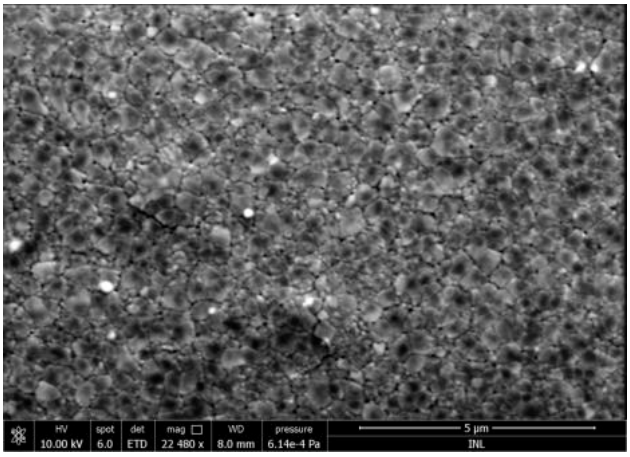

Figure 4.35: SEM image image of another region taken in high vacuum mode.

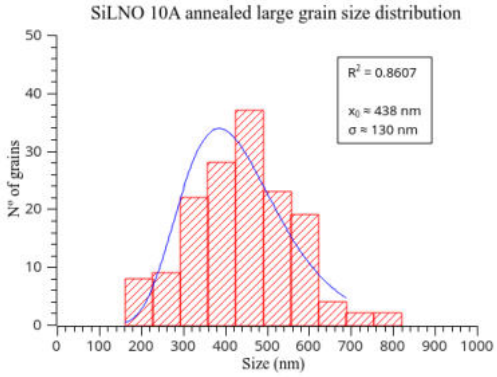

Figure 4.36: Size distribution of the large grains.

Imaging of the surface at an higher accelerating voltage (Figure 4.37) reveals the presence of porosity at the boundaries between the grains, which indicates that they extend at least some distance below the film's surface.

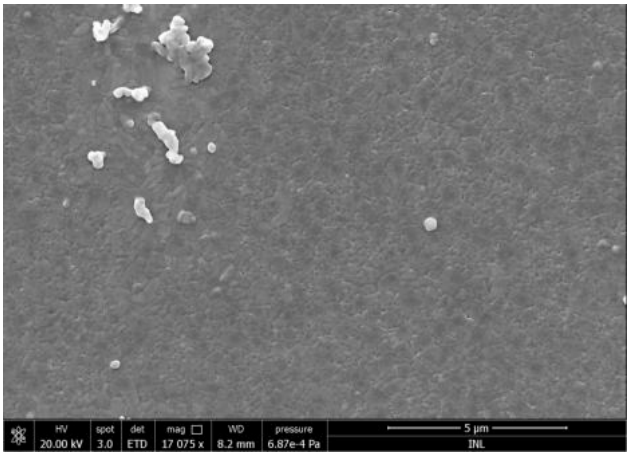

Figure 4.37: SEM image of the surface taken with a higher accelerating voltage.

Samples: SiLNO 11A/B

Substrate	T(°C)	E(mJ)	f(Hz)	d_{target}(cm)	t_{dep}(min)	P_{dep}(mbar)
Si	RT	350	6	7	20	0.01

Table 12: Deposition conditions of samples SiLNO 11A/B.

Both samples were deposited at room temperature. The B version was subsequently annealed at 650 °C for 2h. These samples show the effect that a large increase in target-substrate distance has on film microstructure, for the same deposition/annealing conditions as in the previous sample.

Atomic %		
Nb	O	Ratio (approx.)
2.57	19.59	0.13
3.40	26.78	0.13
0.76	6.91	0.11
0.75	8.57	0.09
0.88	7.70	0.11
0.81	7.50	0.11
2.25	15.75	0.14
4.20	25.27	0.17
0.91	6.4	0.14
2.34	16.90	0.14

Table 13: Results of SEM-EDS analysis for the non-annealed sample.

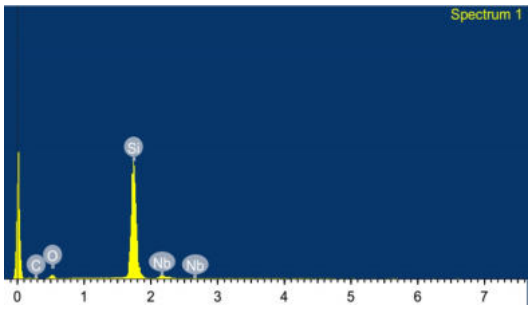

Figure 4.38: SEM-EDS spectrum of the non-annealed sample.

Atomic %		
Nb	O	Ratio (approx.)
0.22	4.53	0.05
0.36	4.67	0.08
0.37	5.93	0.06

Table 14: Results of SEM-EDS analysis for the annealed sample.

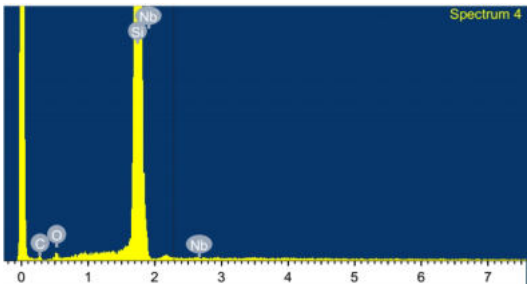

Figure 4.39: SEM-EDS spectrum of the annealed sample.

SEM-EDS analysis confirms the presence of the elements of interest in both samples (Figure 4.38 and Figure 4.39). Their stoichiometry, however, is not as intended (Table 13 and Table 14), with the annealed sample in particular showing smaller Nb/O ratios. However, more regions analysed would be necessary to confirm the effect since the percentage values are small.

The sample has ring-like structures spread throughout its surface (Figure 4.40), probably impact craters formed by bulk-like (droplets) particulates of $LiNbO_3$ that did not stick to the film. Between these craters, small, isolated droplets of material are visible, with an average size of $\approx$ 104 and distribution width of $\approx$ 98 nm (Figure 4.41). Apart from these droplets, no type of structure is identifiable between the craters, suggesting that the film's material was deposited through the seen droplets only or that it may be very smooth (most likely), thus making the observation of any other structure difficult.

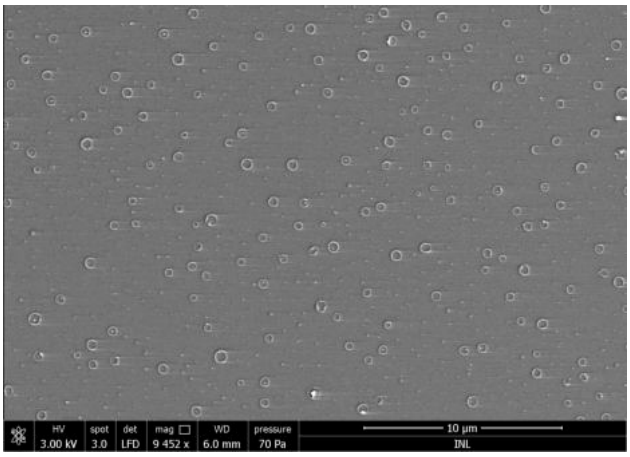

Figure 4.40: SEM image showing the surface of the non-annealed sample.

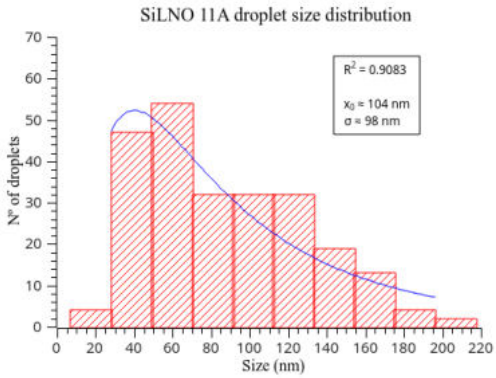

Figure 4.41: Droplet's size distribution.

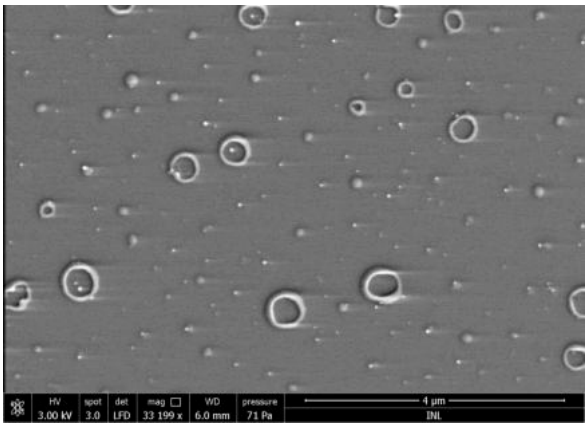

Figure 4.42: Higher magnification SEM image of the region imaged in Figure 4.40.

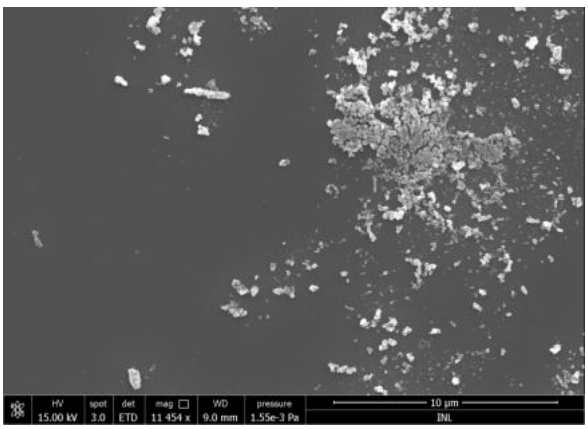

Figure 4.43: SEM image showing another region of the non-annealed sample.

Figure 4.43 shows another region of the sample where some material was clearly deposited and agglomerated to some extent, but no type of structure is readily identifiable. It is in the limit of the thinner part of the films corresponding to the extreme of the plume. However, given the morphology of the largest cluster of material (top-right), a zone 1 or T structure of Thornton's diagram seems to have been favoured.

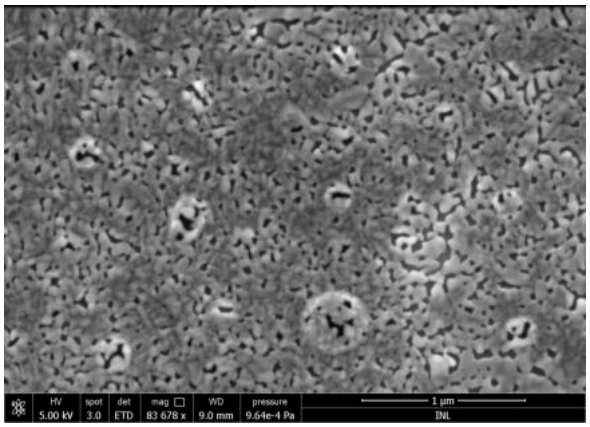

Figure 4.44: SEM image showing the surface of the annealed sample.

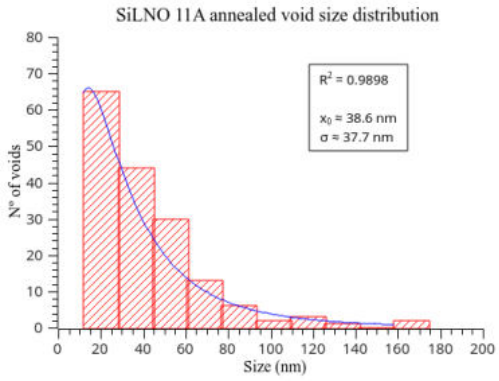

Figure 4.45: Size distribution of the voids in the annealed sample.

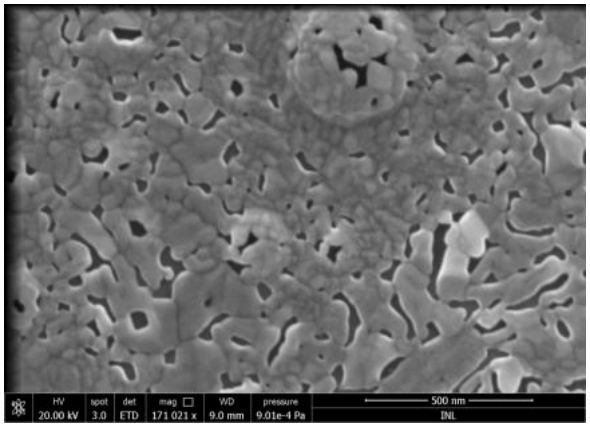

Figure 4.46: Higher magnification SEM image of the region shown in Figure 4.44.

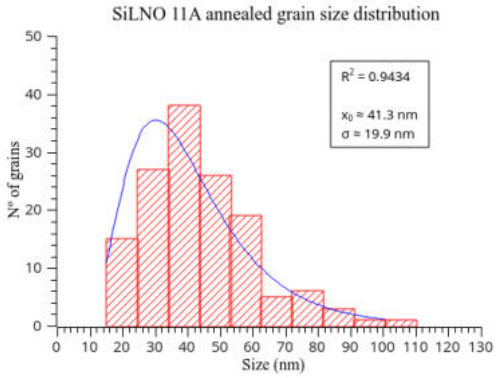

Figure 4.47: Size distribution of the grains.

Figure 4.44 shows the surface of the annealed sample, revealing a grained, porous structure in which the grains seem to have coalesced together, showing signs of melting. Nevertheless, the average void size is $\approx$ 38.6 with a distribution width of $\approx$ 37.7 nm (Figure 4.45) showing small pores. The circular bright spots correspond to the craters and white particulates seen in the non-annealed sample. Of particular notice is the observation of material between the craters, contrary to the non-annealed sample. This suggests that the as-deposited (non-annealed) films are dense, with a smooth surface.

The coalesced grains (Figure 4.46) have an average size of $\approx$ 41.3 and a distribution width of $\approx$ 19.9 nm (Figure 4.47). The surface is somewhat reminiscent of a recrystallized film, suggesting some level of recrystallization took place. Classifying this sample in terms of a Thornton's diagram zone is difficult - on one hand, the porous aspect is characteristic of zone 1 but on the other hand the recrystallized aspect is typical of zone 3. As such, the film has a zone 1 structure and is very sparse over the substrate's surface, but the annealing process provided enough energy for some coalescence/recrystallization to take place.

Samples: SiLNO 12A/B

Substrate	T(°C)	E(mJ)	f(Hz)	d_{target}(cm)	t_{dep}(min)	P_{dep}(mbar)
Si	RT	350	6	2	20	0.1

Table 15: Deposition conditions of samples SiLNO 12A/B.

Similarly to the previous sample, both A and B versions were deposited at room temperature but the B version was subsequently annealed at 650 °C for 2h. This sample has the same deposition conditions as sample SiLNO 9A (T = RT, d_{target} = 3 cm, t_{dep} = 20 min, P_{dep} = 0.1 mbar) except for the target-substrate distance, which is 1 cm smaller in the present sample, illustrating the impact that a reduction by such a value has on film microstructure.

Atomic %		
Nb	O	Ratio (approx.)
1.93	17.12	0.11
1.86	6.93	0.27
2.43	17.57	0.14

Table 16: Results of SEM-EDS analysis for the non-annealed sample.

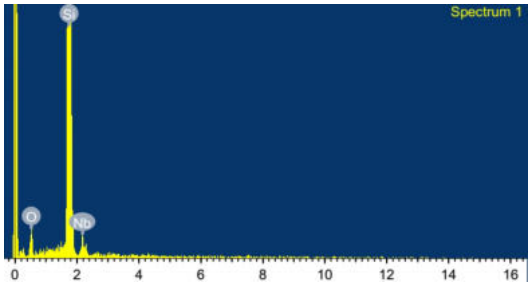

Figure 4.48: SEM-EDS spectrum of the non-annealed sample.

Atomic %		
Nb	O	Ratio (approx.)
2.32	15.67	0.15
2.66	18.86	0.14
3.05	21.80	0.14
2.39	16.93	0.14

Table 17: Results of SEM-EDS analysis for the annealed sample.

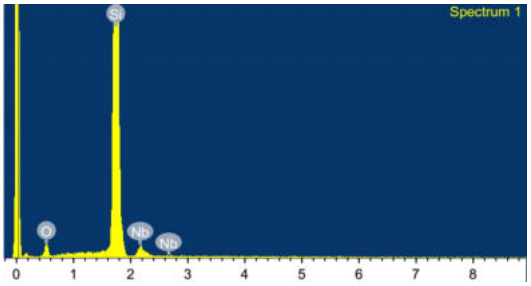

Figure 4.49: SEM-EDS spectrum of the annealed sample.

SEM-EDS analysis reveals that all the elements of interest are present in the samples (Figure 4.48 and Figure 4.49). The stoichiometry, however, still is not as desired (Table 16 and Table 17). One of the regions analysed in the non-annealed sample comes close to the intended Nb/O ratio but it was a larger particle (droplet).

As observed in Figure 4.50, the morphology of the non-annealed sample is similar to the that of sample SiLNO 9A (Figure 4.19), which is indicative of a zone 1 of Thornton's diagram structure. The deposition conditions differ in d_{target}, that was reduced by 1 cm. The white balls observed (Figure 4.52) are larger particulates (droplets) of the film's material that was melted and then were deposited.

The individual grains that constitute the clusters of film material become more easily discernible at

higher accelerating voltages (Figure 4.52), which enables the determination of the grain size distribution (Figure 4.53). The average grain size is ≈ 11.2 with a distribution width of ≈ 7.7 nm.

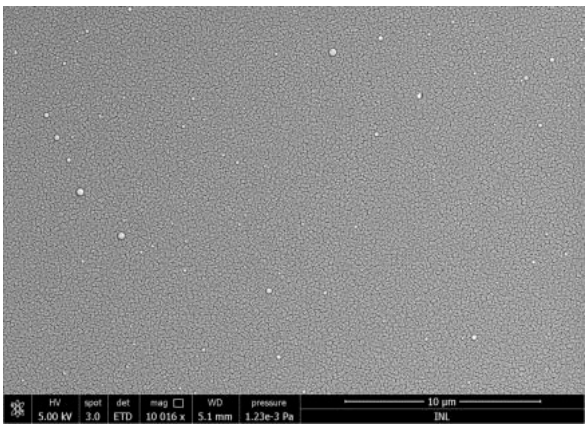

Figure 4.50: SEM image showing the surface of the $LiNbO_3$ film in the non-annealed sample.

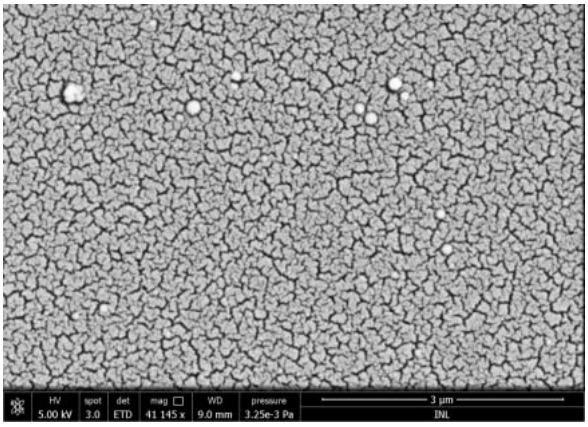

Figure 4.51: Higher magnification SEM image of the surface (non-annealed sample).

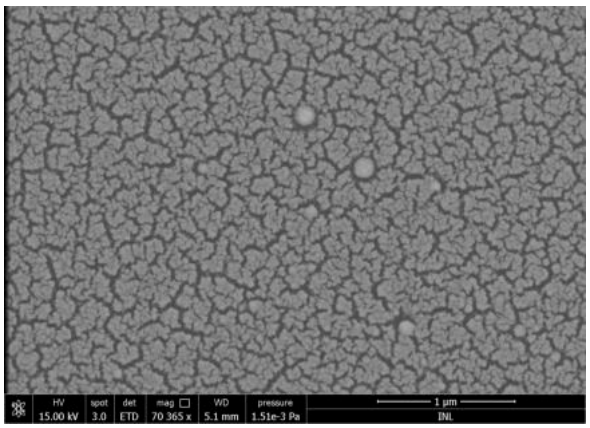

Figure 4.52: SEM image of the surface (non-annealed sample) taken at higher kV.

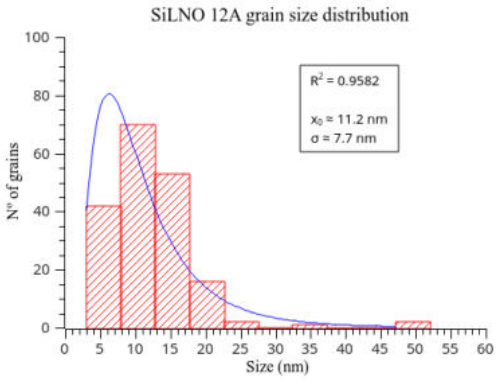

Figure 4.53: Grain size distribution of the non-annealed sample.

Figure 4.54 shows the surface of the annealed sample. The large structure on the right side of the image is a very large piece of film material that was deposited.

The cracked structure persists but the edges of the cracks seem smoother, suggesting that some level of melting or coalescence took place. Comparison of Figure 4.55 with Figure 4.51 further reinforces this

observation. This indicates that the annealing process only promoted some level of coalescence, with the structure remaining typical of zone 1 of Thornton's diagram.

Figure 4.54: SEM image showing the surface of the annealed sample.

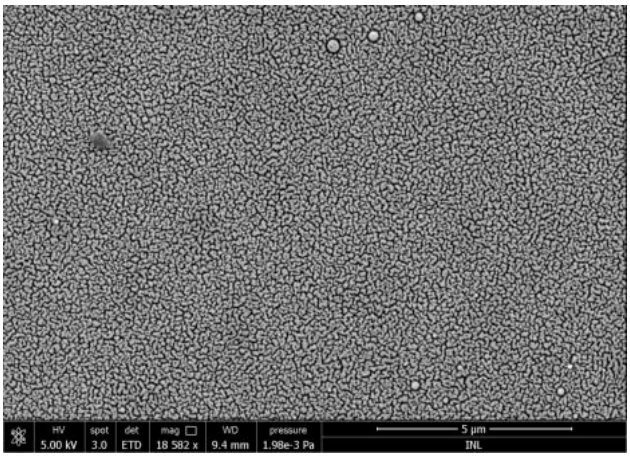

Figure 4.55: SEM image of another region of the annealed sample.

4.1.2 LNO film on SiPt substrate

Sample: SiPtLNO 4B

Substrate	T(°C)	E(mJ)	f(Hz)	d_{target}(cm)	t_{dep}(min)	P_{dep}(mbar)
SiPt	650	350	6	3	60	1

Table 18: Deposition conditions of sample SiPtLNO4B.

This sample consists of a LNO film deposited on a SiPt substrate. It has the same deposition conditions as the first sample presented, SiLNO 6A (T = RT, d_{target} = 3 cm, t_{dep} = 20 min, P_{dep} = 1 mbar), except

for the deposition temperature and time, which are 650 °C and three times longer (60 min), respectively. Compared with sample SiLNO6A, it shows the effect on film microstructure of using a high deposition temperature and depositing for a considerably longer time.

Given the oxygen content of the substrate, the SEM-EDS analysis does not allow to distinguish the percentage belonging to the film only, as the volume of interaction from which the characteristic X-rays come from includes the substrate as well. For this reason it is not possible to estimate the Nb/O ratio for this sample. However, it's possible to confirm that the intended elements are present through the SEM-EDS spectrum (Figure 4.56 and ??). In the case of Nb, given the proximity of its peak with that of Pt and the presence of the latter in the substrate, as well as the broad peak observed for it, suggests that Nb is present as shown in Figure 4.56.

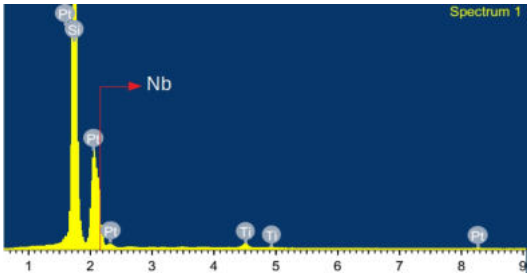

Figure 4.56: SEM-EDS spectrum of the sample's surface.

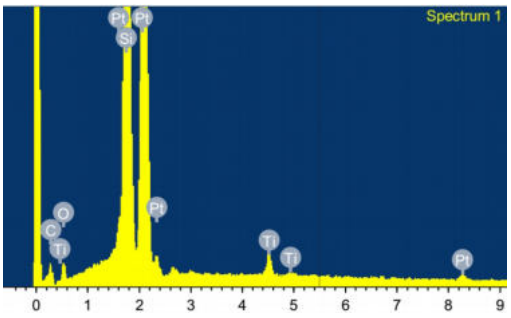

Figure 4.57: SEM-EDS spectrum of another region showing the presence of oxygen.

The surface of the film (Figure 4.58) is uniform and devoid of cracks.

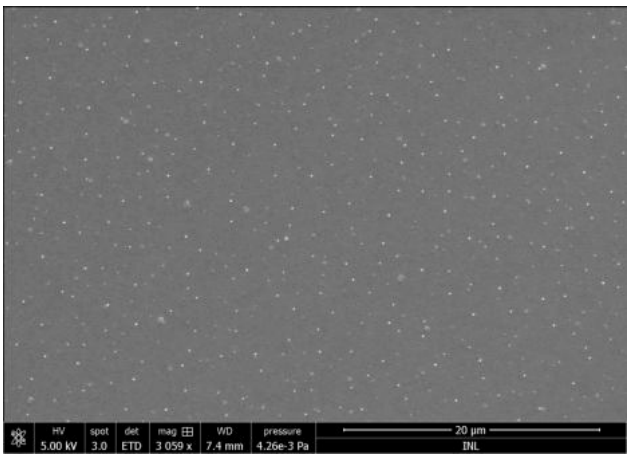

Figure 4.58: SEM image showing the surface of the $LiNbO_3$ film.

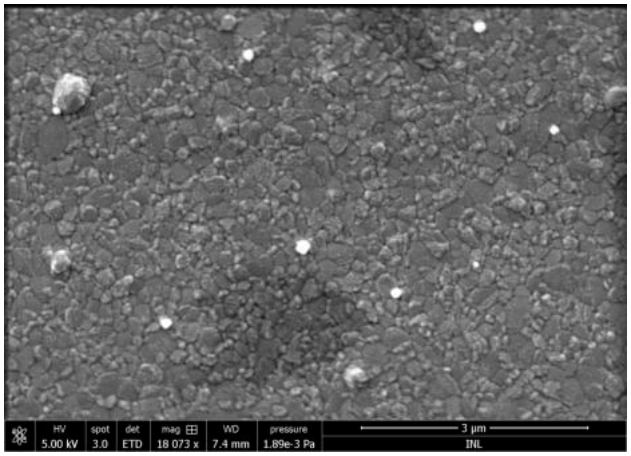

Figure 4.59: Higher magnification SEM image of the surface.

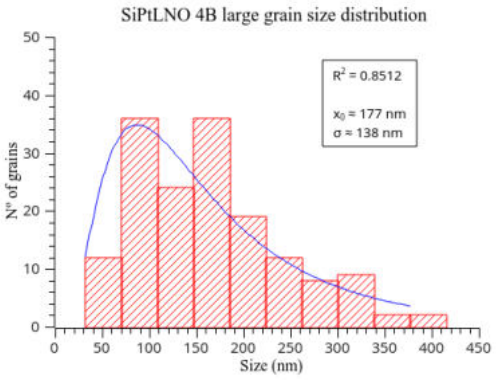

Figure 4.60: Grain size distribution of the sample.

A close-up of the surface (Figure 4.59) reveals the individual grains that constitute it, allowing the determination of their size distribution (Figure 4.60). The average grain size is ≈ 177 with a distribution width of ≈ 138 nm. There seem to be both faceted grains and flatter ones, suggesting a coexistence of zones 2 and 3 of Thornton's diagram. Possibly a transition between these zones was taking place.

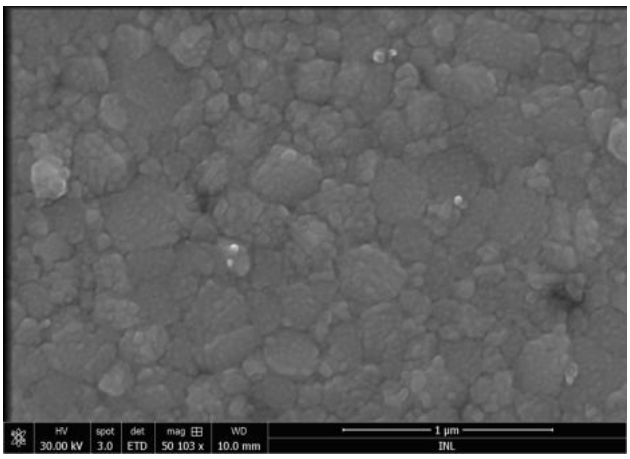

Figure 4.61: SEM image of the surface taken at high-kV.

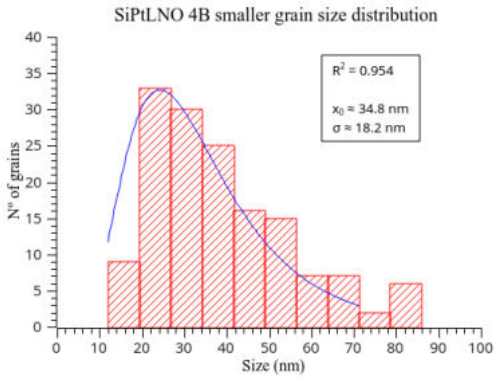

Figure 4.62: Small grain size distribution.

A high accelerating voltage SEM image of the surface (Figure 4.61) reveals that the aforementioned individual grains are, in fact, constituted by smaller ones, with the size distribution shown in Figure 4.62. The average grain size is ≈ 34.8 with a distribution width of ≈ 18.2 nm. These results indicate growth modes happening at different size scales in the films. It is noteworthy that the absence of voids between the smaller grains indicates that surface diffusion and bulk diffusion took place.

The sample was successfully used to perform dielectric measurements (capacitance vs applied electric field frequency) but some gold coating had to be applied to its surface. Figure 4.63 shows the aspect of the gold coated film. Small voids are observed but they are of nanoscopic size and did not prevent the measurements.

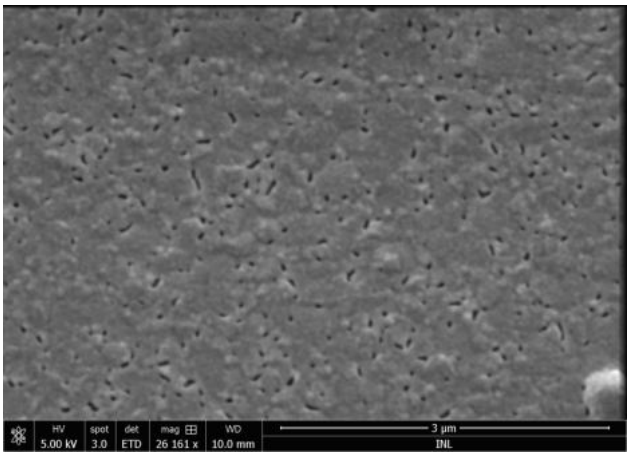

Figure 4.63: SEM image showing the gold coated films for dielectric measurements.

4.1.3 CFO-LNO film on SiPt substrate

4.1.3.1 X-ray diffractograms

The CFO-LNO samples were analysed by X-ray diffraction to confirm the presence of the phases of interest[15]. Figure 4.64 shows the diffractograms obtained for some of the samples.

The peak positions correspond to a rhombohedral crystal structure for the LNO (space group R3c (161)) and a cubic crystal structure for the CFO (space group Fd3m (227))[15], as intended. This indicates that the envisaged structure of the CFO and LNO films were stabilized in the samples, complementing the EDS stoichiometry information on these layers.

The lattice parameters of the CFO and LNO are indicated in Table 19. The observed differences relative to the values from literature are due to strain induced by the lattice mismatch between the CFO, the LNO and the substrate[15].

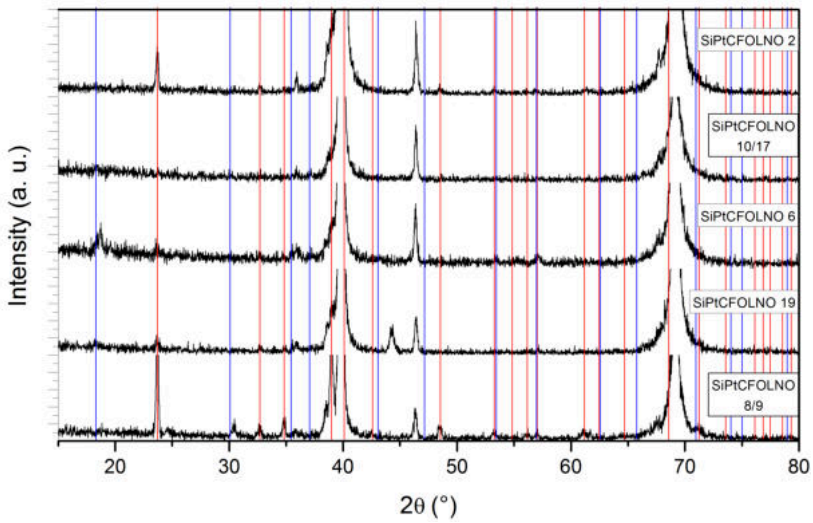

Figure 4.64: X-ray diffraction patterns of the indicated samples. The red and blue vertical lines are the diffraction peaks of the LNO and CFO, respectively. Image adapted from Ref. [15].

	LNO (rhombohedral)		CFO (cubic)
Obtained	a = 4.2773 Å	c = 13.861 Å	a = 8.2688 Å
Literature	a = 5.1494 Å	c = 13.862 Å	a = 8.3919 Å

Table 19: Lattice parameters obtained for the LNO and CFO. Calculated in Ref. [15].

.

4.1.3.2 Samples' analysis

The samples presented in the following discussion, except for the first and last one, were all deposited using the same conditions except for the deposition time, which was varied from sample to sample. As such, they show the impact of the deposition time on the film microstructure.

Sample: SiPtCFO 2

Substrate	T(°C)	E(mJ)	f(Hz)	d_{target}(cm)	t_{dep}(min)	P_{dep}(mbar)
SiPt	650	350	10	3.5	60	0.1

Table 20: Deposition conditions of the SiPtCFO 2 sample.

This sample is constituted by a CFO film alone deposited on a SiPt substrate. As mentioned in the previous sample, given the O content of the substrate, SEM-EDS analysis can't distinguish the detected O between that belonging to the film and that belonging to the substrate. For this reason, the only ratio that is safe to confirm is the Co/Fe ratio, which should be $1/2$.

All the intended elements are present (Figure 4.65). The Co/Fe ratio is above the intended (Table 21). However, note should be taken of their small atomic percentages as the film is a small region of the sample, which includes the substrate.

Atomic %		
Co	Fe	Ratio (approx.)
1.16	1.34	0.89
1.5	2	0.75
1.2	1.65	0.73
1.1	1.50	0.73
1.13	1.33	0.85
1.15	1.76	0.65

Table 21: Results of SEM-EDS analysis.

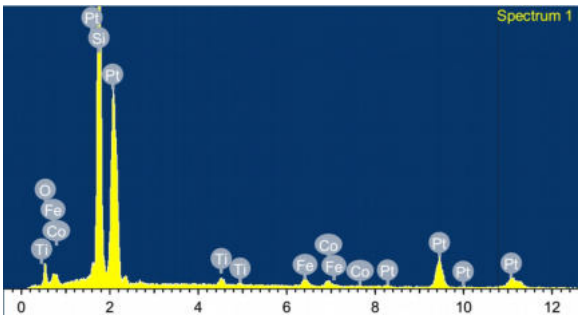

Figure 4.65: SEM-EDS spectrum of the surface.

The surface appears uniform (Figure 4.66), the main morphological feature identifiable being the white dots, which appear to be large particulates of material that were deposited. Their size distribution is shown

in Figure 4.68, presenting an average size of ≈ 990 with a distribution width of ≈ 510 nm. Some pores are also present, adjacent to the white dots (Figure 4.67).

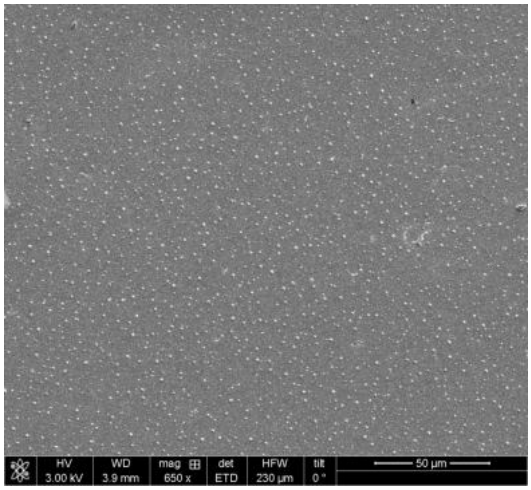

Figure 4.66: SEM image showing the surface of the sample.

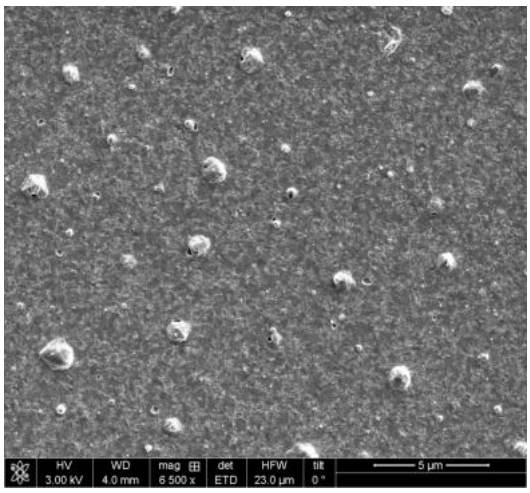

Figure 4.67: High magnification SEM image of the surface.

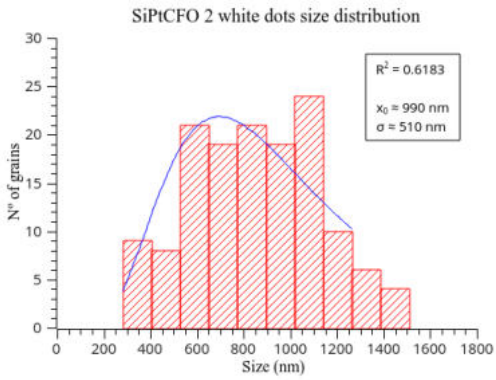

Figure 4.68: Size distribution of the white dots.

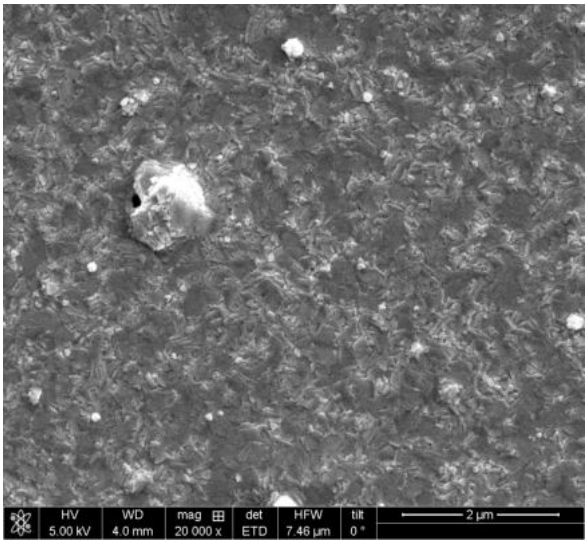

Figure 4.69: Higher magnification SEM image of the surface revealing that it is made up of grains.

A higher magnification SEM image reveals that the surface is constituted by individual grains (Figure 4.69) closely compacted together. Some regions of the surface seem smoother (the darker ones).

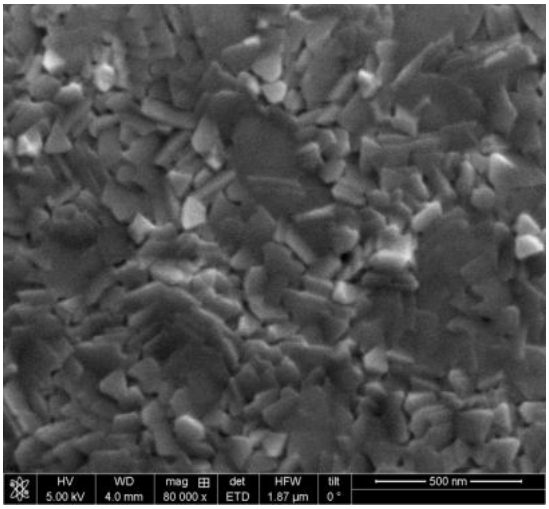

Figure 4.70: High magnification SEM image of the grains.

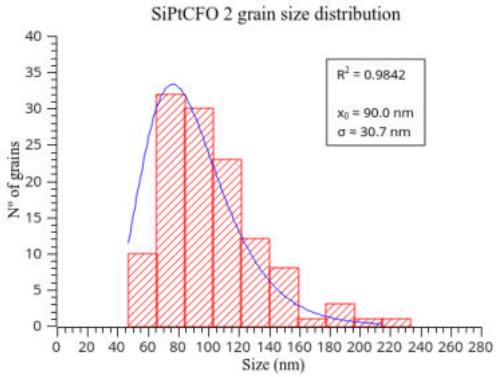

Figure 4.71: Grain size distribution.

Figure 4.70 reveals that the grains appear flat, similar to shards. The darker regions are the spots where the grains coalesced together, making the surface smoother, as previously mentioned. The average grain size is ≈ 90.0 with a distribution width of ≈ 30.7 nm (Figure 4.71). Given the faceted appearance of the grains this sample would fit into zone 2 of Thornton's diagram, perhaps in progress to zone 3 due to the observed coalescence.

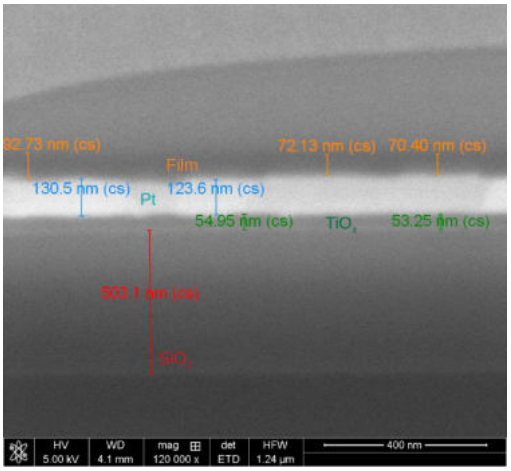

Figure 4.72: FIB-SEM image showing the cross-section of the sample with the thicknesses of the different layers.

Figure 4.72 shows a cross-section image of the sample, with the thicknesses of the film (orange measurements) and the substrate layers (blue measurements = Pt layer, green measurements = TiO_x layer, red measurement = SiO_2 layer) presented. The film is dense and no voids are observed.

Sample: SiPtCFOLNO 2

Substrate	Target	T(°C)	E(mJ)	f(Hz)	d_{target}(cm)	t_{dep}(min)	P_{dep}(mbar)
SiPt	CFO	650	350	10	5	45	0.1
	LNO			6	3	30	1

Table 22: Deposition conditions of the SiPtCFOLNO 2 sample.

Atomic %		
Co	Fe	Ratio (approx.)
0.78	1.22	0.64

Table 23: Results of SEM-EDS analysis.

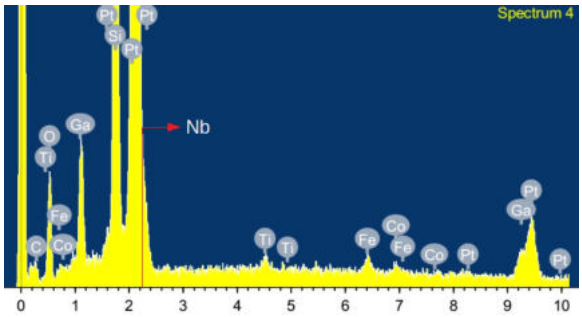

Figure 4.73: EDS spectrum of the cross-section acquired from the FIB-SEM.

SEM-EDS analysis confirms the presence of the elements of interest (Figure 4.73). Similarly to other samples, Nb seems to have been overlapped with Pt, resulting in a broad peak for the latter. Regarding the ratio Co/Fe (Table 23), several regions were analysed by SEM-EDS but only one displayed both peaks. In the other regions, either one or both of the peaks were not shown. However, given the proximity of the peaks of Co and Fe, it's possible that in regions where one was detected the other element was present as well. The Co/Fe ratio is near to the envisaged one.

The surface of the sample (Figure 4.74) shows regions of different contrast, with grain boundaries (Figure 4.75) visible on the darker region - this is the film layer, while the brighter regions (top-left and right margin of Figure 4.74) are the Pt layer of the substrate, exposed due to film scratching during handling. This is confirmed in Figure 4.76 where the darker region seems to be over the bright one, suggesting that it is the film layer, confirmed as well by EDS analysis of sample SiPtCFOLNO 15. Additionally, the great prevalence of pores (black spots) is observed in the Pt layer of other samples with SiPt substrates, when analysing their cross-section images. This further confirms that this region is indeed the substrate's Pt layer which was exposed. Comparison of Figure 4.77 with Figure 4.119 further confirms this. Finally, the morphology observed in Figure 4.69 for the $CoFe_2O_4$ also contributes to this interpretation, though the difference in deposition conditions could be argued to be the reason for the difference.

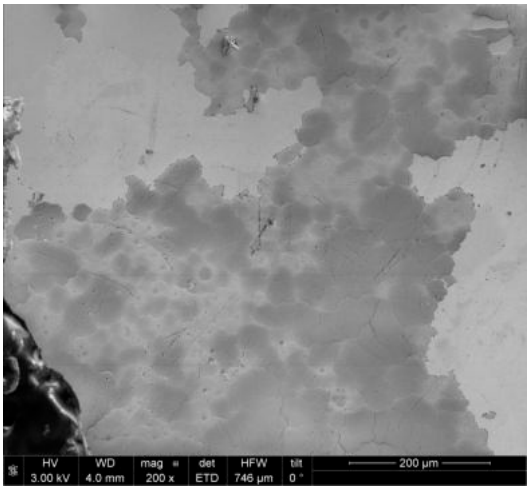

Figure 4.74: SEM image showing the surface of the sample.

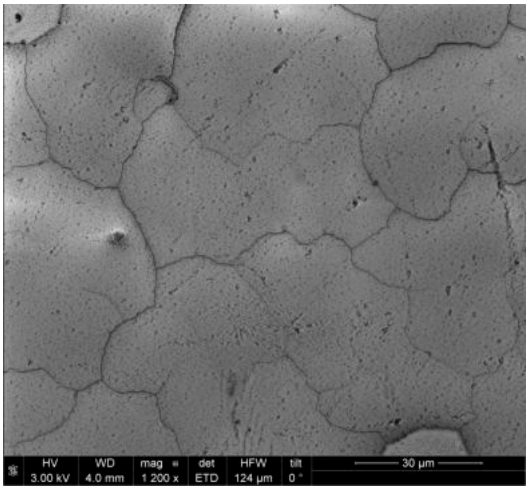

Figure 4.75: High magnification SEM image of the film's surface, displaying the grain boundaries.

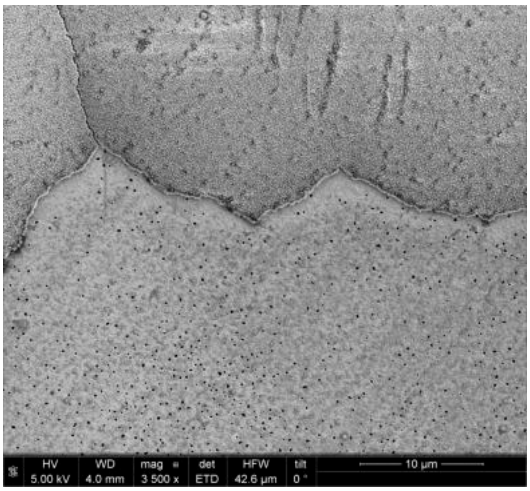

Figure 4.76: High magnification SEM image of a boundary between the aforementioned dark and bright regions (upper and lower halves of the image, respectively).

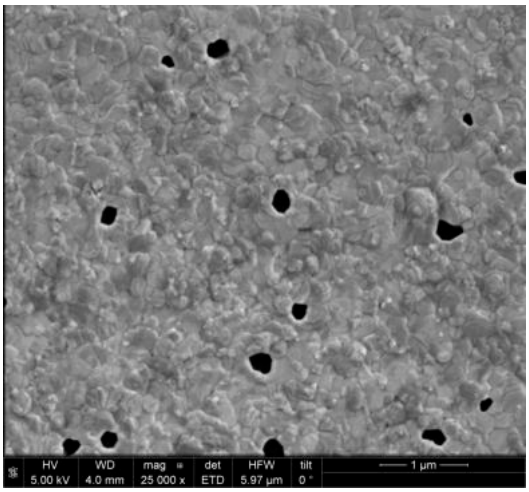

Figure 4.77: High magnification SEM image of the bright region.

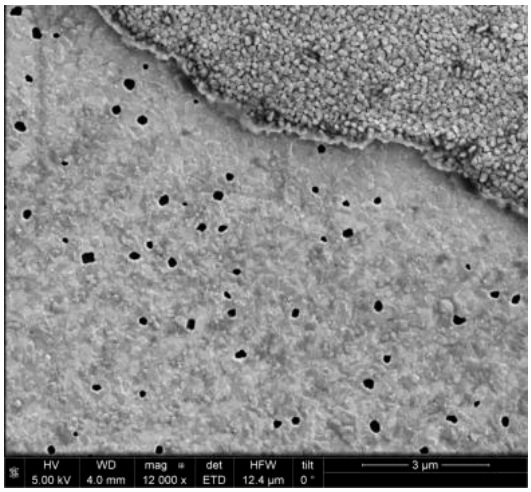

Figure 4.78: Higher magnification SEM image of the region showed in Figure 4.76.

(Figure 4.78) shows that the edge of the film's layer is particularly bright and seems to have some thickness, suggesting it may be the $CoFe_2O_4$ layer protruding from under the $LiNbO_3$ layer.

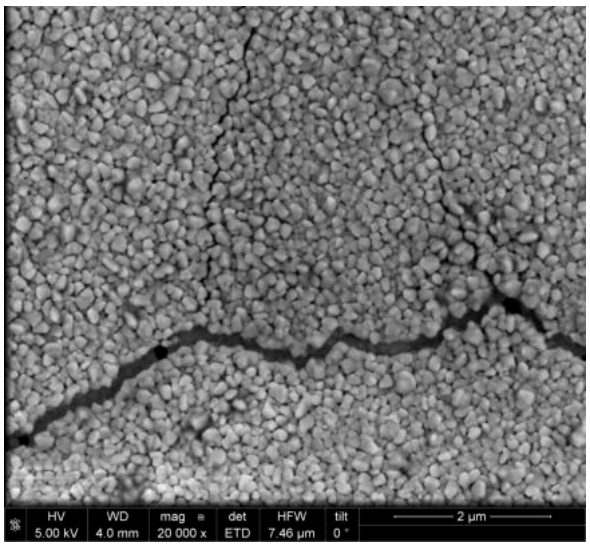

Figure 4.79: High magnification SEM image of the film's surface.

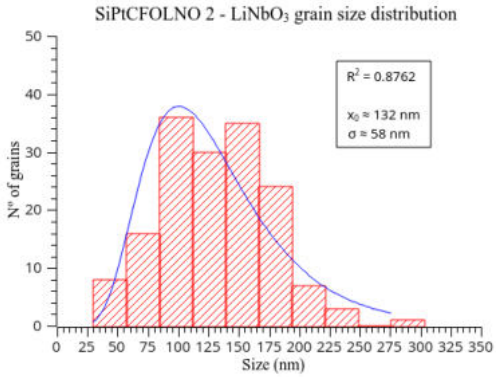

Figure 4.80: $LiNbO_3$ grain size distribution.

Close inspection of the film's surface (LNO layer, Figure 4.79) reveals that it is constituted by individual, faceted grains, with an average size of $\approx$ 132 and a distribution width of $\approx$ 58 nm (Figure 4.80). The faceted grains are suggestive of a zone 2 of Thornton's diagram structure.

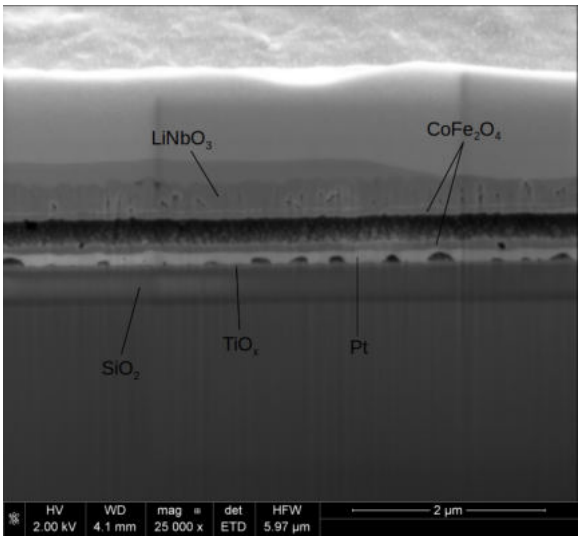

Figure 4.81: FIB-SEM cross-section image of the sample with the different layers identified.

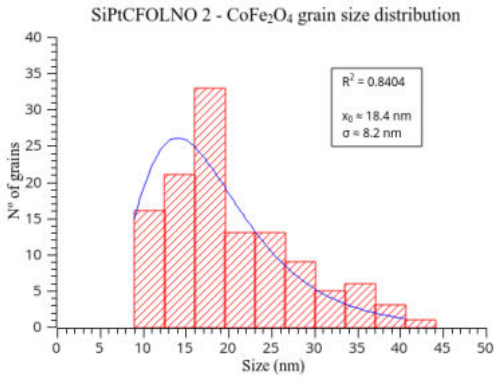

Figure 4.82: $CoFe_2O_4$ grain size distribution.

Observation of the cross-section (Figure 4.81) reveals a large gap below the surface layer and the rest of the sample. Under it, a thin layer with grains on its surface is observed, most likely the $CoFe_2O_4$ layer. The $CoFe_2O_4$ average grain size is $\approx$ 18.4 with a distribution width of $\approx$ 8.2 nm (Figure 4.82). It is not possible to predict the morphology of the grains and consequently in which Thornton's diagram zone this layer would fit, but given its dense aspect and surface constituted by grains a zone 2 structure seems the most plausible. The $LiNbO_3$ layer shows some pores. At its base, part of the $CoFe_2O_4$ layer is present, as

indicated by the observed contrast difference.

The observed gap was most likely originated by fracture of the CFO layer, dividing it in half as shown in Figure 4.81.

The thickness of the different layers is presented in Figure 4.83.

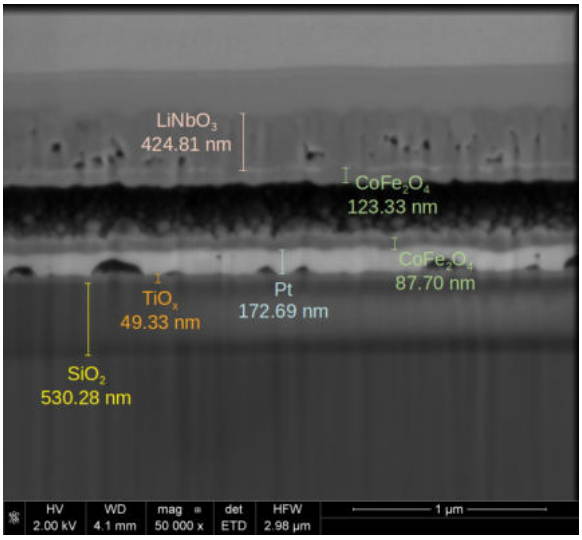

Figure 4.83: High magnification FIB-SEM image of the cross-section with the different layer's thicknesses.

Sample: SiPtCFOLNO 6

Substrate	Target	T(°C)	E(mJ)	f(Hz)	d_{target}(cm)	t_{dep}(min)	P_{dep}(mbar)
SiPt	CFO	650	350	10	5	60	0.1
	LNO			6	3	45	1

Table 24: Deposition conditions of the SiPtCFOLNO 6 sample.

Atomic %		
Co	Fe	Ratio (approx.)
1.64	3.78	0.44
1.70	2.79	0.61
2.72	4.22	0.64
1.04	1.86	0.56
2.91	3.60	0.81

Table 25: Results of SEM-EDS analysis.

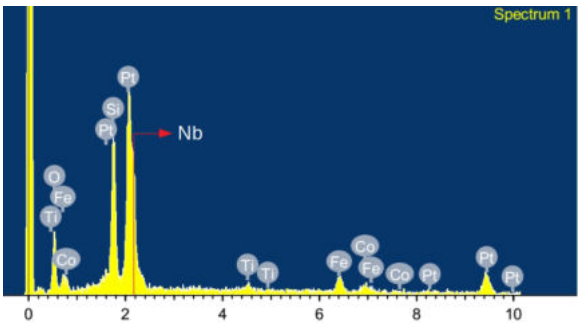

Figure 4.84: SEM-EDS spectrum of the surface.

SEM-EDS analysis confirms the presence of all elements of interest (Figure 4.84), with Nb experiencing the aforementioned issue of overlapping with the Pt but its presence being revealed by the broad Pt

peak. The Co/Fe ratio is generally close to the intended value in the sample (Table 25).

The sample's surface (LNO layer) shows a rough morphology and grainy appearance (Figure 4.85). Closer inspection reveals that it is constituted by individual, faceted grains (Figure 4.86) with an average size of $\approx$ 113 and a distribution width of $\approx$ 53 nm (Figure 4.87). There are spots where the grains are not closely-packed together. The structure fits in zone 2 of Thornton's diagram.

Figure 4.85: SEM image showing the surface of the sample ($LiNbO_3$ layer).

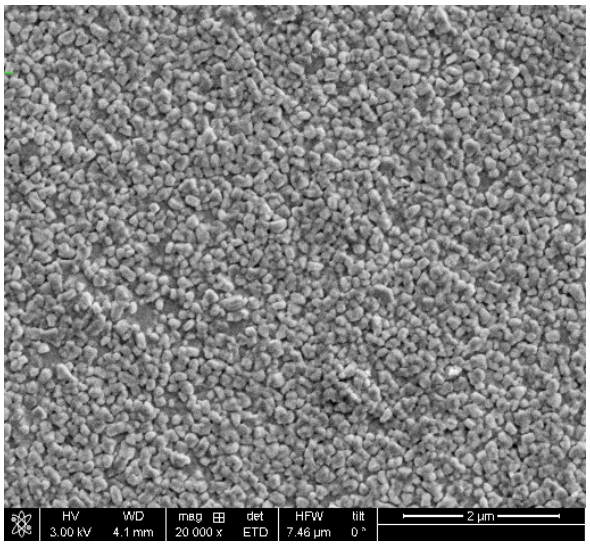

Figure 4.86: High magnification SEM image of the $LiNbO_3$ layer.

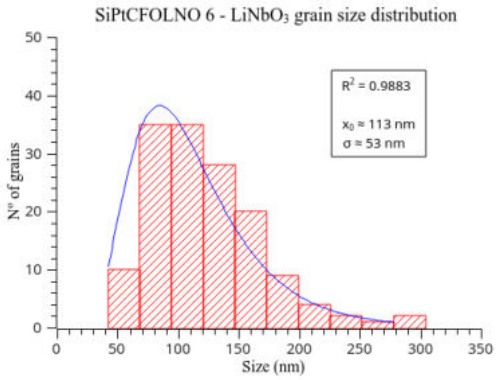

Figure 4.87: $LiNbO_3$ grain size distribution.

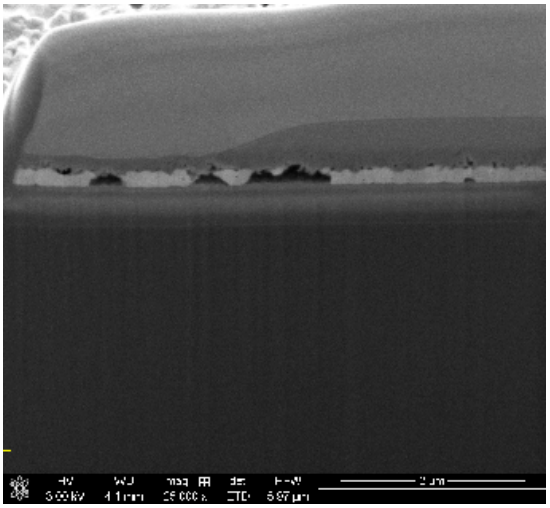

Figure 4.88: Cross-section image of the sample imaged with the FIB-SEM.

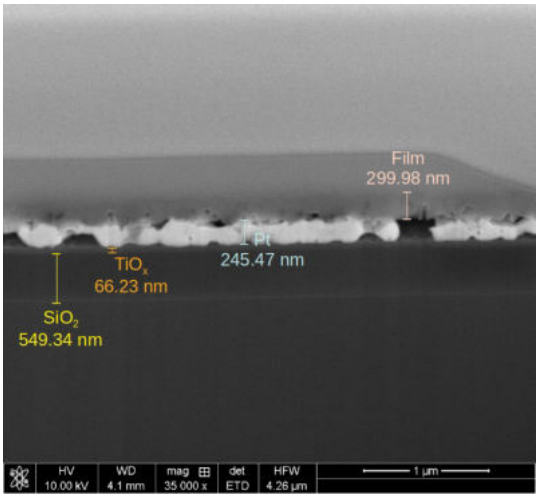

Figure 4.89: High magnification image of the cross-section with the thicknesses of the different layers indicated, imaged by FIB-SEM.

Cross-section imaged by the FIB-SEM reveal the different layers of the sample (Figure 4.88 and Figure 4.89). However, in the film layer, no distinction between the two films is observed. The $CoFe_2O_4$ layer seems absent when compared with the previous sample (check Figure 4.83), suggesting that it is difficult to distinguish with the current imaging parameters, as its presence was confirmed by SEM-EDS (Figure 4.84). Some pores are observed in the film.

Sample: SiPtCFOLNO 8

Substrate	Target	T(°C)	E(mJ)	f(Hz)	d_{target}(cm)	t_{dep}(min)	P_{dep}(mbar)
SiPt	CFO	650	350	10	5	60	0.1
	LNO			6	3	75	1

Table 26: Deposition conditions of sample SiPtCFOLNO 8.

Atomic %			
Co	Fe	Nb	Co/Fe ratio (approx.)
0.73	1.42	16.18	0.51
0.70	1.32	15.94	0.53
0.70	1.14	16.40	0.61

Table 27: Results of SEM-EDS analysis.

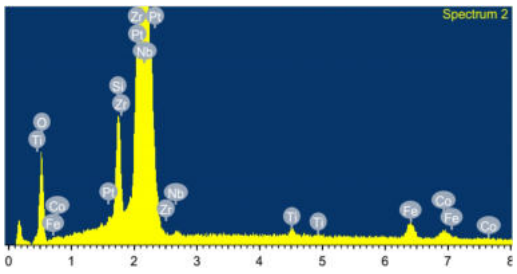

Figure 4.90: SEM-EDS spectrum of the surface.

SEM-EDS analysis shows that all elements of interest are present (Figure 4.90). The Zr detected probably results from confusion with either the Nb or Pt, given the proximity of their peaks. The Co/Fe ratios appear very close to the intended proportion.

The sample's surface (LNO layer) is rough, with domes visible throughout it (Figure 4.91). Smoother regions (bottom-right of Figure 4.91 for example) are also present.

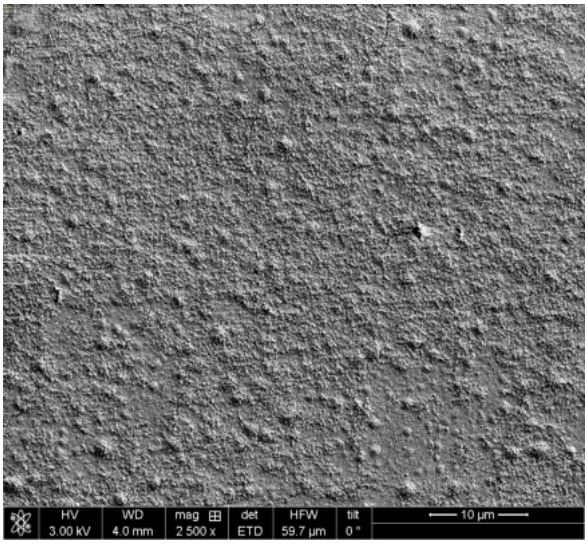

Figure 4.91: SEM image showing the surface of the sample ($LiNbO_3$ layer).

Closer inspection of the surface reveals that the roughness is due to the faceted grains that constitute it (Figure 4.92). Their average size is $\approx$ 340 with a distribution width of $\approx$ 99 nm (Figure 4.93). Considerably smaller grains are visible between the larger ones (left side of Figure 4.92, magnified view in Figure 4.94), constituting the smoother regions mentioned in Figure 4.91. These smaller grains have an average size of $\approx$ 87.7 and a distribution width of $\approx$ 34.7 nm (Figure 4.95) and have coalesced to some extent. Some cracks are also visible.

The faceted grains suggest a zone 2 structure of Thornton's diagram. The domes observed may be the beginning of the formation of recrystallized grains (check Fig. 3D of [10]), typical of zone 3 of Thornton's diagram.

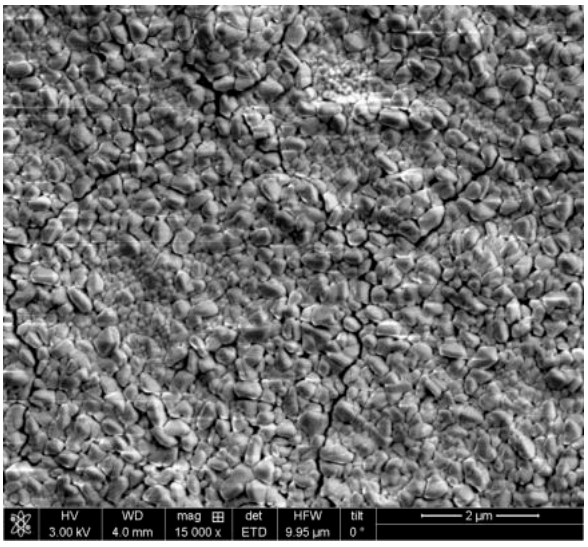

Figure 4.92: High magnification SEM image of the surface.

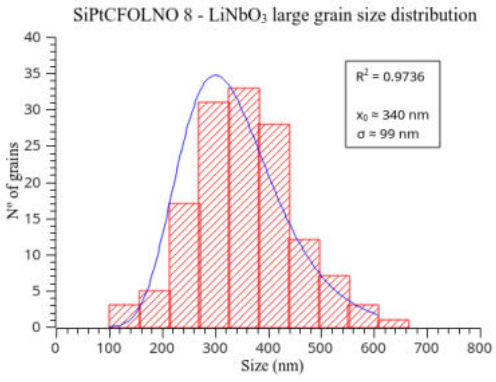

Figure 4.93: Size distribution of the LNO grains.

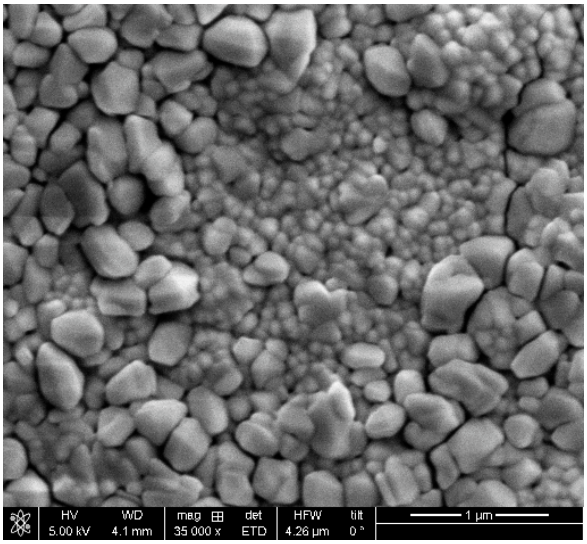

Figure 4.94: High magnification SEM image of the surface showing the LNO faceted grains.

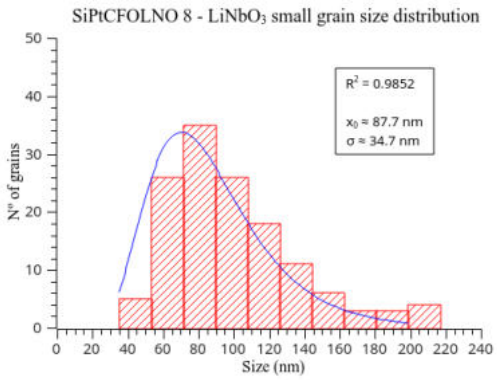

Figure 4.95: Size distribution of the smaller LNO grains.

Cross-section images reveal pores in the film (Figure 4.96). Closer inspection shows that the film is constituted by lobular components, with the pores defining the boundaries between them (Figure 4.97). These lobes are reminiscent of a columnar structure, typical of zone 2 of Thornton's diagram. The LNO and CFO layers are indistinguishable.

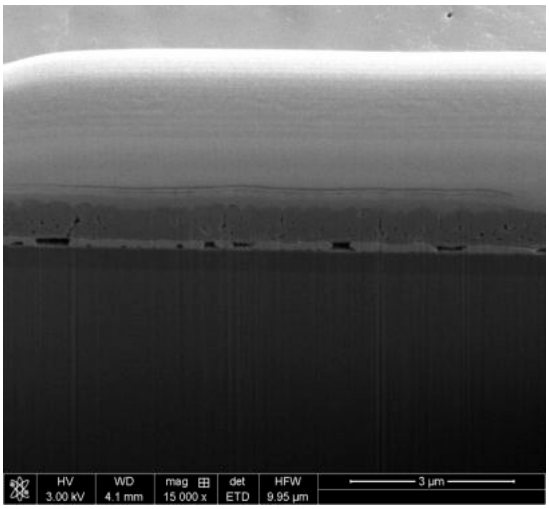

Figure 4.96: Cross-section image of the sample showing its different layers imaged by the FIB-SEM.

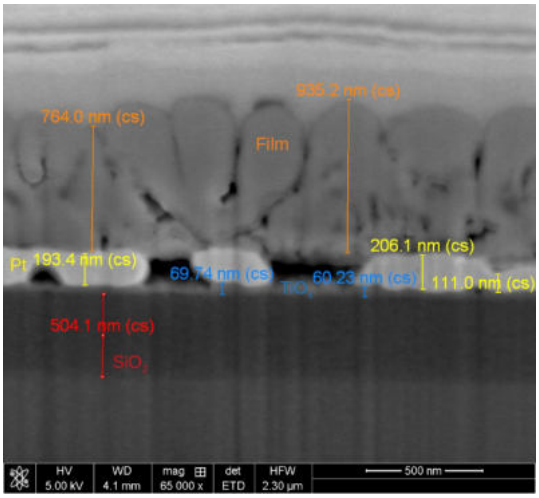

Figure 4.97: The thickness of the different layers (red = SiO_2 layer, blue = TiO_x layer, yellow = Pt layer, orange = film).

Sample: SiPtCFOLNO 9

This sample is a repetition of the previous one. Its deposition conditions are the same except for the degasification time - 90 minutes versus 35 minutes in the previous one.

Atomic %		
Co	Fe	Ratio (approx.)
0.40	0.69	0.58
1.28	1.80	0.71

Table 28: Results of SEM-EDS analysis.

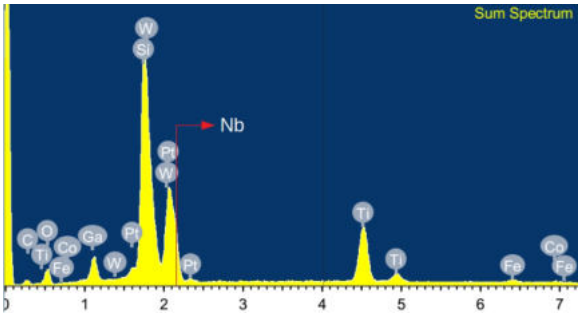

Figure 4.98: SEM-EDS spectrum of the sample's cross-section.

SEM-EDS analysis confirms the presence of all elements of interest (Figure 4.98). The presence of W is probably some confusion with the Si, as their peaks are close. The presence of Nb is deduced from the asymmetric peak of Pt. Regarding the Co/Fe ratios, several regions were analysed but only two generated atomic percentages, with one of them close to the desired ratio (Table 28).

The sample's surface (LNO layer) appears flat with the exception of the spherical particulates observed (Figure 4.99). Their average size is ≈ 1.49 with a distribution width of ≈ 0.42 μm (Figure 4.100), indicating that they are droplets. Figure 4.101 provides a closer look of the surface, revealing grains at the early stages of formation. Additionally, a large, spherical particulate is particularly bright and a depression of similar diameter is seen close above, probably an impact crater for this particulate. This confirms that the spherical particulates seen throughout the film are indeed macroparticles ejected from the target during the ablation process.

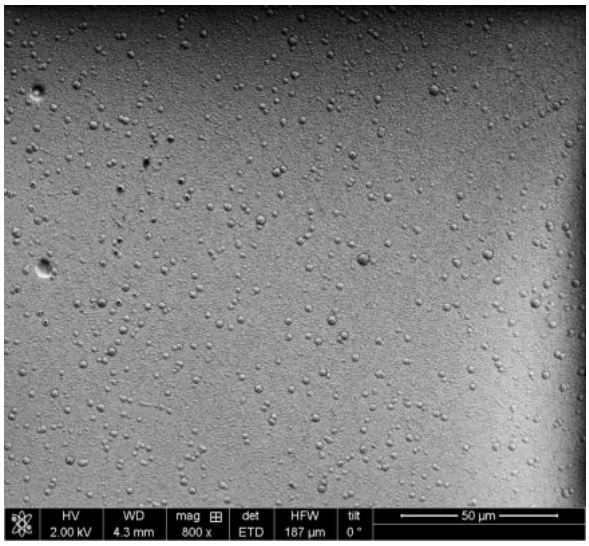

Figure 4.99: Surface of the sample showing the $LiNbO_3$ layer imaged by the SEM.

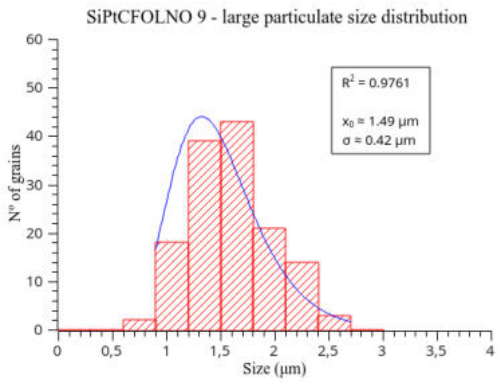

Figure 4.100: Size distribution of the large particulates.

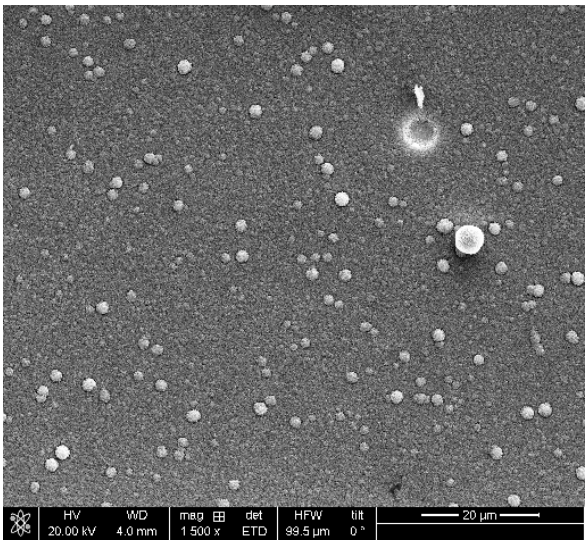

Figure 4.101: High magnification SEM image of the surface.

Closer inspection of the surface reveals a grainy morphology, which extends to the spherical particulates as well (Figure 4.102). The aforementioned grains at the early stage of formation are agglomerations of smaller grains. These agglomerations have an average size of $\approx$ 756 with a distribution width of $\approx$ 179 nm (Figure 4.103). It's also possible to identify regions where no agglomerations are observed. The presence of both agglomerations and regions without them is reminiscent of the structure observed in Figure 4.91.

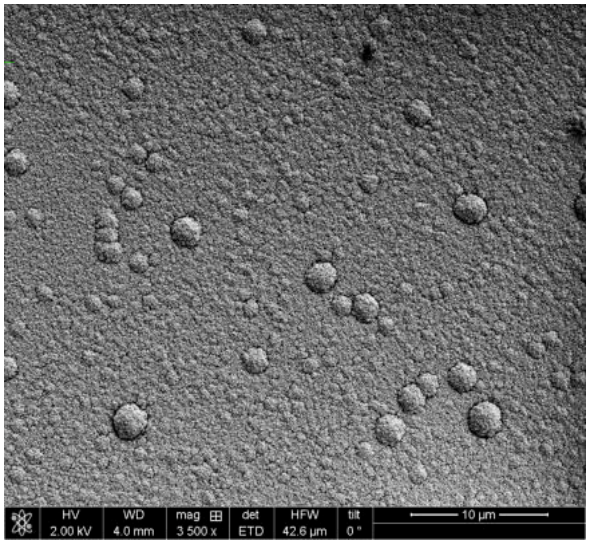

Figure 4.102: Higher magnification SEM image of the surface.

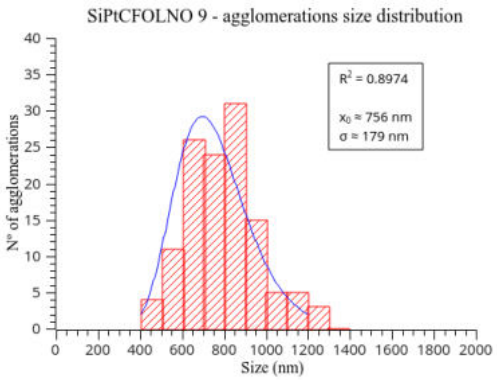

Figure 4.103: Size distribution of the agglomerations.

Figure 4.104 shows that the surface is uneven and constituted by small, individual grains connecting to larger ones, indicating grain coalescence during film growth. The grain's average size is $\approx$ 54.0 with a distribution width of $\approx$ 16.7 nm (Figure 4.105).

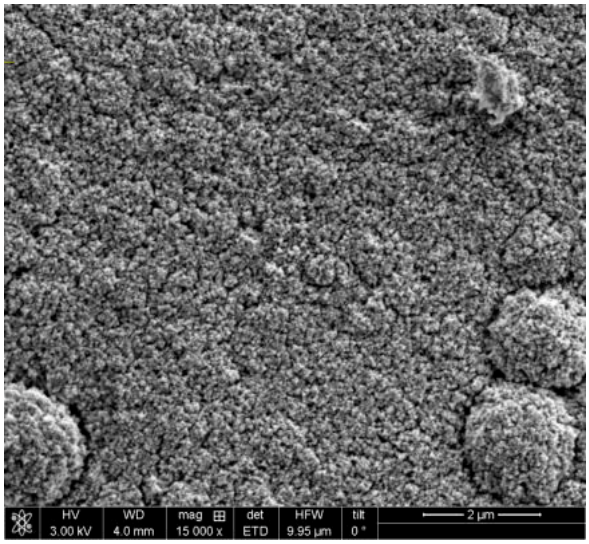

Figure 4.104: High magnification SEM image of the surface.

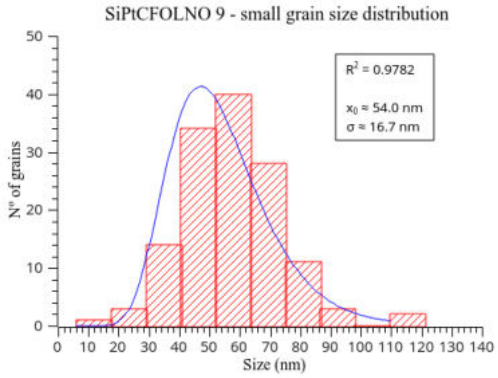

Figure 4.105: Size distribution of the small grains.

Cross-sectional images of the sample reveal a film with a porous structure (Figure 4.107). The first few hundred nanometres appear to have less voids, consistent with that observed in Figure 4.97, in which the same happens in the first $\approx$ 500 nm. The significantly increased film thickness of the present sample, for the same deposition conditions, suggests that the previous sample's cross-section was observed in a region where the film thickness wasn't maximal such as in a film edge. This effect is due to the ablation plume's shape that generates films which are thinner at the edges, as illustrated in Figure 4.106.

No distinct layers are distinguishable for the CFO and LNO.

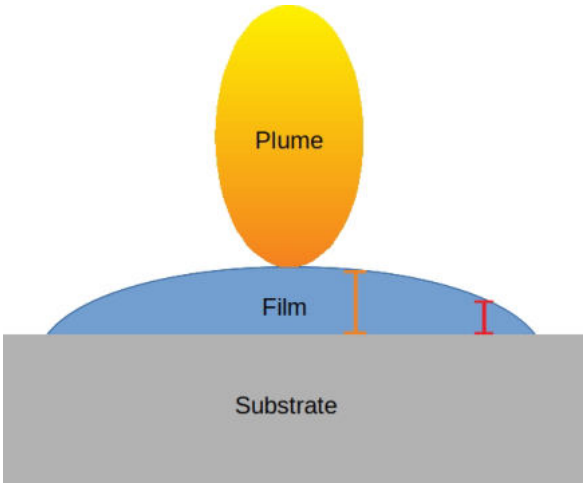

Figure 4.106: The non-uniformity of the film thickness due to the plume's shape. The region imaged in the previous sample corresponds to the red line while that imaged in the present sample corresponds to the orange one.

The sample's surface morphology and the porous film bulk suggest a zone 1 of Thornton's diagram. This interpretation is also supported by the similarity between Figure 4.107 and computer simulations of the expected structure of zone 1 [16,17], Figure 4.108. This image shows the film structure at different instants in time during deposition, for a film incident at the indicated angle and substrate temperature. However,

the agglomerations observed at the surface may indicate the beginning of coalescence and transition to zone T.

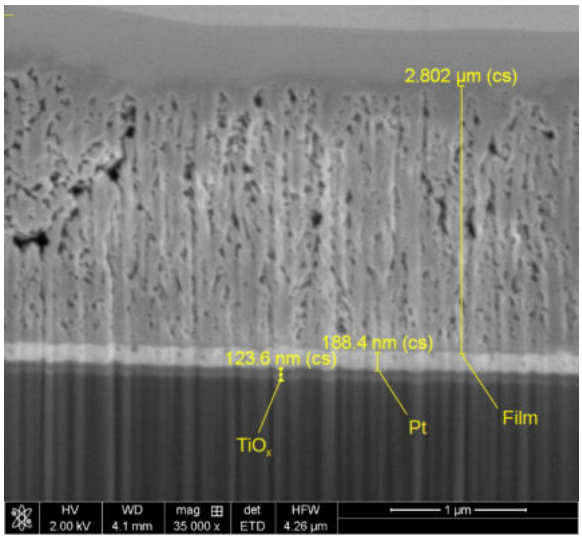

Figure 4.107: FIB-SEM image of the cross-section of the sample with the thicknesses of its layers.

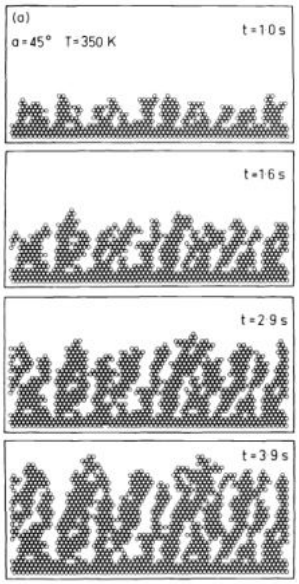

Figure 4.108: Excerpt from Figure 5 of Ref. [16]. Original simulations from Ref. [17].

Sample: SiPtCFOLNO 10

Substrate	Target	T(°C)	E(mJ)	f(Hz)	d_{target}(cm)	t_{dep}(min)	P_{dep}(mbar)
SiPt	CFO	650	350	10	5	75	0.1
	LNO			6	3	30	1

Table 29: Deposition conditions of sample SiPtCFOLNO 10.

Atomic %		
Co	Fe	Ratio (approx.)
0.16	0.34	0.47
0.47	0.77	0.61
0.47	0.67	0.70
0.50	0.82	0.61
0.34	0.49	0.69
0.54	0.87	0.62
0.54	0.83	0.65
0.32	0.52	0.62
0.40	0.60	0.67
0.29	0.56	0.52

Table 30: Results of SEM-EDS analysis.

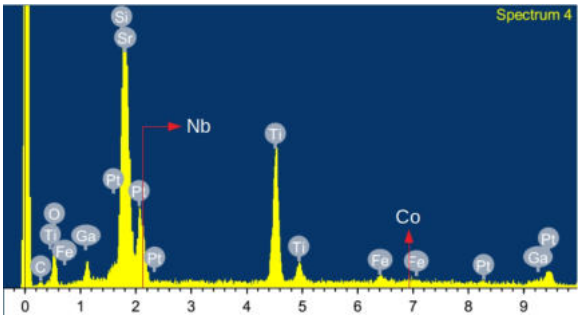

Figure 4.109: SEM-EDS spectrum of the sample's cross-section.

SEM-EDS analysis confirms the presence of all elements of interest (Figure 4.109), with the presence of both Nb and Co deduced from the asymmetric Pt peak and the beginning of formation of the Co peak, respectively. Generally the Co/Fe ratios are close to the appropriate proportions (Table 30).

The sample's surface appears to have the same structure as the previous sample (Figure 4.102). Closer inspection reveals a morphology identical to that observed in Figure 4.104. However, the agglomerations of the individual grains seem more strongly defined compared to the previous sample, suggesting that the grains coalesced more. The agglomeration's average size is ≈ 492 with a distribution width of ≈ 215 nm (Figure 4.112).

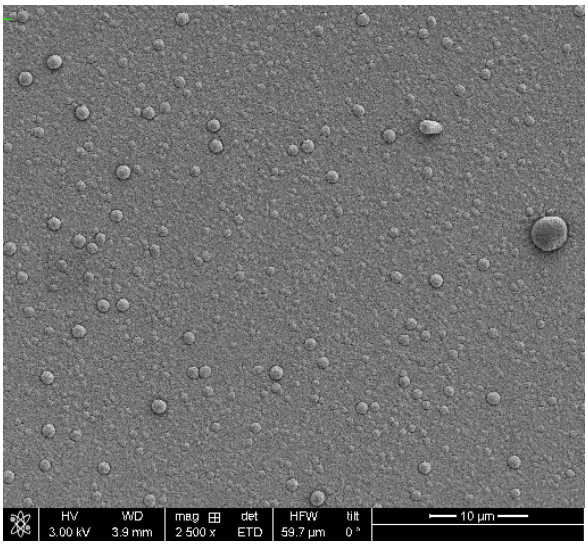

Figure 4.110: SEM image of the surface of the sample.

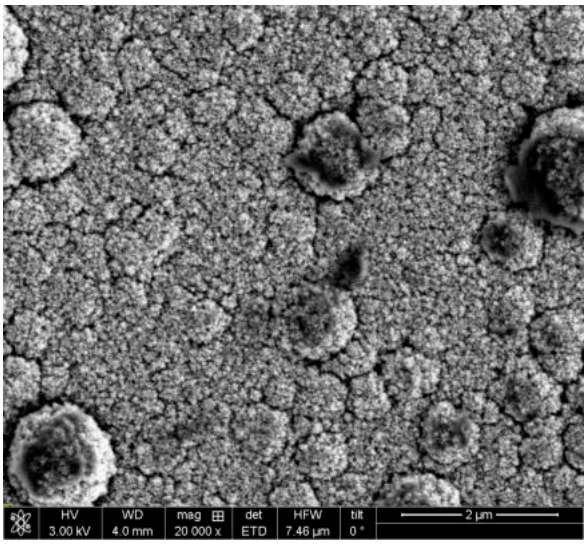

Figure 4.111: High magnification SEM image of the surface.

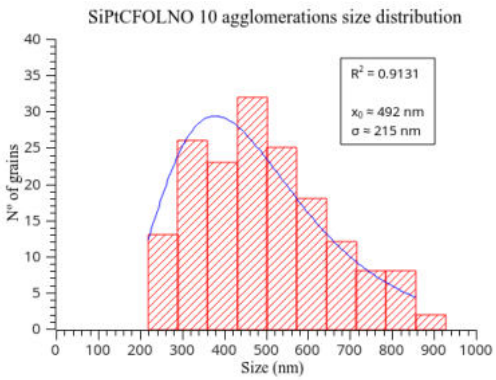

Figure 4.112: Size distribution of the agglomerations.

Similarly to the previous sample, the surface (LNO layer) is constituted by individual grains (Figure 4.113) with average size ≈ 34.6 and a distribution width of ≈ 13.5 nm (Figure 4.114).

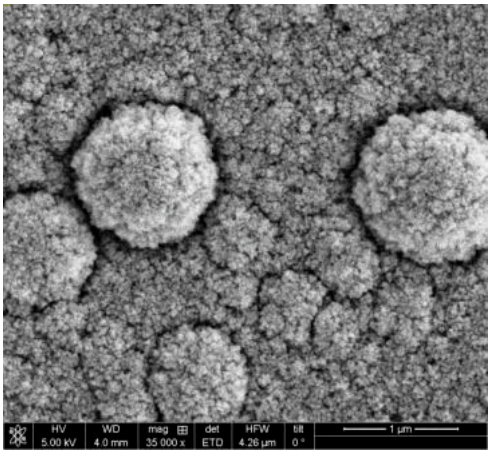

Figure 4.113: The individual grains that constitute the film.

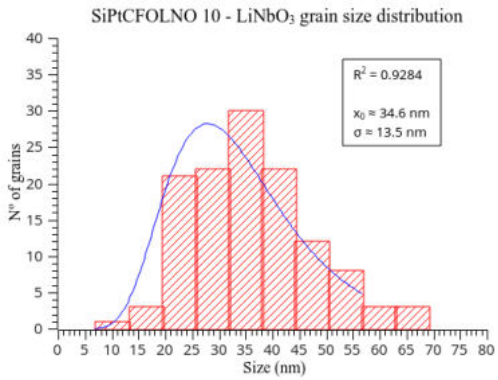

Figure 4.114: Size distribution of the LNO grains.

Figure 4.115 shows the cross-section of the sample, revealing the same structure as observed in Figure 4.107. However, the columns seem wider, suggesting further coalescence compared to the previous sample.

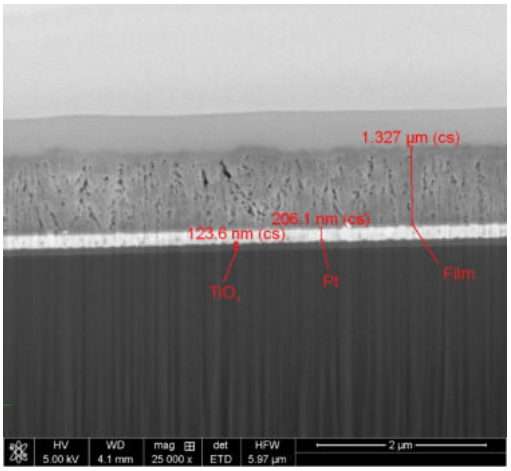

Figure 4.115: FIB-SEM image of the cross-section of the sample revealing its different layers and their thicknesses.

Due to the similarity to the previous sample in surface morphology and film cross-section, the present sample would fit in zone 1 of Thornton's diagram. However, given the greater degree of coalescence observed a zone T structure seems more adequate. The only difference in the deposition conditions relative to the previous sample is the deposition times of each film, leading to the exposure to the high temperature during more time and, thus, promoting grain coalescence and film densification.

Sample: SiPtCFOLNO 15

Substrate	Target	T(°C)	E(mJ)	f(Hz)	d_{target}(cm)	t_{dep}(min)	P_{dep}(mbar)
SiPt	CFO	650	350	10	5	20	0.1
	LNO			6	3	10	1

Table 31: Deposition conditions of sample SiPtCFOLNO 15.

Atomic %			
Co	Fe	Nb	Co/Fe ratio (approx.)
0.26	0.38	2.75	0.68
0.30	0.34	3.03	0.88
0.20	0.32	2.36	0.63
0.27	0.40	2.46	0.68
0.23	0.29	2.38	0.79
0.27	0.35	2.52	0.77
0.22	0.41	2.72	0.54
0.23	0.28	2.23	0.82

Table 32: Results of SEM-EDS analysis.

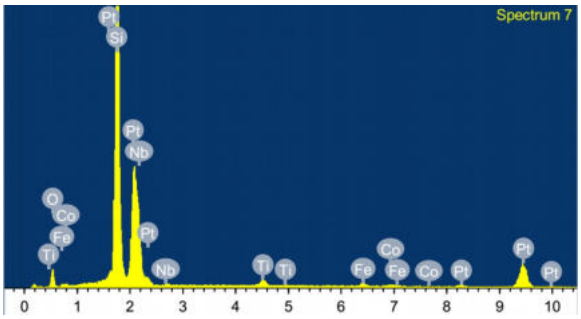

Figure 4.116: SEM-EDS spectrum of the sample's surface.

SEM-EDS analysis confirms the presence of all elements of interest (Figure 4.116). The Co/Fe ratio is higher than intended overall but close (Table 32). The difference is due to the small detected amounts in the sample, due to the high signal from the substrate.

The sample's surface appears smooth but with some texture (Figure 4.117). The bright areas are regions where the film was removed, as confirmed in Figure 4.118. The film's surface (LNO layer) has a grainy appearance and large, spherical particulates are observed throughout it. Grain boundaries are observed as well.

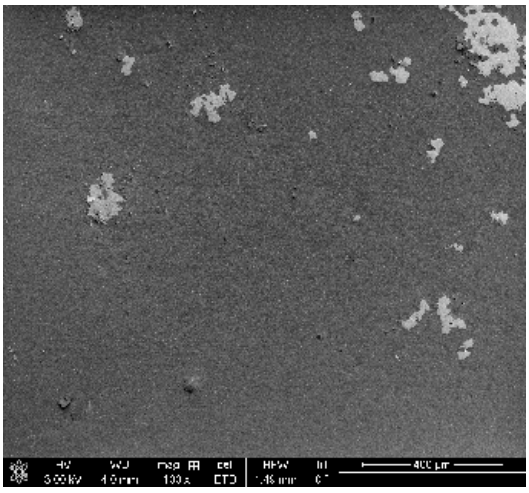

Figure 4.117: SEM image of the surface of the sample.

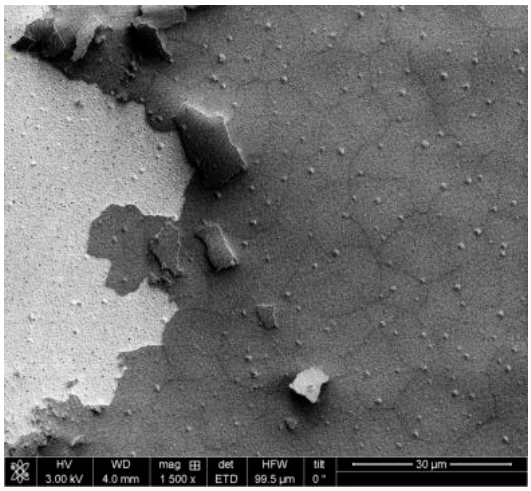

Figure 4.118: High magnification SEM image of the surface.

SEM-EDS analysis of a bright region where the film was removed confirms only elements from the substrate (Figure 4.120), confirming that what is being observed is the substrate's Pt layer.

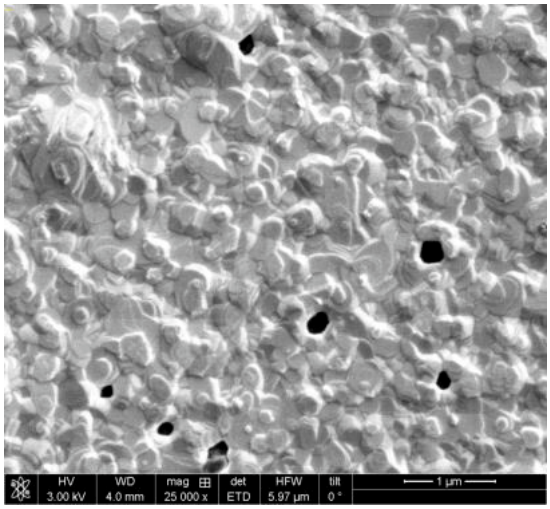

Figure 4.119: High magnification SEM image of a bright region.

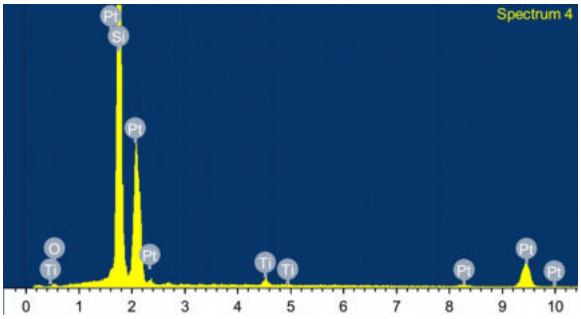

Figure 4.120: SEM-EDS spectrum of a bright region.

Figure 4.121 reveals that the LNO layer is constituted by individual grains interspersed by flatter regions. The larger particulates observed in Figure 4.118 are constituted by these grains closely packed together. Some voids are also observed. The average grain size is $\approx$ 120 with a distribution width of $\approx$ 23 nm (Figure 4.123). Closer inspection reveals a morphology identical to that observed in Figure 4.14 and Figure 4.94. The flatter regions are constituted by much smaller grains that have coalesced to some extent.

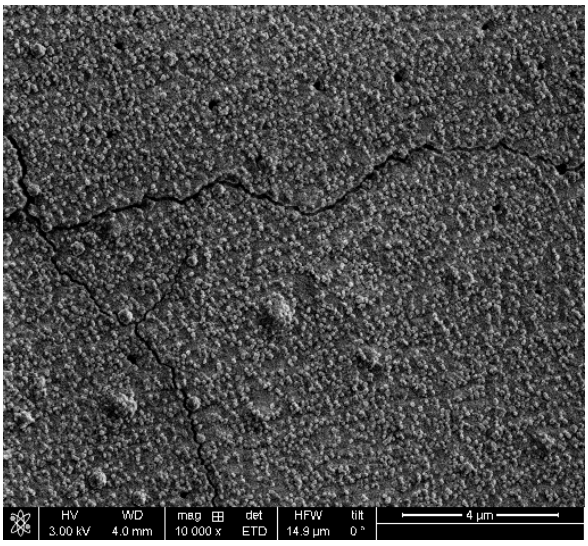

Figure 4.121: High magnification SEM image of the surface.

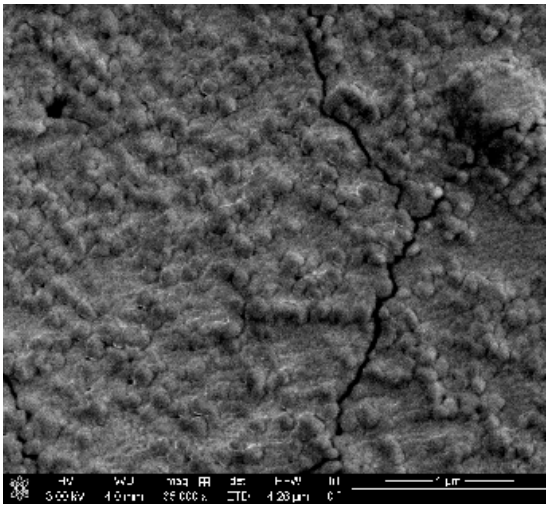

Figure 4.122: Higher magnification SEM image of the surface.

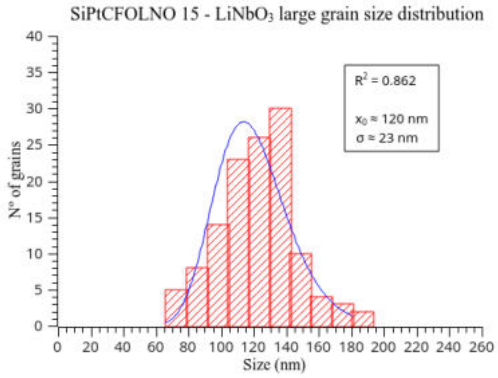

Figure 4.123: Size distribution of the LNO large grains.

Closer inspection of the grains (Figure 4.124) shows that their surfaces appear smooth but orientations characteristic of faceted grains, such as those seen in Figure 4.94, are recognizable. This smoother appearance suggests that some melting/coalescence occurred compared to the conditions of the referred sample. The smaller grains have an average size of $\approx$ 51.8 and a distribution width of $\approx$ 24.2 nm (Figure 4.125).

The faceted grains suggest a zone 2 structure of Thornton's diagram, possibly starting to transit to zone 3 given the smoother appearance of the grains and coalescence of the smaller grains.

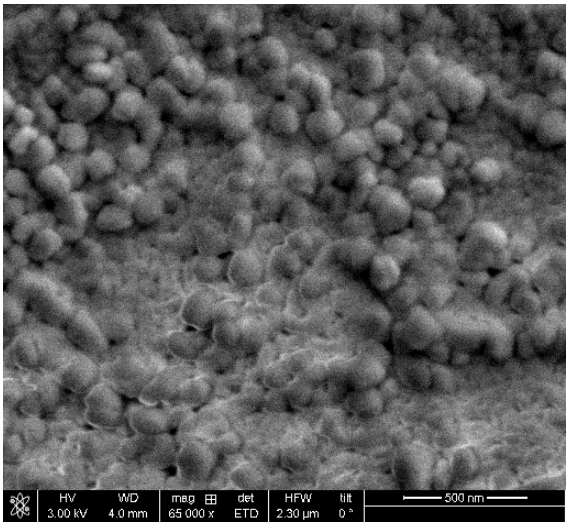

Figure 4.124: High magnification SEM image of the grains.

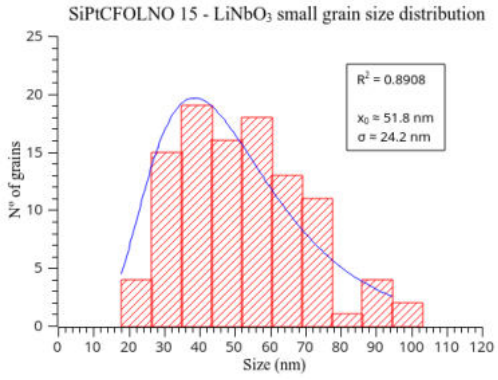

Figure 4.125: Size distribution of the LNO small grains.

Cross-section imaging (Figure 4.126) reveals a contrast difference at the base of the film's layer, suggesting the boundary between the $CoFe_2O_4$ and the $LiNbO_3$. At the left side of the image the film is not in contact with the substrate, likely a result of the process that induced the cracks observed at the surface. The film is dense and without pores. Non-parallel boundaries are identifiable, suggesting that the film's material was coalescing into large grains (Figure 4.127). This further reinforces that transition

to zone 3 of Thornton's diagram was taking place.

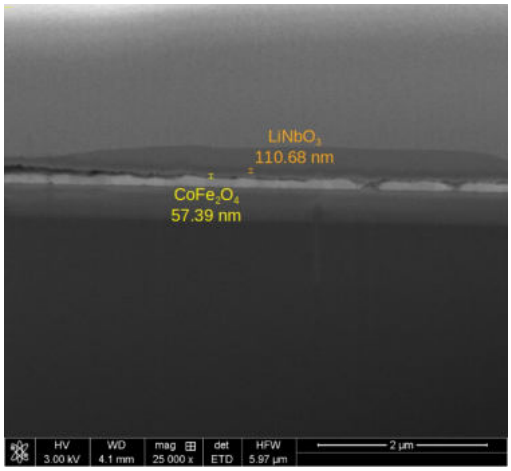

Figure 4.126: FIB-SEM image of the cross-section of the sample showing its different layers. Each film is indicated.

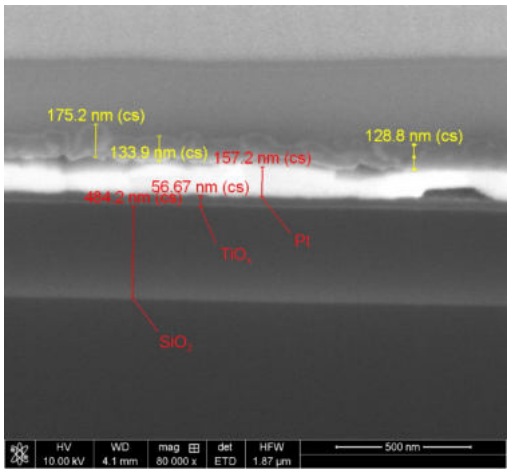

Figure 4.127: FIB-SEM higher magnification image of the cross-section with the layers' thicknesses. The film layer (CFO + LNO) measurements are presented in yellow.

Sample: SiPtCFOLNO 16

Substrate	Target	T(°C)	E(mJ)	f(Hz)	d_{target}(cm)	t_{dep}(min)	P_{dep}(mbar)
SiPt	CFO	650	350	10	5	30	0.1
	LNO			6	3	10	1

Table 33: Deposition conditions of sample SiPtCFOLNO 16.

Atomic %			
Co	Fe	Nb	Co/Fe ratio (approx.)
1.12	1.74	7.57	0.64
0.96	1.15	6.54	0.83
1.01	1.32	7.49	0.77
1.09	1.23	6.40	0.87
1.19	1.68	7.60	0.71

Table 34: Results of SEM-EDS analysis.

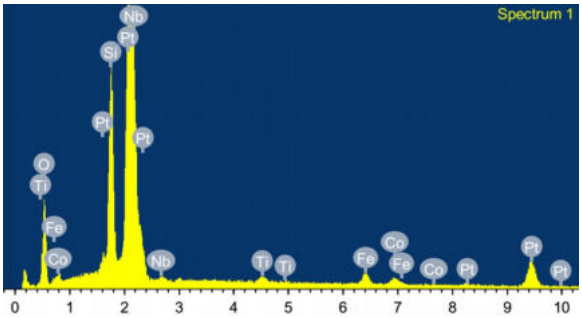

Figure 4.128: SEM-EDS spectrum of the sample's surface.

SEM-EDS analysis confirms the presence of all elements of interest (Figure 4.128). The Co/Fe ratios are somewhat higher than intended (Table 34) but this may reflect the small detected values.

The surface of the sample appears heterogeneous, with dark regions interspersed by brighter ones (Figure 4.129). Large, white dots are observed spread throughout it. The bright structure at the top-left of

Figure 4.129, on the top margin, is a contamination - possibly a piece of copper tape used for securing the sample onto the stub.

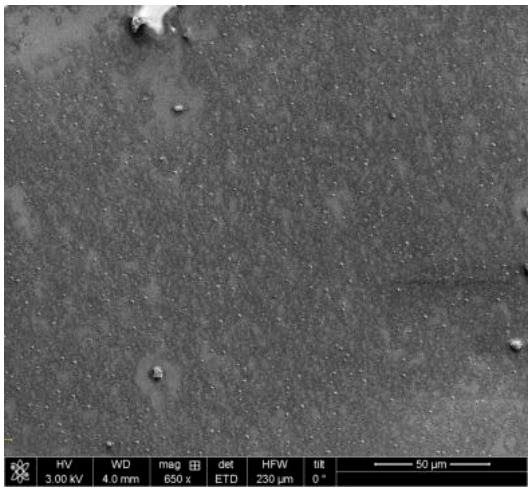

Figure 4.129: SEM image of the surface of the sample.

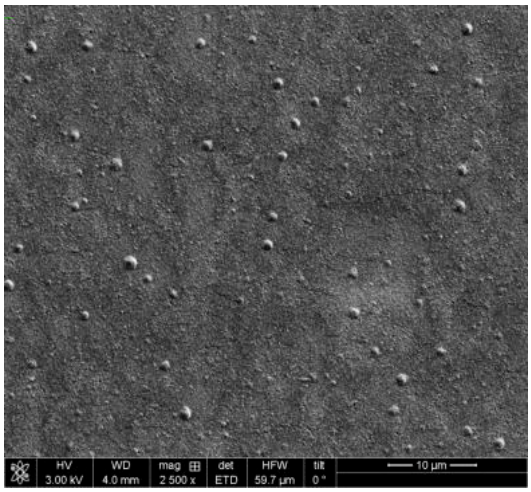

Figure 4.130: High magnification SEM image of the surface.

Closer inspection reveals a rough morphology (Figure 4.130). The large, white dots appear to be larger particulates of film that were deposited.

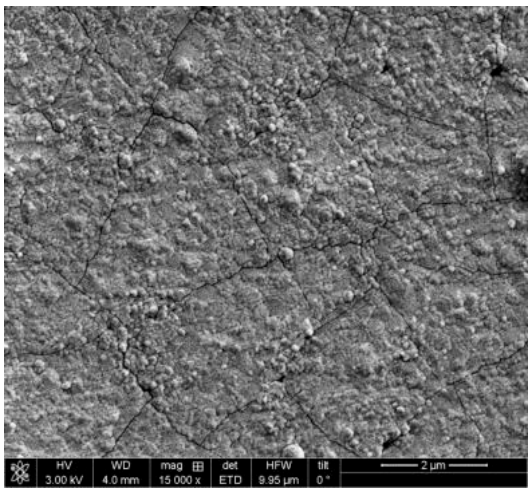

Figure 4.131: Higher magnification SEM image of the surface.

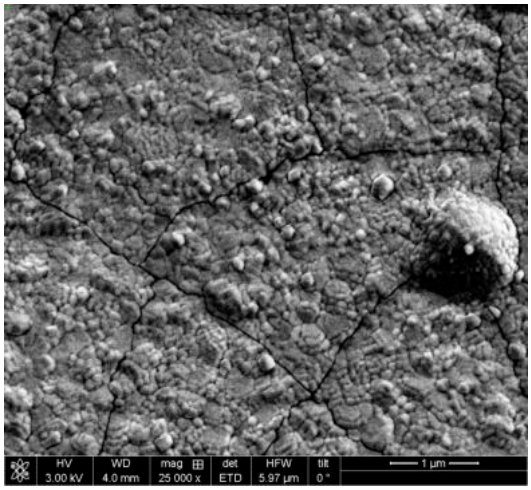

Figure 4.132: SEM image showing the individual grains that constitute the surface (LNO layer).

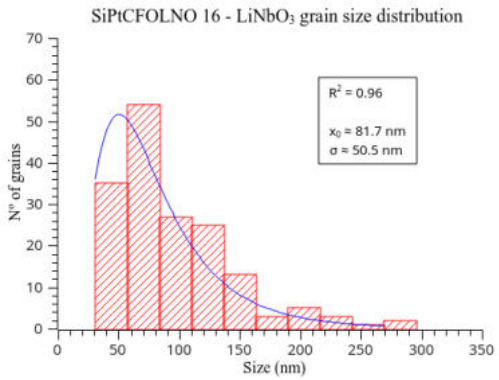

Figure 4.133: Size distribution of the LNO grains.

Figure 4.131 reveals that the sample's surface has fractures and is constituted by individual grains closely-packed together.

A high magnification image (Figure 4.132) shows that the grains (LNO) have an overall smooth appearance, but in some of them orientations characteristic of faceted grains (Figure 4.94) are recognizable. Coalescence has occurred, in some regions forming larger grains with a relatively smooth appearance. The large particulates observed in previous images are constituted by grains compacted together, as seen on the right side of the image. The average grain size is $\approx$ 81.7 with a distribution width of $\approx$ 50.5 nm (Figure 4.133).

The grain's morphology suggests a zone 2 structure of Thornton's diagram, possibly in transition to zone 3 given the coalescence and larger, smooth grains observed.

Figure 4.134 shows the sample's cross-section, revealing its different layers and respective thicknesses. The film's layer appears dense and with virtually no voids. The contrast difference observed close to the film's surface suggests the boundary between the CFO and LNO layers as indicated in the image.

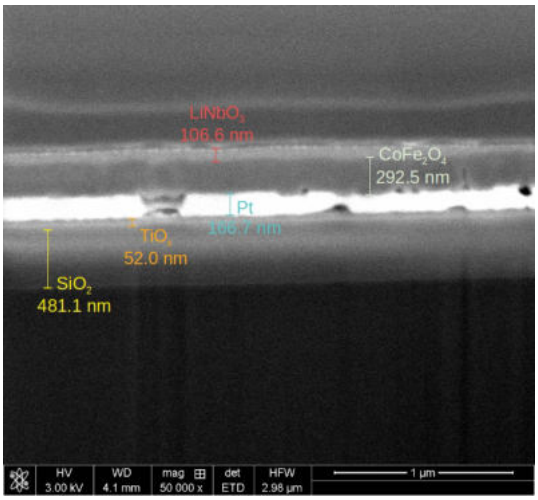

Figure 4.134: FIB-SEM image showing the cross-section of the sample.

Sample: SiPtCFOLNO 17

Substrate	Target	T(°C)	E(mJ)	f(Hz)	d_{target}(cm)	t_{dep}(min)	P_{dep}(mbar)
SiPt	CFO	650	350	10	5	75	0.1
	LNO			6	3	30	1

Table 35: Deposition conditions of sample SiPtCFOLNO 17.

Atomic %			
Co	Fe	Nb	Co/Fe ratio (approx.)
0.42	0.66	2.19	0.64
0.45	0.67	2.66	0.67
0.38	0.44	2.14	0.86
0.37	0.56	2.10	0.66

Table 36: Results of SEM-EDS analysis.

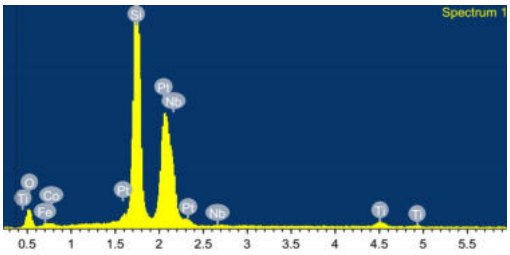

Figure 4.135: SEM-EDS spectrum of the sample's surface.

SEM-EDS analysis confirms the presence of all elements of interest (Figure 4.135). The Co/Fe ratios are somewhat above the intended proportions (Table 36) but one should take notice of their small percentage as compared to the rest of the sample, including the substrate.

The surface of the sample (LNO) layer (Figure 4.136) is constituted by individual grains interspersed by smoother regions. Pores are observed, as well as large, spherical domes, also constituted by the grains. They are larger particulates (droplets) that were deposited.

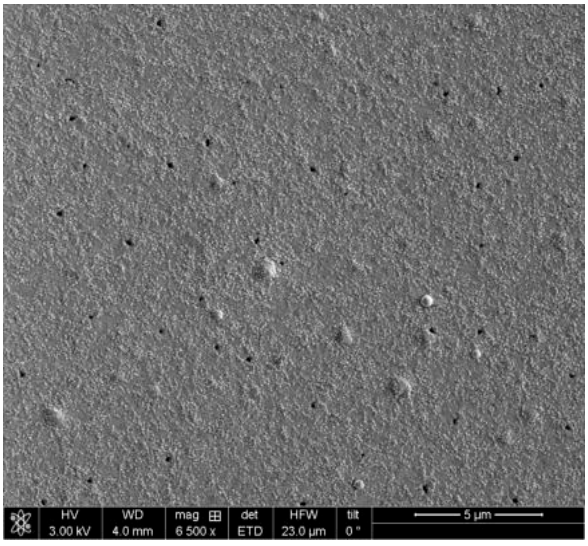

Figure 4.136: SEM image of the surface of the sample (LNO layer).

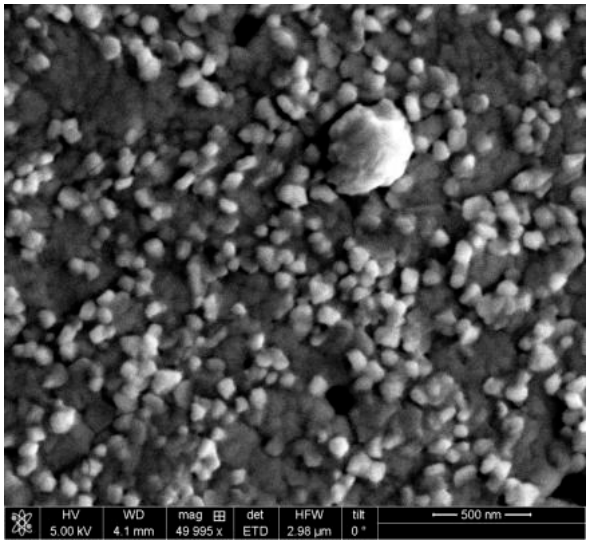

Figure 4.137: High magnification SEM image of the sample's surface.

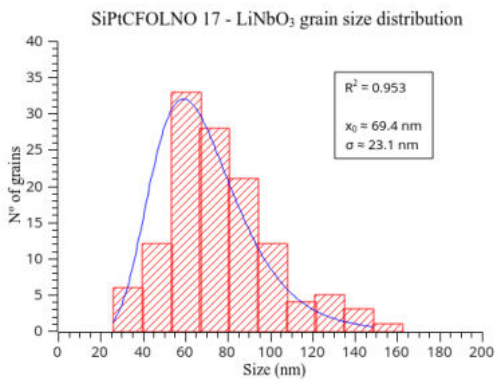

Figure 4.138: Size distribution of the LNO grains.

Closer inspection reveals that the grains appear to have faceted surfaces (Figure 4.137). The average grain size is $\approx$ 69.4 with a distribution width of $\approx$ 23.1 nm (Figure 4.138). The smoother regions between them are areas where coalescence occurred, originating a smoother and flatter surface. Larger and flatter grains can sometimes be identified in these regions (lower-left corner of Figure 4.137, for example), an indication of recrystallization.

The faceted grains indicate a zone 2 structure of Thornton's diagram. The observed coalescence and larger, smooth grains, as well as the dense film layer, suggest a possible transition to zone 3 taking place.

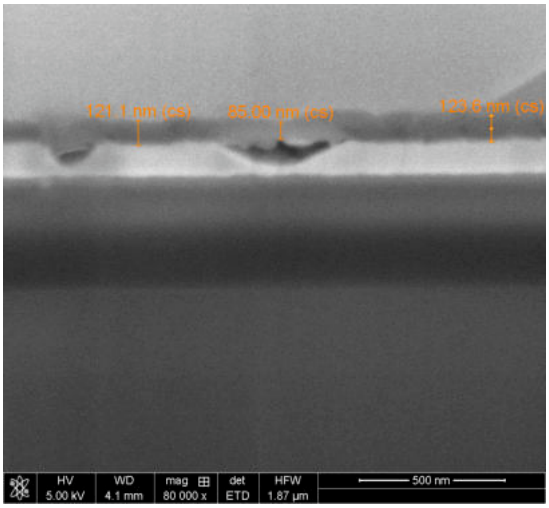

Figure 4.139: FIB-SEM image of the cross-section of the sample. The measured region is the film.

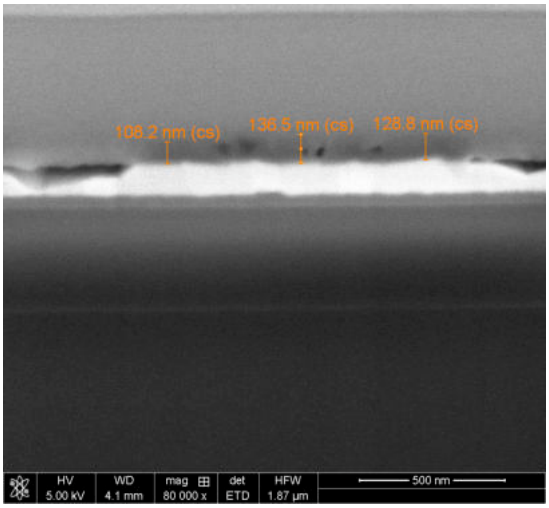

Figure 4.140: FIB-SEM image of another region of the film's layer.

Cross-section imaging of the sample reveals a dense film with no visible distinction between the CFO and LNO layers (Figure 4.139). The darker spots on the right side of the film, close to the Pt layer (brightest layer), are probably pores, given the similar aspect to those identified clearly in other region (Figure 4.140). However, few are present. Figure 4.141 shows a close-up of the film layer.

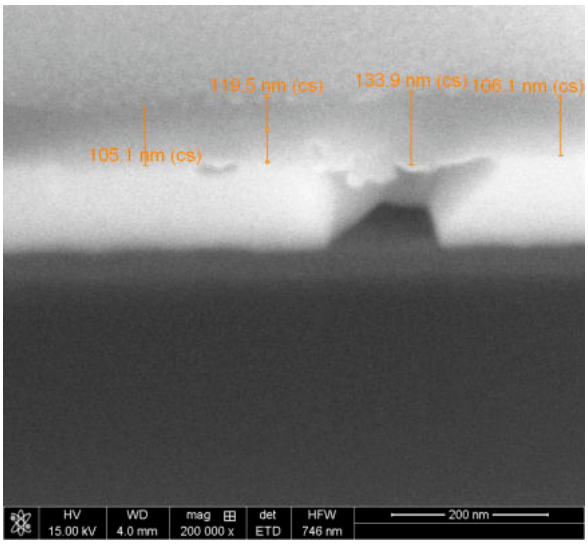

Figure 4.141: Higher magnification FIB-SEM image of the sample's cross-section with the film layer measurements.

Sample: SiPtCFOLNO 19

Substrate	Target	T(°C)	E(mJ)	f(Hz)	d_{target}(cm)	t_{dep}(min)	P_{dep}(mbar)
SiPt	CFO	650	350	10	5	60	0.1
	LNO			6	3	60	1

Table 37: Deposition conditions of the sample SiPtCFOLNO 19.

Atomic %		
Co	Fe	Ratio (approx.)
0.15	0.25	0.60
0.53	0.83	0.64
0.68	1.03	0.66
0.18	0.26	0.69

Table 38: Results of SEM-EDS analysis.

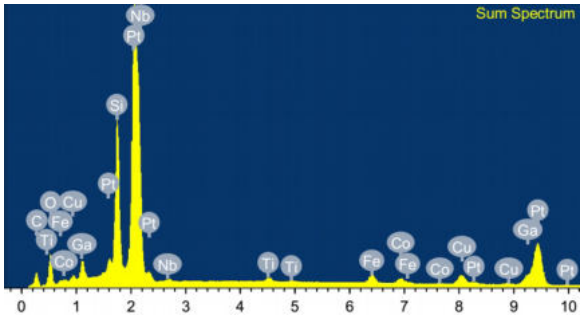

Figure 4.142: SEM-EDS spectrum of the sample's cross-section.

SEM-EDS analysis confirms the presence of all elements of interest (Figure 4.142). The Cu detected is from the lamella holder which is made of copper. The Co/Fe ratio is somewhat above the intended (Table 38).

The sample's surface (LNO layer) is constituted by grains which seem to have coalesced together to some extent (Figure 4.143). Some pores are present. On the top-right corner of the image, spherical domes made of grains are also observed. The average grain size is $\approx$ 178 with a distribution width of $\approx$ 67 nm (Figure 4.144).

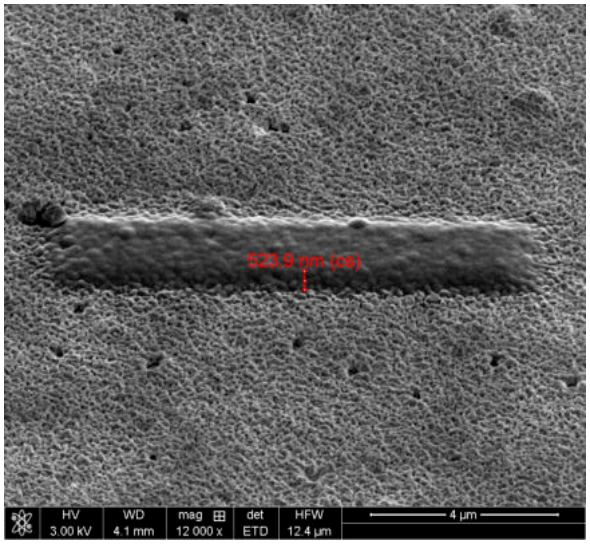

Figure 4.143: SEM image showing the surface of the sample, observed at a tilt of 52°. The protective Pt layer deposited and its height are shown as well.

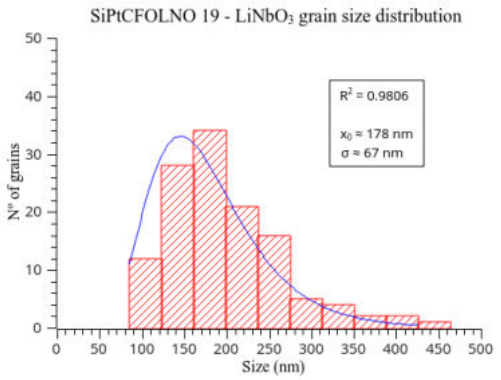

Figure 4.144: Size distribution of the LNO grains.

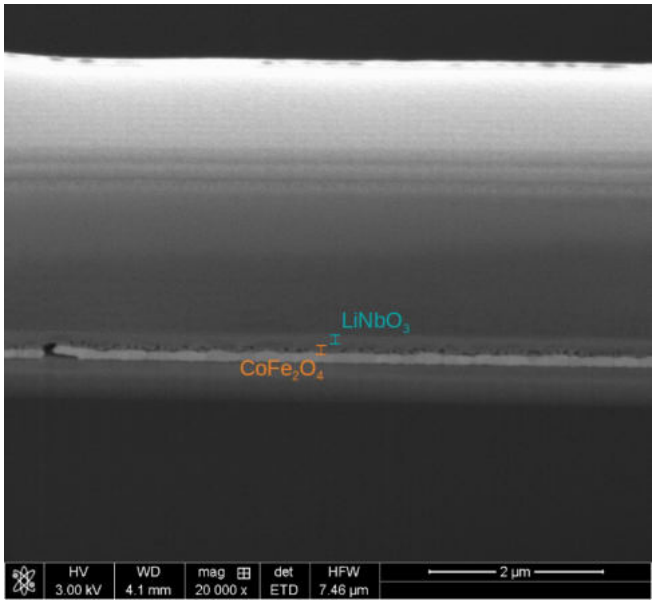

Figure 4.145: FIB-SEM image of the cross-section of the sample.

Figure 4.145 shows the cross-section of the sample. The contrast difference observed in the film layer suggests the boundary between the $CoFe_2O_4$ and $LiNbO_3$ layers as indicated. Some pores are present at the interface of the film with the substrate's Pt layer, but otherwise the film appears dense.

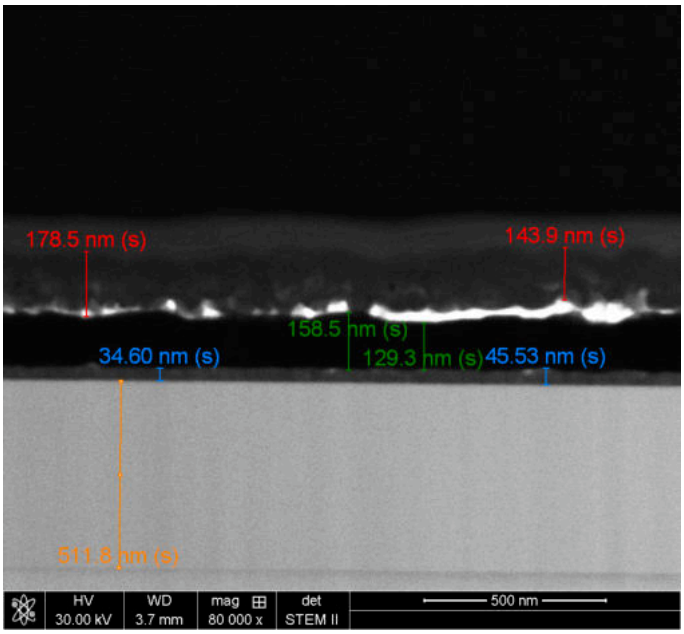

Figure 4.146: A lamella of the sample imaged in STEM mode, in bright-field (BF) mode. The thicknesses of the film (red), the substrate's Pt layer (green), the Ti layer (blue) and the SiO_2 layer (orange) are presented.

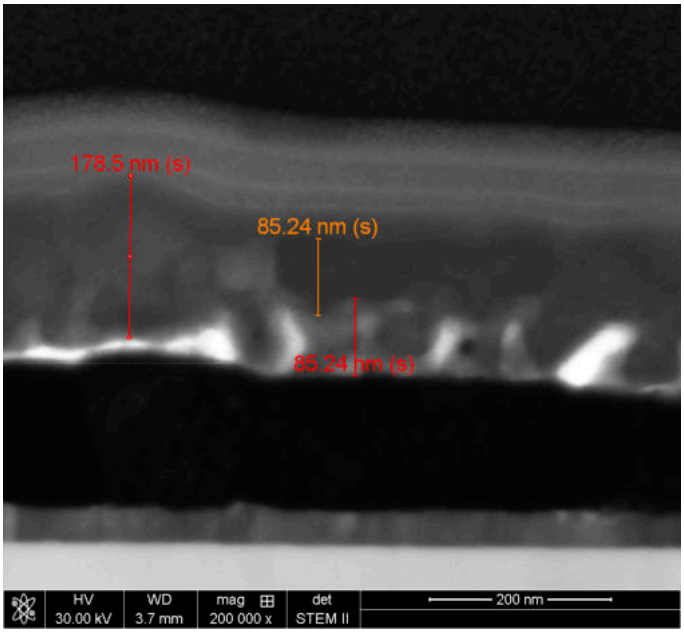

Figure 4.147: Close-up of the lamella in BF mode.

A lamella of the sample was prepared and imaged in STEM mode (Figure 4.146). The darker regions are made of heavier elements which scatter the electron beam more, thus appearing dark in BF mode. There is some contrast difference in some regions of the film due to the CFO/LNO atomic number difference. Tentative measurements of the CFO/LNO layers' thicknesses are shown in Figure 4.147.

Figure 4.148 shows another region of the lamella, revealing boundaries between grains, typical of zone 3 of Thornton's diagram. However, the surface morphology fits more adequately into zone 2, suggesting a transition between the two zones was taking place.

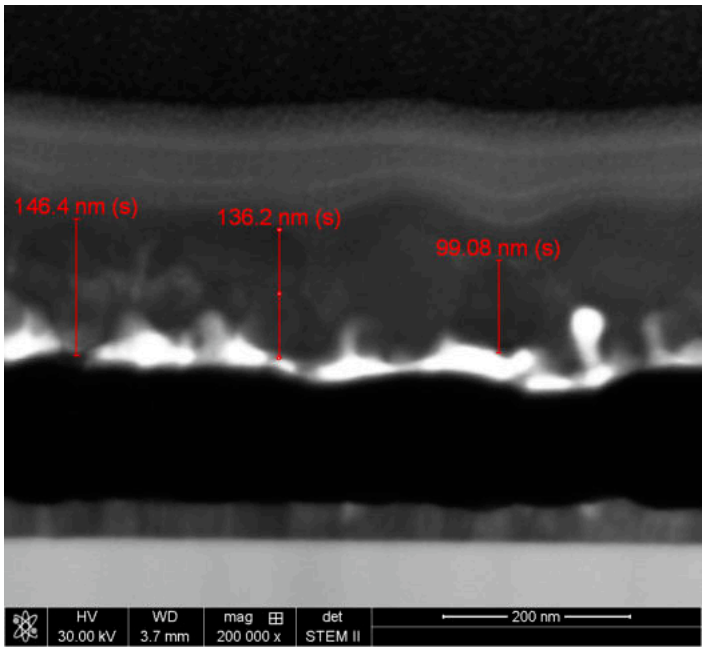

Figure 4.148: Another region of the lamella imaged in BF mode.

Sample: SiPtCFOLNO 22

Substrate	Target	T(°C)	E(mJ)	f(Hz)	d_{target}(cm)	t_{dep}(min)	P_{dep}(mbar)
SiPt	CFO	650	350	10	3.5	60	0.1
	LNO			6	3.1	60	1

Table 39: Deposition conditions of the sample SiPtCFOLNO 22.

This sample shows, compared with the previous one, the effect of reducing the CFO target-substrate distance to the value used in the first bi-layer sample, SiPtCFOLNO 2.

Atomic %			
Co	Fe	Nb	Co/Fe ratio (approx.)
0.94	1.28	0.64	0.73
1.17	1.57	0.88	0.75
1.28	1.66	1.13	0.77
1.05	1.31	0.72	0.80
1.00	1.30	0.75	0.79

Table 40: Results of SEM-EDS analysis.

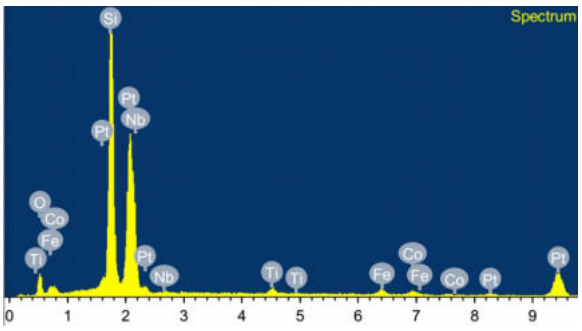

Figure 4.149: SEM-EDS spectrum of the sample's surface.

SEM-EDS analysis confirms the presence of all elements of interest (Figure 4.149). The Co/Fe ratios are higher than intended, however (Table 40).

The sample's surface (Figure 4.150) is very similar to that of Figure 4.66, with a grainy appearance and large particulates. The particulates' average size is ≈ 1194 with a distribution width of ≈ 1128 nm (Figure 4.151).

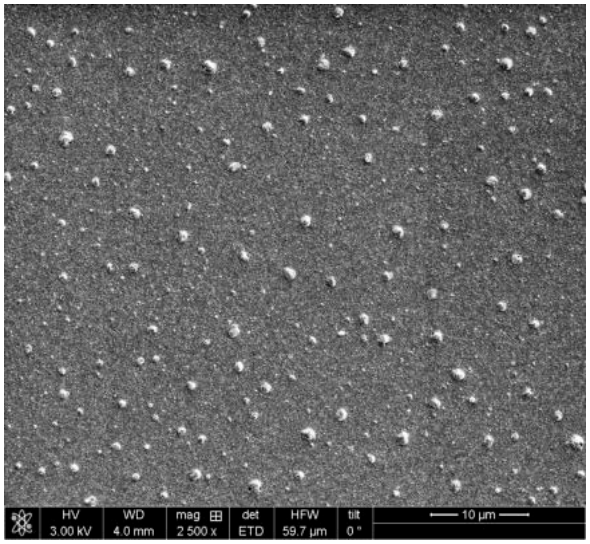

Figure 4.150: SEM image of the surface of the sample.

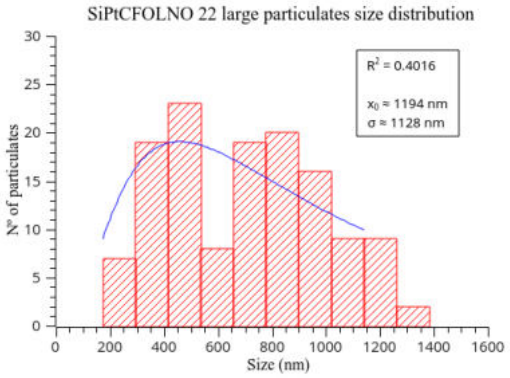

Figure 4.151: Size distribution of the large particulates.

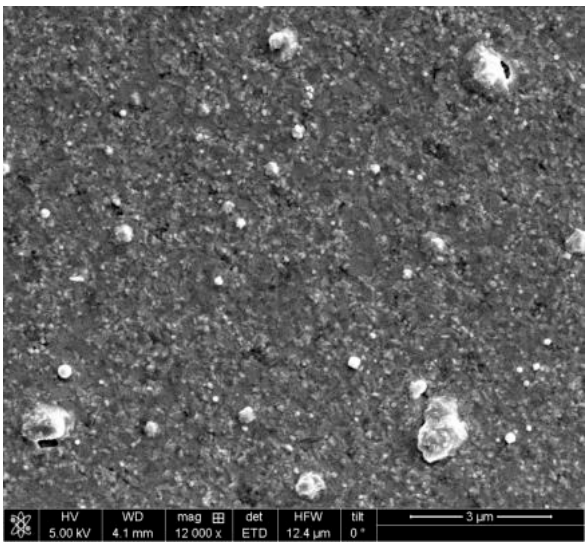

Figure 4.152: High magnification SEM image of the surface.

High magnification imaging (Figure 4.153) reveals a morphology identical to that of sample SiPtCFO 2, with faceted grains similar to shards. Both samples have the same CFO deposition conditions. The average grain size is ≈ 94.0 with a distribution width of ≈ 35.2 nm (Figure 4.154). Coalescence of the grains is observed in some regions, originating flatter and smoother surfaces. Some larger particulates (bright spheres at the left side of the image) are observed.

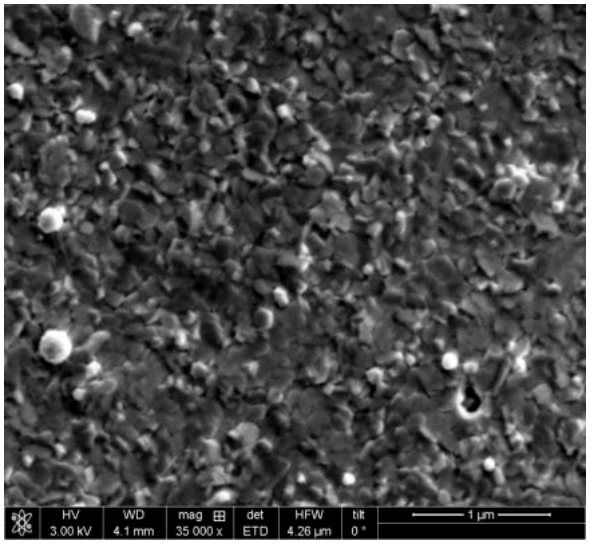

Figure 4.153: High magnification SEM image of the surface.

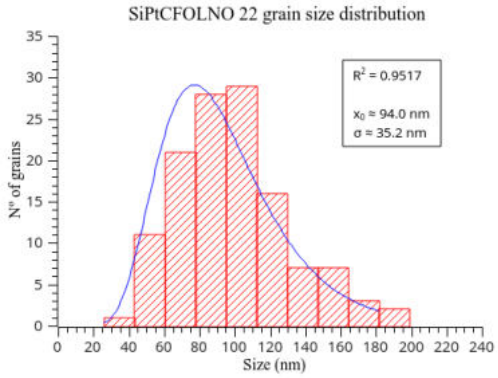

Figure 4.154: Grain size distribution of the sample.

Figure 4.155 shows an image of the surface taken at very low accelerating voltage. Compared with Figure 4.153, the surface appears smooth and no faceted grains are seen. Given that the $LiNbO_3$ is the top layer of the film, as well as the mentioned similarities with the sample SiPtCFO 2, it's possible that what was seen in the previous images was the CFO layer and the present image shows the LNO layer. It is also noteworthy that this layer must be very thin since it was visible only with an accelerating voltage of 1 kV. This hypothesis is further corroborated by the Nb relative abundance detected in the SEM-EDS analysis (Table 40). However, imaging of the cross-section would be necessary to confirm this.

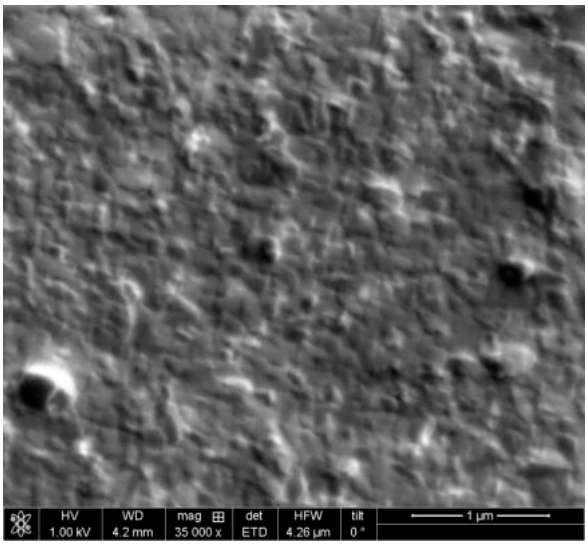

Figure 4.155: Very low accelerating voltage SEM image of the surface.

Given the faceted grains observed for the CFO layer, a zone 2 structure of Thornton's diagram seems to be the case, possibly in transition to zone 3 given the coalesced and smoother regions observed. For the LNO layer it's difficult to conclude which Thornton's diagram zone would be the most adequate.

4.1.4 Thornton's diagram zones of the studied samples

Table 41 and Table 42 compile, for each sample studied, the zones of Thornton's diagram into which they fit as well as their deposition temperature, pressure, target-substrate distance and deposition time. It is also indicated whether they were annealed or not in the case of room-temperature depositions.

Sample	T_{dep}(°C)	Annealed?	t_{dep} (min)	d_{target}(cm)	P_{dep}(mbar)	Thornton's diagram zone
SiLNO 6A	RT	Yes	20	3	1	1
SiLNO 5B	650	–	20	3	0	2
SiLNO 9A	RT	No	20	3	0.1	1, possibly T
SiLNO 10A	RT	No	20	3	0.01	1, possibly T
SiLNO 10B		Yes		3	0.01	2 in transition to 3
SiLNO 11A	RT	No	20	7	0.01	1, possibly T
SiLNO 11B		Yes		7	0.01	1 with recrystallized grains
SiLNO 12A	RT	No	20	2	0.1	1
SiLNO 12B		Yes		2	0.1	1 with some coalescence
SiPtLNO 4B	650	–	60	3	1	2 in transition to 3
SiPtCFO 2	650	–	60	3.5	0.1	2, maybe in transition to 3

Table 41: Observed Thornton's diagram zones for the LNO and CFO films studied.

Sample	T_{dep}(°C)	Layer	t_{dep} (min)	d_{target}(cm)	P_{dep}(mbar)	Thornton's diagram zone
SiPtCFOLNO 2	650	CFO	45	5	0.1	2
		LNO	30	3	1	2
SiPtCFOLNO 6	650	CFO	60	5	0.1	Not possible to say
		LNO	45	3	1	2
SiPtCFOLNO 8	650	CFO	60	5	0.1	Not possible to say
		LNO	75	3	1	2, maybe in progress to 3
SiPtCFOLNO 9	650	CFO	60	5	0.1	Not possible to say
		LNO	75	3	1	1, maybe in progress to T
SiPtCFOLNO 10	650	CFO	75	5	0.1	Not possible to say
		LNO	30	3	1	T
SiPtCFOLNO 15	650	CFO	20	5	0.1	2 in progress to 3
		LNO	10	3	1	2 in progress to 3
SiPtCFOLNO 16	650	CFO	30	5	0.1	2 in progress to 3
		LNO	10	3	1	2 in progress to 3
SiPtCFOLNO 17	650	CFO	75	5	0.1	2 in progress to 3
		LNO	30	3	1	2 in progress to 3
SiPtCFOLNO 19	650	CFO	60	5	0.1	2 in progress to 3
		LNO	60	3	1	2 in progress to 3
SiPtCFOLNO 22	650	CFO	60	3.5	0.1	2 in progress to 3
		LNO	60	3.1	1	Not possible to say

Table 42: Observed Thornton's diagram zones for the CFO-LNO films studied.

In some of the CFO-LNO samples it was not possible to check to which Thornton's diagram zone the CFO layer belonged. However, it should be safe to assume that they belong to the same zone as the corresponding LNO film.

4.2 Application of the pressure-distance scaling law

To apply the pressure-distance (P-D) scaling law to the systems studied, the best films should be considered, with the concept of "best" depending on the applications envisaged or desired physical properties. In the present study this would mean dense films, ideally without pores, and with the appropriate stoichiometry. However, some flexibility in regards to stoichiometry should be considered, due to the fact that EDS is more appropriate for qualitative rather than quantitative information. In terms of TD zones, films from zones 2 and 3 would be the most desirable. Using the pressure and distance of the samples displaying these properties, a fit of the P-D scaling law with Equation 2.11 can then be obtained.

4.2.1 Single-layer LNO films

Of the LNO single-layer samples observed, those falling in zone 2 or 3 of TD are samples SiLNO 5B, SiLNO 10B - the annealed version of sample SiLNO 10A and SiPtLNO 4B.

Sample SiLNO 10B acquired the observed morphology due to the annealing procedure, as can be confirmed by comparison with its non-annealed counterpart, sample SiLNO 10A. Given that its morphology isn't a result of the deposition process, it cannot be used with the P-D model.

This leaves sample SiPtLNO 4B, which displays a dense morphology. No stoichiometric information on it is available but given the presence of the desired elements it will be considered for this analysis.

The pressure and target-substrate distance values for this sample are $P = 1$ mbar and $d_{target} = D = 3$ cm. This pressure is high compared to the value under which Equation 2.9 was applied in other studies[8], so the value $n = 0.4$ of the original blast wave model would be appropriate in Equation 2.11. The P-D scaling law for this case would then be:

$$PD^3 = 27 \text{ mbar cm}^3 \tag{4.1}$$

which may also be written as[23]:

$$P_{mbar} = \frac{27}{D^3_{optimal}} \quad \text{at} \quad T = 650 \text{ °C} \tag{4.2}$$

where P_{mbar} is the pressure in mbar and $D_{optimal}$ is the optimal target-substrate distance.

Regarding the samples deposited at room temperature and not annealed, despite not displaying the

intended morphology, applying the P-D scaling law is informative. Sample SiLNO 12A was selected for this. It was deposited using $P = 0.1$ mbar and $d_{target} = D = 2$ cm. By the aforementioned argument, a value of $n = 0.4$ would be appropriate in this case as well, yielding the P-D scaling law:

$$PD^3 = 0.8 \text{ mbar cm}^3 \Rightarrow P_{mbar} = \frac{0.8}{D^3_{optimal}} \quad \text{at} \quad T = RT \tag{4.3}$$

Equation 4.2 and Equation 4.3 are represented in Figure 4.156.

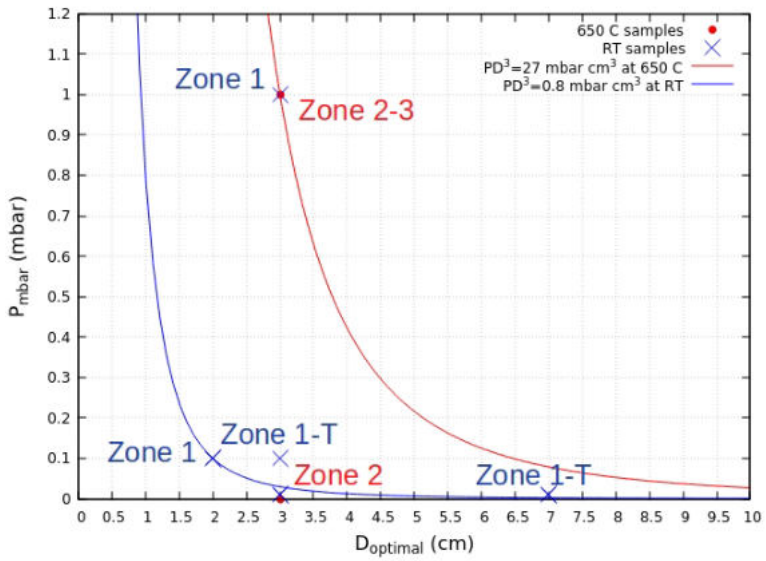

Figure 4.156: P-D scaling law obtained for single-layer LNO films at the temperatures indicated. The Thornton's diagram zones observed for samples deposited at both temperatures are indicated as well.

The samples represented in red in Figure 4.156 are SiPtLNO 4B and SiLNO 5B, both deposited under the same conditions except for pressure and deposition time. The deposition time will influence the film's thickness; the difference in pressure, however, allows the draft of a phase diagram for the different Thornton's diagram zones at each temperature, as represented in Figure 4.156. It should be noted that the substrates are different - sample SiPtLNO 4B has a SiPt substrate while sample SiLNO 5B has a Si one. The samples represented in blue are SiLNO 12A, SiLNO 9A, SiLNO 10A and SiLNO 11A.

It is observed that at room temperature, the represented samples display a zone 1 structure despite the reduced target-substrate distances used. To achieve a zone 2 or 3 microstructure smaller distances and/or lower pressures would be needed, that is, the diagram moves left. However, such reduced distances (less than 2 cm) are not possible with the laboratory's equipment but they also aren't advisable, as such values increase the chance of the film being resputtered due to the plume's constituents having high kinetic energy at low distance to target. This also alters the stoichiometry. Increasing the deposition temperature provides a zone 2 (in progress to 3) microstructure for the same P and D values, confirming the critical role of the temperature.

4.2.2 CFO films

Regarding the CFO films deposited, one was a single-layer film (SiPtCFO 2) and the remaining constituted one of the layers of the bi-layer films. The vast majority of the CFO films was observed to belong to zone 2 of Thornton's diagram, but in the some of the bi-layer samples it wasn't possible to verify into which zone they fit (Table 42). However, as mentioned before, it should be safe to assume that they belong to the same zone as the corresponding sample's LNO layer, due to the uniformity observed in the cross-section images. Furthermore, the CFO layer functioned as a nucleation layer for the LNO and the morphology of the growth surface influences the structure of the growing film[9], being reproduced at the film's surface[39]. So it should have a structure similar to that observed in the LNO. This places the vast majority of the CFO layers belonging to bi-layer samples in the zone 2 of Thornton's diagram. With this in mind and attending to the Co/Fe ratios observed, sample SiPtCFOLNO 15 was deemed adequate to be used in the pressure-distance scaling law.

The CFO layer in this sample was deposited with $P = 0.1$ mbar and $d_{target} = D = 5$ cm. Based on the argument mentioned above, a value of $n = 0.4$ of the original blast wave model would be appropriate in this case as well, yielding the P-D scaling law:

$$PD^3 = 12.5 \text{ mbar cm}^3 \Rightarrow P_{mbar} = \frac{12.5}{D^3_{optimal}} \quad \text{at} \quad T = 650 \text{ °C} \tag{4.4}$$

Equation 4.4 is represented in Figure 4.157.

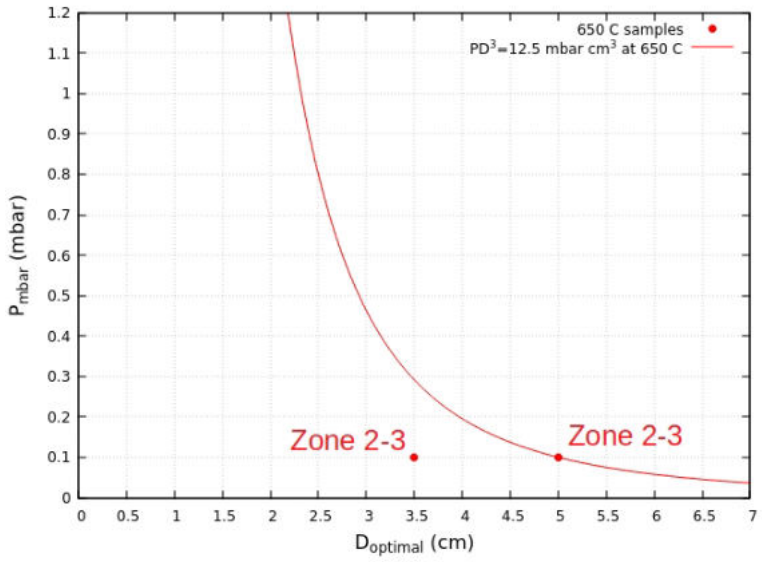

Figure 4.157: P-D scaling law obtained for the CFO layer at the temperature indicated. The Thornton's diagram zones observed for this layer in other samples (both single film and bi-layer film) are also represented.

4.3 Effect of the deposition time

The deposition time will affect the deposited film in different ways. Maintaining all other deposition parameters constant (temperature, target-substrate distance, pressure), it is expected that the films become thicker with longer deposition times. Figure 4.158 shows, for the CFO-LNO samples studied, the influence of the total deposition time (t_{dep}(CFO) + t_{dep}(LNO)) on the total film thickness (CFO layer + LNO layer). Overall, the film thickness increases with the deposition time, as expected. The deviations from this tendency may be due to observation of the film in a region where the thickness wasn't maximal, as illustrated previously in Figure 4.106.

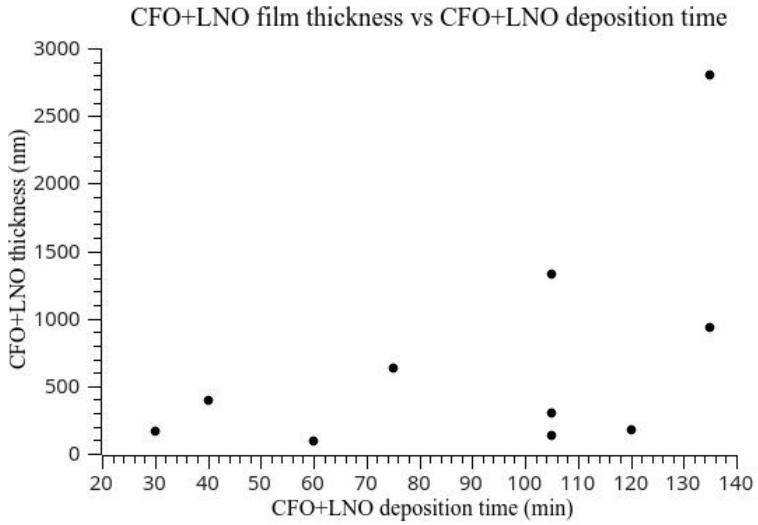

Figure 4.158: Variation of the total film thickness (CFO layer + LNO layer) with the total deposition time (t_{dep}(CFO) + t_{dep}(LNO)).

The film's crystallinity may also be affected, due to changes in the growth mechanism induced by different exposures times to the oxygen atmosphere[56] and high temperatures. If there are mechanical stresses present, longer deposition times translate to stress relaxation, which may also affect the resulting crystal structure. Longer deposition times were found to increase the average crystallite size and to promote recrystallization, reflected by stronger peak intensity in X-ray diffraction patterns[56].

The average grain size is also expected to increase with the deposition time[56]. This tendency was observed in the LNO surface grains of the different samples (Figure 4.159).

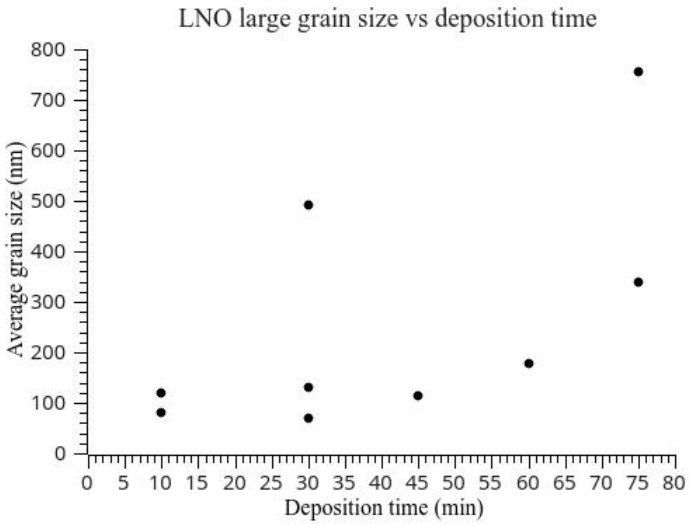

Figure 4.159: Variation of the LNO large grain size with the deposition time. An increasing tendency is visible.

The increase in crystallite and grain size is induced by longer exposure to the deposition temperature, which provides energy for surface and bulk diffusion. However, as the film grows and the distance between the deposition surface and the substrate increases, the effect of the substrate/film interfacial mechanical interaction reduces, due to strain relaxation, and the mechanical energy is minimized by the appearance of stacking faults or defects in the films. This will eventually promote a zone 1 or T structure of Thornton's diagram due to lack of energy for efficient surface diffusion, an effect observed in samples SiPtCFOLNO 9 and 10. These samples' deposition times were some of the longest used, 135 and 105 minutes respectively. Surface and cross-section images of them are shown in Figure 4.160 to Figure 4.163. This observation indicates that there is an optimal deposition time, striking a balance between increased crystallinity, grain size and recrystallization, but without reaching a film thickness where the film structure relaxation occurs and the nanoscale effects disappear. According to the SEM images of the different samples and the EDS elemental ratios, it is observed that sample SiPtCFOLNO 15 displays a dense film, relatively smooth surface with coalescence between the grains observed and an EDS ratio close to the intended. This suggests that a total deposition time of $\approx$ 30 min, in particular $\approx$ 20 min for the CFO and $\approx$ 10 min for the LNO, may suffice for obtaining a good film.

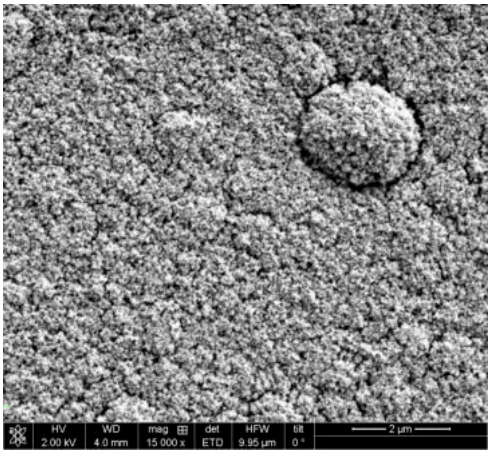

Figure 4.160: Grainy surface of sample SiPtC-FOLNO 9. The total deposition time was 135 minutes.

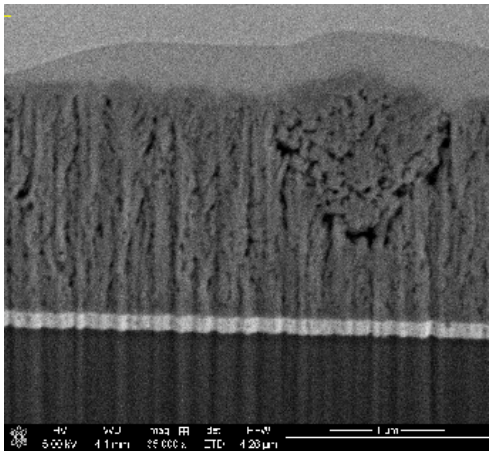

Figure 4.161: Cross-section of sample SiPtC-FOLNO 9.

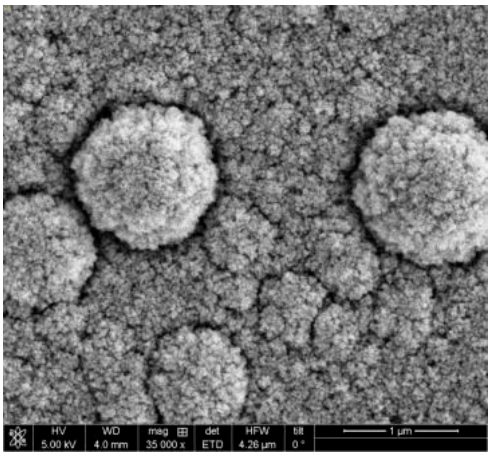

Figure 4.162: Grainy surface of sample SiPtC-FOLNO 10. The total deposition time was 105 minutes.

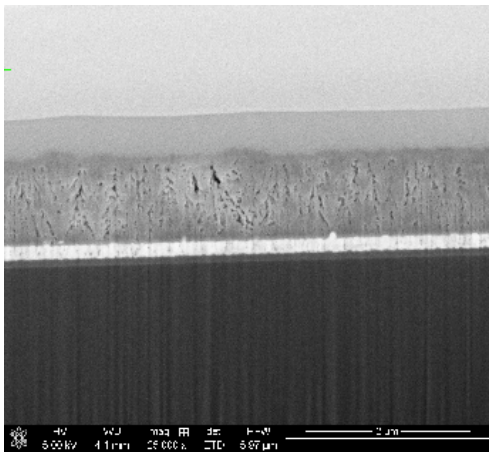

Figure 4.163: Cross-section of sample SiPtC-FOLNO 10.

5 Conclusions and suggestions of future works

In the present work, $LiNbO_3$ (LNO) thin films and bi-layer $LiNbO_3/CoFe_2O_4$ (CFO-LNO) thin films were deposited on Si and Si with a Pt layer (SiPt) substrates by pulsed laser ablation, using different deposition conditions. The target-substrate distance D and background gas pressure P were varied, as well as the deposition time. The film's microstructure and surface morphology were studied by scanning electron microscopy and focused ion beam techniques, allowing the classification of the different samples according to the zone structure model proposed by Thornton[10]. Attending to the dynamics of the ablation plume expansion in a background gas, a blast wave model was be used[8] to obtain a scaling relationship between the background gas pressure and the target-substrate distance[22] (P-D scaling law). Considering the film properties of interest, this P-D scaling law was be applied to films belonging to the desired zone of Thornton's diagram. This allowed the construction of a phase diagram for the materials deposited, revealing what zone structure of Thornton's diagram will be obtained for given values of background gas pressure and target-substrate distance.

It was observed that films deposited at room temperature developed a porous microstructure, typical of zone 1 and zone T of Thornton's diagram. Varying the target-substrate distance or the pressure had no impact, attesting to the need of appropriate substrate temperatures during the deposition. This was further corroborated by the results of a post-deposition annealing procedure, which resulted in grain coalescence and in transition to a zone 2/3 structure. The films deposited at higher temperature (650 °C) consistently display a zone 2 structure, often with indications of transition to zone 3 in progress. The CFO-LNO films analysed with X-ray diffraction reveal a rhombohedral crystal structure for the LNO and cubic structure for the CFO.[15]

The phase diagrams resulting from the application of the P-D scaling law to the LNO film layer indicate that, for room temperature depositions, extremely small target-substrate distances ($\lesssim 2$ cm) and very low pressures would be needed to achieve a zone 2-3 film structure. These distance values, however, are not advisable due to the plume's constituents not having enough time to thermalize, increasing the chances of resputtering the already deposited film. Furthermore, the reduced pressures necessary wouldn't provide an adequate film stoichiometry, as proved by the EDS elemental ratios observed in samples SiLNO 10A (deposited with $P = 0.01$ mbar) and SiLNO 12A/B (deposited with $P = 0.1$ mbar). For depositions at 650 °C, a zone 2-3 structure is obtained for the values of P and D used in room temperature depositions, further reinforcing the deposition temperature's relevance.

For the CFO film layer, the phase diagram indicates that a zone 2-3 structure persists to D values as low as 3,5 cm, indicating that to achieve a zone 3 structure the lowest target-substrate distances capable by the experimental apparatus would have to be used. Eventually, reducing the pressure while maintaining this distance could achieve the same result but this would need to be tested.

The effect of the total deposition time (the sum of the CFO and LNO deposition times) for a given target-substrate distance and background gas pressure was also studied. It was observed that both the total film

thickness and the grain size increased with deposition time. However, it was also observed that for very long deposition times the film's microstructure becomes typical of zone 1/T of Thornton's diagram. This occurs because as the film's thickness increases, the energy provided by the deposition temperature is increasingly absorbed in the film's bulk and surface diffusion becomes more difficult, eventually inducing a zone 1/T growth mode. This indicates that there is an optimal deposition time which enables increased film crystallinity, grain size and recrystallization but without diminishing surface diffusion to the point of inducing a porous growth mode. Observation of the deposited films' density, surface morphology and EDS elemental ratio suggests a value of approximately 30 minutes as providing these characteristics.

It would be interesting to perform more depositions with more combinations of P and D values at 650 °C. This would expand the phase diagrams obtained through the P-D scaling law and allow a more precise determination of where the boundaries between Thornton's diagram zones are. Regarding the distinction between the two film layers in the CFO-LNO samples, preparing a lamella at the FIB and observing it using transmission electron microscopy would allow the precise determination of the boundary between the films.

Regarding the effect of the deposition time, considering the optimal value suggested, it could be interesting to perform depositions with the total time between 20 and 30 minutes, in order to determine the minimum value necessary to obtain films with the desired characteristics.

References

[1] Lane W Martin and Andrew M Rappe. Thin-film ferroelectric materials and their applications. Nature Reviews Materials, 2(2):1–14, 2016.

[2] LW Martin, SP Crane, YH Chu, MB Holcomb, M Gajek, Mark Huijben, Chan-Ho Yang, N Balke, and R Ramesh. Multiferroics and magnetoelectrics: thin films and nanostructures. Journal of Physics: Condensed Matter, 20(43):434220, 2008.

[3] J.M.G.C.A. Barbosa. Nano-estruturas compósitas multiferróicas. PhD thesis, Universidade do Minho, 2013.

[4] Li Gui. Periodically poled ridge waveguides and photonic wires in linbo3 for efficient nonlinear interactions. University of Paderborn, 2010.

[5] R Sato Turtelli, M Kriegisch, M Atif, and R Grössinger. Co-ferrite–a material with interesting magnetic properties. In IOP Conference Series: Materials Science and Engineering, volume 60, page 012020. IOP Publishing, 2014.

[6] Michael NR Ashfold, Frederik Claeyssens, Gareth M Fuge, and Simon J Henley. Pulsed laser ablation and deposition of thin films. Chemical Society Reviews, 33(1):23–31, 2004.

[7] LW Martin, Y-H Chu, and RJMS Ramesh. Advances in the growth and characterization of magnetic, ferroelectric, and multiferroic oxide thin films. Materials Science and Engineering: R: Reports, 68(4-6):89–133, 2010.

[8] David B Geohegan. Fast intensified-ccd photography of yba2cu3o7- x laser ablation in vacuum and ambient oxygen. Applied physics letters, 60(22):2732–2734, 1992.

[9] Norbert Kaiser. Review of the fundamentals of thin-film growth. Applied optics, 41(16):3053–3060, 2002.

[10] John A Thornton. Influence of apparatus geometry and deposition conditions on the structure and topography of thick sputtered coatings. Journal of Vacuum Science and Technology, 11(4):666–670, 1974.

[11] EAG Laboratories Ltd. Auger Electron Sprectroscopy AES Services. https://www.eag.com/resources/appnotes/auger-electron-spectroscopy-aes-services/. Accessed: 2021-06-19.

[12] H Seiler. Secondary electron emission in the scanning electron microscope. Journal of Applied Physics, 54(11):R1–R18, 1983.

[13] Bob Hafner. Scanning electron microscopy primer. Characterization Facility, University of Minnesota-Twin Cities, pages 1–29, 2007.

[14] Joseph I Goldstein, Dale E Newbury, Joseph R Michael, Nicholas WM Ritchie, John Henry J Scott, and David C Joy. Scanning electron microscopy and X-ray microanalysis. Springer, 2017.

[15] Bruna Machado da Silva. Nanoestruturas compósitas magnéticas por ablação laser. Master's thesis, Universidade do Minho, Escola de Ciências, 2019.

[16] John A Thornton. Structure-zone models of thin films. In Modeling of Optical Thin Films, volume 821, pages 95–105. International Society for Optics and Photonics, 1988.

[17] Karl-Heinz Müller. Dependence of thin-film microstructure on deposition rate by means of a computer simulation. Journal of applied physics, 58(7):2573–2576, 1985.

[18] L Zhou, YP Wang, ZG Liu, WQ Zou, and YW Du. Structure and ferroelectric properties of ferroelectromagnetic ymno3 thin films prepared by pulsed laser depositon. physica status solidi (a), 201(3):497–501, 2004.

[19] BA Movchan and AV Demchishin. Structure and properties of thick condensates of nickel, titanium, tungsten, aluminum oxides, and zirconium dioxide in vacuum. Fiz. Metal. Metalloved. 28: 653-60 (Oct 1969)., 1969.

[20] Russell Messier. Toward quantification of thin film morphology. Journal of Vacuum Science & Technology A: Vacuum, Surfaces, and Films, 4(3):490–495, 1986.

[21] CRM Grovenor, HTG Hentzell, and DA Smith. The development of grain structure during growth of metallic films. Acta Metallurgica, 32(5):773–781, 1984.

[22] HS Kim and Hoi Sing Kwok. Correlation between target-substrate distance and oxygen pressure in pulsed laser deposition of yba2cu3o7. Applied physics letters, 61(18):2234–2236, 1992.

[23] M Koubaa, AM Haghiri-Gosnet, R Desfeux, Ph Lecoeur, W Prellier, and B Mercey. Crystallinity, surface morphology, and magnetic properties of la 0.7 sr 0.3 mno 3 thin films: an approach based on the laser ablation plume range models. Journal of applied physics, 93(9):5227–5235, 2003.

[24] Wilma Eerenstein, ND Mathur, and James F Scott. Multiferroic and magnetoelectric materials. nature, 442(7104):759–765, 2006.

[25] Crystal Technology Inc. Lithium niobate/lithium tantalate acoustic crystals. https://web.archive.org/web/20061016052556/http://www.crystaltechnology.com/docs/LN_LTAppNote.pdf. Accessed: 2021-07-23.

[26] RS Weis and TK Gaylord. Lithium niobate: summary of physical properties and crystal structure. Applied Physics A, 37(4):191–203, 1985.

[27] A Franco Jr and FC e Silva. High temperature magnetic properties of cobalt ferrite nanoparticles. Applied Physics Letters, 96(17):172505, 2010.

[28] J Barbosa, BG Almeida, JA Mendes, AG Rolo, JP Araújo, and JB Sousa. Nanogranular ba ti o 3–co fe 2 o 4 thin films deposited by pulsed laser ablation. Journal of applied physics, 101(9):09M101, 2007.

[29] A Ferretti, RJ Arnott, E Delaney, and A Wold. Cobalt ferrite single crystals. Journal of Applied Physics, 32(5):905–905, 1961.

[30] GR Fox, S Trolier-McKinstry, SB Krupanidhi, and LM Casas. Pt/ti/sio2/si substrates. Journal of materials research, 10(6):1508–1515, 1995.

[31] P Muralt. Ferroelectric thin films for micro-sensors and actuators: a review. Journal of micromechanics and microengineering, 10(2):136, 2000.

[32] Roger Kelly, Antonio Miotello, Bodil Braren, Arunava Gupta, and Kelly Casey. Primary and secondary mechanisms in laser-pulse sputtering. Nuclear Instruments and Methods in Physics Research Section B: Beam Interactions with Materials and Atoms, 65(1-4):187–199, 1992.

[33] Milton Ohring. Materials science of thin films. Elsevier, 2001.

[34] TJ Jackson and SB Palmer. Oxide superconductor and magnetic metal thin film deposition by pulsed laser ablation: a review. Journal of Physics D: Applied Physics, 27(8):1581, 1994.

[35] Tiago Rebelo, João Alves, and Bernardo Almeida. Simulation of the temperature profile of bacazrtio3 thin films during laser annealing. In EPJ Web of Conferences, volume 233, page 05008. EDP Sciences, 2020.

[36] Jørgen Schou, Salvatore Amoruso, and James G Lunney. Plume dynamics. In Laser Ablation and its Applications, pages 67–95. Springer, 2007.

[37] Donald L. Smith. Thin-film deposition: principles and practice. McGraw-Hill, Inc., 1995.

[38] Ya B Zel'Dovich and Yu P Raizer. Physics of shock waves and high-temperature hydrodynamic phenomena. Courier Corporation, 2002.

[39] John A Thornton. High rate thick film growth. Annual review of materials science, 7(1):239–260, 1977.

[40] John A Thornton. The microstructure of sputter-deposited coatings. Journal of Vacuum Science & Technology A: Vacuum, Surfaces, and Films, 4(6):3059–3065, 1986.

[41] G Cristoforetti, G Lorenzetti, PA Benedetti, E Tognoni, S Legnaioli, and V Palleschi. Effect of laser parameters on plasma shielding in single and double pulse configurations during the ablation of an aluminium target. Journal of Physics D: Applied Physics, 42(22):225207, 2009.

[42] David W Gregg and Scott J Thomas. Momentum transfer produced by focused laser giant pulses. Journal of Applied Physics, 37(7):2787–2789, 1966.

[43] Christof W Schneider and Thomas Lippert. Laser ablation and thin film deposition. In Laser processing of materials, pages 89–112. Springer, 2010.

[44] Coherent Inc. LPXpro series data sheet. https://content.coherent.com/legacy-assets/pdf/LPXpro-Series-Data-Sheet.pdf. Accessed: 2021-05-30.

[45] SG Lipson, H Lipson, and DS Tannhauser. Optical Physics, ed. Cambridge, 1995.

[46] Nikon Instruments Inc. Resolution. https://www.microscopyu.com/microscopy-basics/resolution. Accessed: 2021-06-10.

[47] JEOL Ltd. SEM Scanning Electron Microscope A To Z. Basic Knowledge For Using The SEM. https://www.jeol.co.jp/en/applications/pdf/sm/sem_atoz_all.pdf. Accessed: 2021-06-14.

[48] Hitachi Ltd. Advanced FE Applications Course. https://www.utoledo.edu/engineering/cmsc/pdfs/SEM%20Workshop%20presentation%201.pdf. Accessed: 2021-06-15.

[49] Weilie Zhou, Robert Apkarian, Zhong Lin Wang, and David Joy. Fundamentals of scanning electron microscopy (sem). In Scanning microscopy for nanotechnology, pages 1–40. Springer, 2006.

[50] David C Joy, Alton D Romig Jr, Joseph Goldstein, Joseph I Goldstein, et al. Principles of analytical electron microscopy. Springer Science & Business Media, 1986.

[51] Jon Orloff, LW Swanson, and Mark Utlaut. Fundamental limits to imaging resolution for focused ion beams. Journal of Vacuum Science & Technology B: Microelectronics and Nanometer Structures Processing, Measurement, and Phenomena, 14(6):3759–3763, 1996.

[52] Jon Orloff, Lynwood Swanson, and Mark Utlaut. High resolution focused ion beams: FIB and its applications: Fib and its applications: the physics of liquid metal ion sources and ion optics and their application to focused ion beam technology. Springer Science & Business Media, 2003.

[53] PD Nellist and SJ Pennycook. The principles and interpretation of annular dark-field z-contrast imaging. Advances in imaging and electron physics, 113:147–203, 2000.

[54] INL International Iberian Nanotechnology Laboratory. Scanning Elect. Microscope QUANTA 650FEG (00000555). https://lims.inl.int/WebForms/Equipment/EquipmentView.aspx?toolId=229. Accessed: 2021-06-26.

[55] INL International Iberian Nanotechnology Laboratory. Dual Beam FIB-SEM (00000549). https://lims.inl.int/WebForms/Equipment/EquipmentView.aspx?toolId=248. Accessed: 2021-06-26.

[56] PC Korir and FB Dejene. The effect of deposition time on the structural, morphological and luminescence properties of y 2 o 2 s: Eu 3+ thin films prepared by pulsed laser deposition. Applied Physics A, 124(5):1–9, 2018.